Polar Radiant Energy in the Far-Infrared Experiment (PREFIRE) Algorithm Theoretical Basis Documents (ATBDs)

Brian J. Drouin, Brian Kahn, Aronne Merrelli, Xianglei Huang, Erin Wagner, Nathaniel Miller, Yan Xie

January 2024

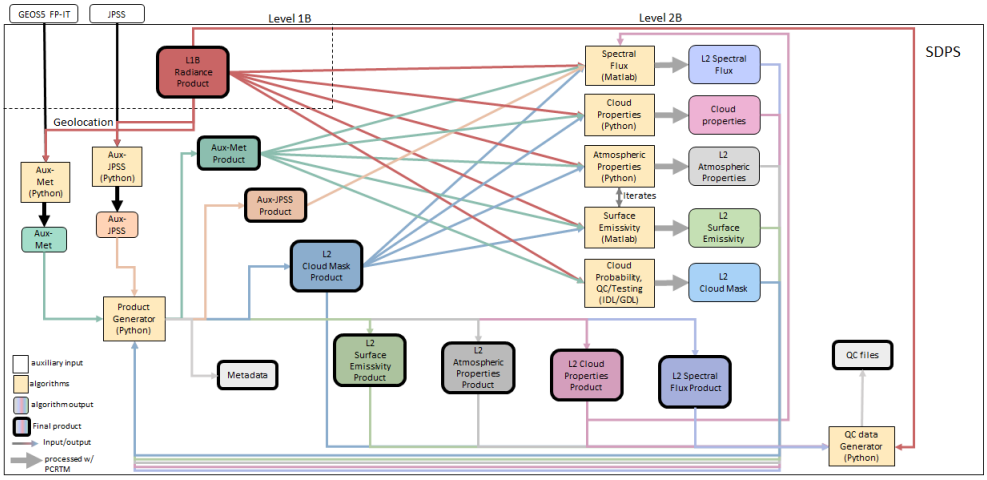

Figure 0.1: PREFIRE algorithm connectivity and flow.

Contents

1 Level 1 Radiances and Geolocation

Thermal Infrared Spectrometer Design Model Brian J. Drouin January 2024

Algorithm Theoretical Basis Document of the Thermal Infrared Spectrometer for the PREFIRE mission

1.1 Introduction

In this section we describe the radiometric, spatial and spectral characteristics of a space-based scanning Thermal InfraRed Spectrometer (TIRS) implemented for the Polar Radiant Energy in the Far-InfraRed Experiment (PREFIRE) mission. Fundamentally, TIRS is a grating spectrometer with a slit projection on the ground aligned cross-track to the satellite motion - a so-called “pushbroom” configuration. TIRS contains a 2-dimensional focal plane array detector with

one dimension aligned cross-track, parallel to the slit (spatial), and the other dimension containing the spectral information from the scene, perpendicular to the slit.

The ATBD presented here describes the theoretical basis of the instrument geometric, spectral and radiometric characteristics of TIRS, as well as details of the geolocation and radiometric calibration algorithms that are implemented as part of the PREFIRE operational L1B processing package. The TIRS geometric, spectral and radiometric characteristics are described in sections 1.2 - 1.5, followed by sections 1.6 and 1.7 that describe more specific algorithm implementation details for the L1B package.

1.2 TIRS geometric model

1.2.1 Imaging considerations

The basic angular resolution parameters are controlled by the instrument focal lengths and the detector size and spectrometer slit width. The focal lengths are different in these two perpendicular axes. In the spatial dimension, the angular width of the observed scene (α_{sc}) is limited by the detector size l_{d}; in the along-track (cross-slit) dimension, the angular width (α_{n}) is controlled by the spectrometer slit width l_{sw}. The idealized angular Instantaneous Field of View (IFOV) is then given by:

$$\alpha_{\mathrm{sc}} = l_{\mathrm{d}}/f_{\mathrm{sc}} \tag{1.1}$$

and

$$\alpha_{\mathrm{n}} = l_{\mathrm{sw}}/f_{\mathrm{n}} \tag{1.2}$$

The size of the instantaneous ground footprint for the scene, l_{sc} is then determined by the orbital altitude H:

$$l_{\mathrm{sc}} = \alpha_{\mathrm{sc}} H \tag{1.3}$$

The TIRS optical design parameters result in IFOV angles of $\alpha_{\mathrm{sc}} = 3.2°, \alpha_{\mathrm{n}} = 1.3°$. At a nominal orbital altitude of $H = 540$ km, the IFOV ground footprint size of each scene is approximately 30×12 km (along track $\times$ cross track).

The total number of cross-track scenes with cross-track dimension l_{sc} is determined by the number of detector strips (rows) in the focal plane array. Due to gaps between detector strips, the spatial sampling is not contiguous, with separations between samples in the cross-track direction equal to

$$\Delta l_{\mathrm{gap}} = l'_{\mathrm{d}} H/f_{\mathrm{sc}} \tag{1.4}$$

The total angular field of view of the swath, that projects to the ground swath width (l_{SW}), is determined by the pixel width and spacing (l'_{d}) of these rows, and the number of detector rows, $M_{\mathrm{FPA}} = 8$:

$$l_{\mathrm{SW}} = M_{\mathrm{FPA}} l_{\mathrm{sc}} + (M_{\mathrm{FPA}} - 1)\Delta l_{\mathrm{gap}} \tag{1.5}$$

The detector gaps, l'_{d} are slightly more than a factor of two larger than the detector size l_{d}. The resulting swath width, l_{SW}, is approximately 270 km.

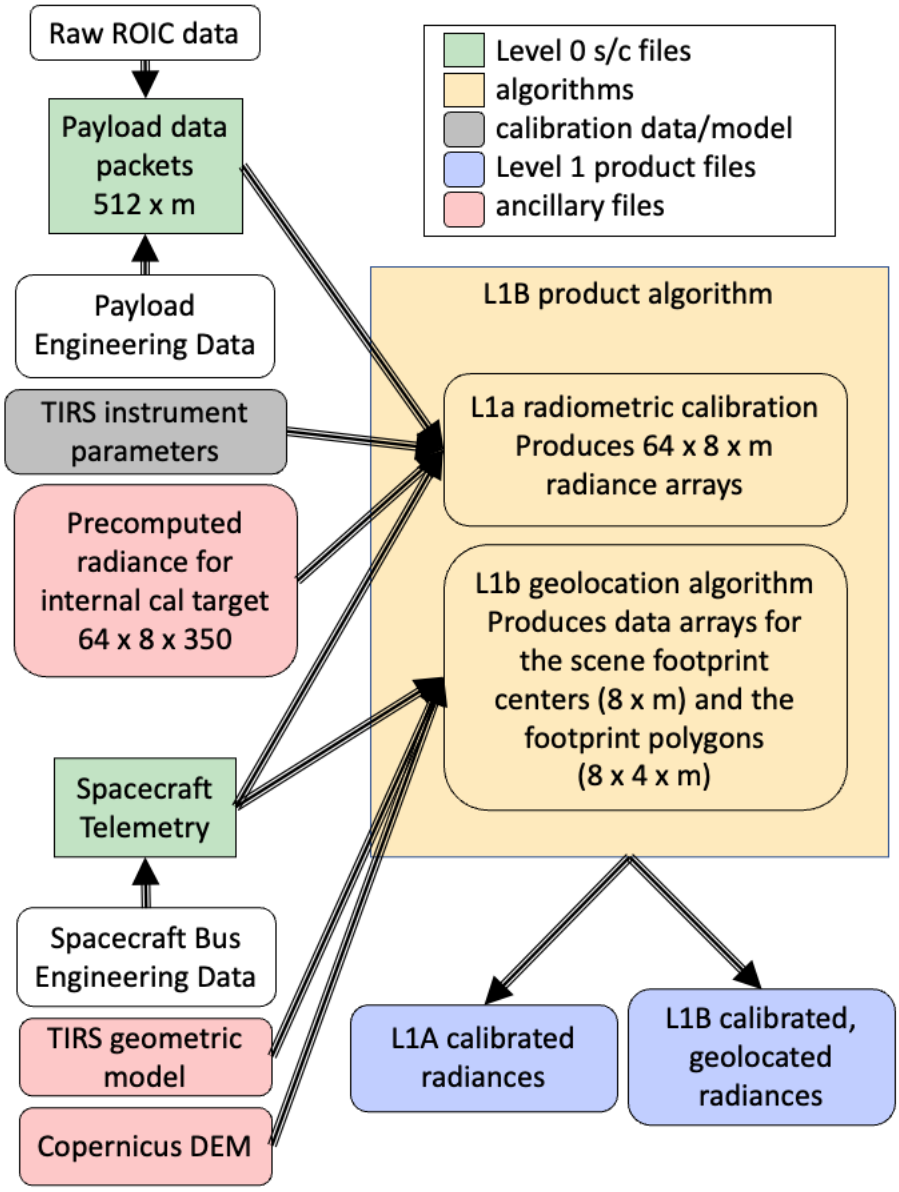

Figure 1.1: Flowchart depicting L1B algorithms and the input and output data files. The array dimensions are given, with the number of spectral channels, $n = 64$, number of spatial scenes, $sc = 8$, and the number of pre-computed cal target temperatures equal to 350.

1.3 Scene FOV model

The Level-0 spacecraft data includes the Earth Centered Inertial (ECI) position and velocity. The nominal attitude of the spacecraft with respect to latitude and longitude can be determined from transformation from the spacecraft frame to the instrument frame and these ECI positions and velocity components. The subroutine converts all positions to geodetic coordinates and determines the spacecraft azimuth angle, β from a finite difference of geodetic spacecraft latitude and longitude positions (ϕ,θ) one unit velocity vector apart. The calculation for β can be written as follows, in terms of the ECI positions, spacecraft latitude and longitude, and the orbital radius (R_e):

$$\beta = -\arctan \frac{R_e(\phi - \phi')}{\sqrt{x_{\mathrm{ECI}}^2 + y_{\mathrm{ECI}}^2}(\theta - \theta')} \tag{1.6}$$

Additional corrections to the attitude vector associated with yaw/pitch and roll of the spacecraft can be applied while determining the azimuth and tilt of the TIRS optical axis in the ECI. These will be described after providing the focal plane coordinate projections.

The angular projections of the detector dimensions onto the earth scene, l_{sc} and l_{n} are determined from instrument pointing, composed as tilt (α') and azimuth (β'), as well as the orbital height, and geometric properties of the TIRS instrument provided from pre-flight testing. Imperfections of imaging will be projected onto Level 1b radiances as part of the geo-rectification algorithms.

Ground calibration of the TIRS instruments enable modeling of instantaneous field-of-view limits for each pixel, with centers $l_{sc,m}^{\mathrm{c}} = (X_{sc,0}^{\mathrm{c}}, Y_{sc,0}^{\mathrm{c}})$ defined as the projected rays normal to the focal plane from an internal detector coordinate system. The detector coordinate system places the M_{FPA} zero - order pixels centered along the $X_{sc,0}^{\mathrm{c}} = 0.0$ axis, with $Y_{sc,0}^{\mathrm{c}}$ values evenly spaced at

$$Y_{sc,0}^{\mathrm{c}} = (sc - (M_{\mathrm{FPA}} - 1)/2)(l_p + l_{\mathrm{gap}}) \tag{1.7}$$

For ideal center ray angles of each pixel, Y-coordinates, corrected for spectral dispersion, provide the nominal tilt angle ($\alpha_{sc,n}^{c}$) which is the angle subtending nadir and the pixel footprint. The tracing of this distortion in the spectral dimension results in a shift of the spectral response function (described later) with respect to other spectral images, so only the spatial distortion is considered in this section. These distortions ($X_{sc,n}^{\mathrm{c},\pm}, Y_{sc,n}^{\mathrm{c},\pm}$) will be measured and quantified with a geometric instrument model ($\mathcal{F}$) as offsets to the geo-located zero-channels.

$$X_{sc,n}^{\mathrm{c},\pm} = X_{sc}^{\mathrm{c},\pm} + \mathcal{F}(sc, \lambda) \tag{1.8}$$

and

$$Y_{sc,n}^{\mathrm{c},\pm} = Y_{sc}^{\mathrm{c},\pm} + \mathcal{F}(sc, \lambda) \tag{1.9}$$

A line of points associated with the ground track are defined by projection from orbit using these M_{FPA} values. Spectral footprints depend on physical

pixel location and dispersion corrections in the X coordinates as shown later. Additionally, the finite size of the slit and width and breadth of the pixels each must be projected also in order to track the (potentially distorted) images onto the earth surface. Geometric calibration of the instrument provides a 2D model of the pixel centroids and corners, in which any mis-alignment of the third dimension is projected onto the (actual) focal plane and blurs the 2D projection. The corner coordinates are paired by $(X^{+}_{sc,n}, Y^{+}_{sc,n})$,$(X^{+}_{sc,n}, Y^{-}_{sc,n})$,$(X^{-}_{sc,n}, Y^{+}_{sc,n})$, and $(X^{-}_{sc,n}, Y^{-}_{sc,n})$.

Adjustments to the azimuth and tilt (indicated with primes) are necessary to track the corners (and any non-ideal centroid positions), and these adjustments for α become,

$$\alpha'^{\mathrm{c},\pm}_{sc,n} = \frac{\alpha^{\mathrm{c},\pm}_{sc,n}}{|\alpha^{\mathrm{c},\pm}_{sc,n}|}\sqrt{(\alpha^{\mathrm{c},\pm}_{sc,n})^2 + (dX^{\mathrm{c},\pm}_{sc,n})^2} \tag{1.10}$$

where dX is the angular difference between the pixel corner x coordinate and the ideal position of the pixel centroid.

$$dX^{\mathrm{c},\pm}_{sc,n} = (X^{\mathrm{c},\pm}_{sc,n} - X^{\mathrm{c},0}_{sc,n})/f \tag{1.11}$$

A similar correction for β' is found

$$\beta'^{\mathrm{c},\pm}_{sc,n} = \tan^{-1}(dX^{\mathrm{c},\pm}_{sc,n}/\alpha^{\mathrm{c},\pm}_{sc,n}m) \tag{1.12}$$

These equations for azimuth and tilt can be easily modified to accommodate for yaw, pitch and roll with respect to the spacecraft velocity vector in which β is defined (the nadir vector has been assumed for tilt). For yaw correction, the value is added directly to β, and for roll the value is added to α. The pitch of the spacecraft distorts the projection in the same sense as the angular coordinate dX and can thus be added to the differential angular coordinate prior to its use in calculating α' and β'.

None of the spatial scenes directly project perpendicularly from the instrument/spacecraft, the rays diverge across the swath with an observing gap in the center due to the even number of pixels. Thus the rays spread out in the cross-track direction from the instrument/spacecraft pointing direction, where the scene-specific angular dependence can be computed from the angular IFOV.

1.4 TIRS Spectral Sampling and Resolution

The spectral sampling interval depends on the desired spectral range and number of detectors per column in the focal plane. The total number of detectors allowed in the spectral direction is n (equal to 64), including the non-spectral detection channel known as the 'zero' channel.

The ideal spectral sampling interval is then the range BW, divided by the number of elements

$$\Delta\lambda_{\mathrm{s}} = \frac{\lambda_2 - \lambda_1}{n-1} \tag{1.13}$$

where $\Delta\lambda_s$ = Spectral sampling interval (μm)
λ_2 = Maximum wavelength desired (μm)
λ_1 = Minimum wavelength desired (μm)
The spectral dispersion is a property of the grating related to the groove spacing l_g.

The angular response of a grating as a function of wavelength is governed by the grating equation

$$l_g(\sin\zeta_i - \sin\zeta_m) = m\lambda \tag{1.14}$$

Where ζ_i is the incidence angle, m is the diffraction order and ζ_m is the angle at which the wavelength λ exits the grating for its m^{th} order. Such that

$$\zeta_m = \left(\frac{m\lambda}{l_g} - \sin\zeta_i\right) \tag{1.15}$$

Since m can be any integer, positive, negative and zero, the grating distributes light in multiple directions with overlapping effect. In an Offner spectrometer, the toroidal curvature of the grating (with X-periodicity) and compensating toroidal optic project the outgoing central dispersive rays within the f-cone at a normal incidence angle at the detector. Thus, the spectral dimension, x, of the focal plane can be described without angular factors. The intersections of the n^{th} wavelength with the focal plane may be described linearly with an effective dispersion ($l_g = l(n-1)/\mathrm{BW}$). For spectrometry, the $M \times n$ thermopile detector array in TIRS is situated behind an Offner spectrometer with a slit width that is chosen to be 2 pixel widths (d) in the spectral dimension. Thus the angular response of the system in the spectral direction is linearized onto the x coordinate for convolution of the slit, the diffraction pattern, and the extent of the detector. The intersections of the n^{th} wavelength with the focal plane may be described

$$x_n = m\frac{\lambda_n}{l_g} + x_0 + x' \tag{1.16}$$

Where x_0 is the intersection of the 0^{th} order (non-diffracted or reflected) ray in the chosen focal plane coordinate system and x' is the (nominally zero) offset of the slit center from the optical axis.

$$\Re_{n,\lambda} = \Re_{\mathrm{slit}}(x' \pm l_{\mathrm{sw}}/2) \otimes \Re_{\mathrm{det}}(x_0 + l[n \pm 1/2]) \otimes \Re_{\mathrm{diff}}(x, \lambda) \tag{1.17}$$

$\Re_{n,\lambda}$ = Linearized response of the system in the spectral direction for channel n
$\Re_{\mathrm{slit}}$ = Rectangular response function representing the slit
$\Re_{\mathrm{det}}$ = Rectangular response function representing the detector
$\Re_{\mathrm{diff}}(\lambda, x)$ = Line spread function response of the optics including diffraction
λ = Wavelength (μm)
l_{sw} = slit width (μm)
In many optical models, $\Re_{\mathrm{diff}}$ is assumed to have a small wavelength dependence and the spectral response function is fitted to a Gaussian, with another

Gaussian representing the spatial spreading. However, the large bandwidth of TIRS makes such an assumption circumspect, so the wavelength dependence of the instrument function is explicitly calculated at several sub-pixel (wavelength) steps, and then convoluted with both the detector and slit sizes. The diffraction pattern is assumed to be a ideal scaled sinc function:

$$\Re_{\text{diff}}(x) = \left(\frac{\gamma \sin(\pi x/\gamma)}{\pi x}\right)^2 \tag{1.18}$$

The spectral resolution of the system is the FWHM of the spectral response function

$$\Delta\lambda_n = \text{FWHM}(\Re_{n,\lambda}) \tag{1.19}$$

where $\Delta\lambda_n$ = Spectral resolution of the n^{th} detector element (μm).

Although diffraction spreads out the longer wavelengths at the focal plane, often into adjoining pixels, this is considered a blurring of the scenes and not a loss of signal. The convolution with the slit and detector widths properly accounts for this effect as long as the adjacent scenes are spectrally similar. Issues with geometric calibrations will be encountered in non-flat field images.

A similar blurring, or vignetting, effect occurs in the spatial or y dimension of the sensor with:

$$\Re_{sc,\lambda} = \Re_{\text{slit}}(y' \pm l_{\text{sl}}/2) \otimes \Re_{\text{det}}(y_0 + l_{\text{p}}[sc \pm 1/2]) \otimes \Re_{\text{diff}}(y, \lambda) \tag{1.20}$$

Where $\Re_{m,\lambda}$ = diffraction limited response of the system in the spatial direction
$\Re_{\text{diff}}(y, \lambda)$ = Line spread function response of the optics including diffraction
l_{sl} = slit length (μm)
sc = spatial scene counter from $1 \cdots 8$

1.5 TIRS Radiometric model

1.5.1 Signal Calculation

The thermopile detectors used by TIRS are sensitive to the total net radiation at the detector surface, from all wavelengths and incidence angles. The net radiation is a balance of thermal radiation emitted by the detector, emitted by the instrument optical elements along the optical path, emitted by the instrument internal structure, and the incident radiation from the observed scene, all expressed as at-detector irradiances (radiation incident on the detector) or exitance (radiation emitted by the detector) in units of W m^{-2}. The TIRS scan mirror can select between an Earth view, space view, or internal calibration target for the observed scene. The total net radiation can be described by a simplified model of the instrument that splits the total irradiance for at the detector for channel n ($E_{\text{total},n}$) into multiple terms:

$$E_{\text{total},n} = E_{sc,n} + E_{\text{filt}} + E_{\text{inst}} - \sigma_B T_{\text{det}}^4 \tag{1.21}$$

where $E_{sc,n}$ is the irradiance from the observed scene for spectral channel n; E_{filt} is irradiance emitted from the order-sorting spectral filter; E_{inst} is irradiance emitted from other optical or instrument surfaces that passes through the order sorting filter; and the final term is the exitance emitted from the detector itself. Note that the detector is assumed to be a blackbody (unit emissivity) such that the total exitance is given by the Stefan-Boltzmann law. The remaining terms all have spectral dependent terms (e.g. the order sorting filters' spectral transmission and emissivity).

The spectral irradiance from the scene is the spectral integral of the product of the spectral response function and the scene spectral radiance $L(\lambda)$ and the angular integral over the incident light cone at the detector with $\cos\theta$ weighting. The spectral response function can be written as the product of the line spread function described above ($\Re_{n,\lambda_i}$), the order sorting filter transmission ($\tau_{\text{f},\lambda_i}$) and the grating efficiency ($^1\rho_{g,\lambda_i}$):

$$\text{SRF}_n(\lambda_i) = {}^1\rho_{\text{g},\lambda_i}\ \tau_{\text{f},\lambda_i}\ \Re_{n,\lambda_i} \tag{1.22}$$

$$E_{sc,n} = \int_{\lambda_0}^{\lambda_1}\int_{\Omega} \text{SRF}_n(\lambda) L(\lambda)\cos\theta\ d\lambda\ \sin\theta\ d\theta\ d\phi \tag{1.23}$$

Note that the light cone (Ω) is the TIRS optical path is not circular, due to the different focal lengths in the along-slit and cross-slit dimensions. The elliptical shape means the integration limits do not have simple analytic expressions. In practice, the average between the two cone angles can be used with relatively small error (less than 10%), since the focal lengths are not too different.

The non-dispersive light from the scene is detected in a broad-band channel and corresponds to signal $E_{\text{sc},0}$, which has no order sorting filter in the optical path. In this case, the total irradiance can be written as:

$$E_{\text{total},0} = E_{sc,0} + E_{\text{inst},0} - \sigma_B T_{det}^4 \tag{1.24}$$

Where the irradiance due to the scene ($E_{\text{inst},0}$) is different than the similar term in equation 1.21, due to the lack of order sorting-filter contributing to thermal emission and reflection in the path. The scene irradiance depends on the reflective efficiency of the grating ${}^0\rho_{g,\lambda}$ and the transmission of the diamond focusing window, τ_C:

$$E_{sc,0} = \int_{\lambda_0}^{\lambda_1}\int_{\Omega} {}^0\rho_{\text{g},\lambda}\ \tau_C\ L(\lambda)\cos\theta\ d\lambda\ \sin\theta\ d\theta\ d\phi \tag{1.25}$$

Although the instrument is designed to maximize the thermal signal from the objective, thermopile detectors are sensitive to all wavelengths incident upon the devices from the entire hemisphere above, such that $E_{sc,n}$ is only a fraction of the temperature change sensed by the detector element. In a perfect thermopile design, the walls, or internal instrument 'scene', are *exactly* the same temperature as the detector, such that the device is only sensitive to the scene at the objective. Due to the heat dissipated from the detection electronics, the

TIRS detectors, with temperature T_{det}, are relatively warm in comparison to other instrument elements, such as the filters and optics, with temperatures T_{filt} and T_{optics} that are typically one degree and four degrees C cooler, respectively. The L1 on-orbit radiometric calibration algorithm is designed to account for these temperature gradients as part of the time varying offset term (see section 1.7).

The signal levels above are expressed in terms of irradiances, as that is the fundamental radiative quantity at the detector level. The radiation of the observed scene is more naturally expressed in terms of the spectral radiance with units W m^{-2} sr^{-1} μm^{-1}. We can compute the expected scene spectral radiance for channel n ($L_{sc,n}$) by applying the SRF in the standard way:

$$L_{sc,n} = \frac{\int_{\lambda_1}^{\lambda_2} L_{sc}(\lambda)\ \text{SRF}_n(\lambda)\ d\lambda}{\int_{\lambda_1}^{\lambda_2} \text{SRF}_n(\lambda)\ d\lambda} \tag{1.26}$$

Our definition of SRF 1.22 does not include a normalization, which means the amplitude of the SRF includes information about the total system throughput. The SRF amplitude, defined this way, could include potential systematic biases or uncertainties (for example, we do not include the reflectivity of the mirror). However, since our fundamental radiance product is a spectral radiance, through the standard application of the SRF (1.26) the overall amplitude is automatically normalized and only the SRF spectral shape impacts the result.

Finally, each thermopile detector has a characteristic voltage related to the net at-detector irradiance described above, such that the detector responsivity, $\wp_{sc,n}$ (with units V/W) and detector area, l_p^2 (converted to m^2), allow calculation of the sensible voltage, V:

$$V_{sc,n} = l_p^2 \wp_{sc,n} E_{\text{total},n} \tag{1.27}$$

1.5.2 Instrument Noise

The detector noise of the thermopile detectors is generally spectrally flat. All detector elements will have approximately the same Noise Equivalent Power (NEP), typically expressed by a constant detectivity D^*. Additional terms, such as electronics noise from the read out integrated circuit (ROIC), could be converted from voltage to power using the instrument responsivity, and added in quadrature to get the total instrument noise.

Ultimately we need the instrument noise defined as a NEDR (Noise equivalent delta spectral radiance) to match the fundamental radiometric quantity reported in the L1b data product. In principle, the NEDR can be computed based on the detector D^* and electronics noise, and combining with other relative instrument parameters such as the optics f-number and detector areas. In practice, the instrument NEDR is best estimated empirically by analysis of collected sensor data. In this manner, any unknowns in the original instrument parameters or changes in instrument characteristics during hardware integration would automatically be included in the NEDR estimate. This is particularly

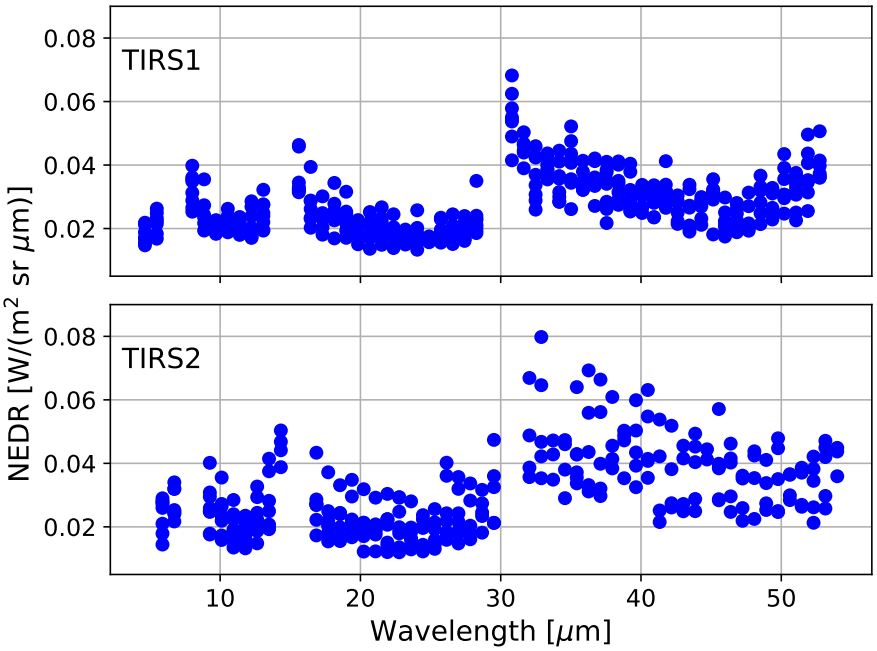

Figure 1.2: The spectral NEDR of TIRS1 and TIRS2 estimated from pre-launch radiometric calibration data. Noisy or unresponsive pixels are omitted from the plot. The gaps at wavelengths $\sim$ 8, 15, and 31 μm are due to the edges of the order sorting filters.

important for identifying bad detector elements that may change behavior over time.

Figure 1.2 shows the empirically estimated channel NEDRs from the pre-launch radiometric testing of each TIRS instrument. Noisy or unresponsive detector elements have been omitted from the plot. The on-orbit detector performance often changes post launch, so these pre-launch estimates will be replaced with on-orbit estimates if necessary.

1.5.3 Digitization

The TIRS ROICs have integrated analog-to-digital converters, and thus the associated gain, g^{IC}, has units of counts/volt. An offset, o^{IC}, in the digitizer allows for all counts to be positive values. The gain and offset are specific to each ROIC, and thus equal for a series of TIRS channels, here we assume that all ROICs have equal gain and offset values. The signal digitization enables the TIRS data memory storage to contain arrays of integers, $\mathbb{S}$, that are $sc \times n$.

$$\mathbb{S}_{sc,n} = o^{IC} + g^{IC} V_{sc,n} \tag{1.28}$$

Raw TIRS data contain blocks of the $\mathbb{S}_{sc,n}$ arrays separated by headers to indicate housekeeping information and the target selecting mirror positions.

The factors τ_f,${}^n\rho_g$,$\Re_{sc,n}$ are determined by calibration or approximated by the system design parameters. It is common for SRF to be normalized to unity and efficiency factors to be absorbed into $\Re$ coefficients. The choice here to have a relatively flat value of $\Re$ for each pixel is from an engineering perspective and retains the broadband nature of these elements. For purposes of signal and noise differentiation, the signal equations will be separated by the scenes, such that the effects of instrument and detector temperature variation will be treated as noise and assumed constant for signal.

1.5.4 Out of Band signal

In addition to capturing the pure reflection (0^{th} order) and primary (1^{st} order) of the grating, other (higher) grating orders will propagate into the detector plane and produce signals if not absorbed or scattered by the filters. The wavelengths, at a given channel, of this undesired radiation are related through the linearized grating equation 1.16. Orders other than the 1^{st} order fall outside of the designed filter bandwidths, such that the minimal filter transmission at these positions attenuates the light.

The out-of-band term can be added by generalizing the SRF to m orders.

$$\mathrm{SRF}_{sc,n}(\lambda_i) = \sum_{m=1}^{3} \rho_{g,\lambda_i/m}\tau_{\mathrm{f},\lambda_i}\Re_{n,\lambda_i/m} \tag{1.29}$$

1.6 Level 1 Geolocation Algorithm

The geolocation algorithm starts with the sets of tilt and azimuth angles at the scene centers and corner points, described in section 1.2, that define the TIRS IFOV. As described above, the in-track IFOV, perpendicular to the spectral slit, is approximately 30 km. Dwell time, t, is the amount of time the image is averaged (or integrated) while the along-track IFOV moves across the surface during the orbital motion. At the nominal PREFIRE orbital altitude, the magnitude of the satellite ground velocity, $|v_{\mathrm{g}}|$ is approximately 7.6 km/s. The TIRS dwell time is 0.7s, corresponding to an additional extent of the (non-instantaneous) FOV by approximately 5 km along-track, yielding a total FOV size of 35×12 km (along track $\times$ cross track). Since the along-track IFOV is much larger than the orbital motion during the dwell time, successive observations will contain substantial overlap in their ground footprints.

To find the geodetic ground latitude, $\phi_{sc}^{\mathrm{c},\pm}$, and ground longitude, $\theta_{sc}^{\mathrm{c},\pm}$, of each point projected onto the oblate spheroid earth, we utilize a MATLAB routine `lookatSpheroid` which was confirmed with custom code to efficiently compute the distance to and positions on the oblate Earth. For the scene centers, this projection is done at the halfway point ($\frac{1}{2}t$) of the integration time. Additional projections are done at each corner of the scene (according to the $(X_{sc,n}^{\pm}, Y_{sc,n}^{\pm})$ described above), both at the beginning and end times of

the detector integration time (to capture the full extent of the motion-smeared FOV) and at the central time (to capture the IFOV at the mid-point of the integration). These projections to geodetic ground position assume the WGS84 ellipsoidal model.

Starting from the geodetic, ellipsoidal latitude and longitude, the earth geoid (EGM96 model) and topography are sampled in order to obtain the surface elevation at all ground points. The surface elevation is used with an iterative algorithm to update the altitude and latitude and longitude positions by accounting for the line of sight vector's intersection with the elevated surface. This algorithm is implemented in a similar fashion as the VIIRS geolocation algorithm (VIIRS geolocation ATBD, 2017). The surface topography is derived from the Copernicus 90m Digital Elevation Model (GLO-90 DEM).

1.7 Level 1 Radiometric Calibration Algorithm

During nominal operations, the instrument performs active calibration sequences in which it is commanded to observe an internal calibration target at T_{cal} and external view of cold space at temperature T_{sp}. These calibration views are used in a two-point (linear) calibration equation to convert the raw counts ($\mathbb{S}_{sc,n}$) into calibrated spectral radiance ($L_{sc,n}$).

At TIRS wavelengths, the cold space at $T_{\text{sp}} \sim 2.7$ K produces essentially zero radiance, so the E_{sc} term in 1.21 would also be zero. Therefore, the space view quantifies the aggregate contributions of the background signals (E_{filt}, E_{inst}, and $\sigma_B T_{\text{det}}^4$ in 1.21), while the calibration target view includes the same terms as well as a scene radiance equal to blackbody emission at T_{cal}. The TIRS optical path and internal calibration are designed to be as isothermal as possible, which reduces calibration bias due to uncertainty in the blackbody target emissivity. Therefore, the radiance from the internal calibration target is assumed to be a blackbody ($\varepsilon = 1$).

Combining equations 1.21 and 1.28 and taking the difference between counts measured from a calibration target view ($\mathbb{S}_{sc,n}^{\text{cal}}$) and a space view ($\mathbb{S}_{sc,n}^{\text{sp}}$), yields:

$$\mathbb{S}_{sc,n}^{\text{cal}} - \mathbb{S}_{sc,n}^{\text{sp}} = g^{IC} l_p^2 \wp_{sc,n} E_{sc,n} \tag{1.30}$$

Since the at-detector scene irradiance $E_{sc,n}$ is proportional to the at-aperture scene spectral radiance $L_{sc,n}$ we can rewrite this equation in terms of L, and lump all constants together into a single radiometric gain $g_{sc,n}^{\text{rad}}$:

$$\mathbb{S}_{sc,n}^{\text{cal}} - \mathbb{S}_{sc,n}^{\text{sp}} = g_{sc,n}^{\text{rad}} L_{sc,n} \tag{1.31}$$

For the view of the calibration target, the $L_{sc,n}$ are assumed to be blackbody radiances after applying the SRFs using equation 1.26. For efficiency, these values are pre-computed in a lookup table over a range of T_{cal}, and then linearly interpolated to the T_{cal} sampled at the time of the calibration target view. Given the interpolated pre-computed blackbody radiances $B_{sc,n,T_{\text{cal}}}$, the radiometric

gain is computed as:

$$g_{sc,n}^{\text{rad}} = \frac{\mathbb{S}_{sc,n}^{\text{cal}} - \mathbb{S}_{sc,n}^{\text{sp}}}{B_{sc,n,T_{\text{cal}}}} \tag{1.32}$$

Application of the gain to the measured earth signal allows calculation of the calibrated earth spectral radiances, $L_{sc,n}$, designated the Level 1a (L1a) science data. This calculation uses the space view counts as the offset term ($\mathbb{S}_{sc,n}^{sp}$) and divides by the radiometric gain:

$$L_{sc,n} = \frac{\mathbb{S}_{sc,n} - \mathbb{S}_{sc,n}^{\text{sp}}}{g_{sc,n}^{\text{rad}}} \tag{1.33}$$

Because the background terms will drift as the instrument temperatures change, the gain and offset terms must be interpolated from the values derived at the calibration sequence times to the times for each TIRS earth view observation. The interpolation method must replicate the temporal behavior of the background terms. More frequent calibration sequences will allow for simpler calibration functions, at the cost of lost earth-view science data collections. The current implementation of the radiometric calibration uses the "makima" (Modified Akima piecewise cubic Hermite interpolation) in MATLAB for the temporal interpolation. During IOC the performance of this method will be evaluated, with the goal of maximizing the earth-view science data that can be collected with minimal radiometric calibration error.

1.8 References

Joint Polar Satellite System (JPSS) VIIRS Geolocation Algorithm Theoretical Basis Document, Rev A, 2017. Available from `https://www.star.nesdis.noaa.gov/jpss/Docs.php`

Copernicus Digital Elevation Model (DEM), GLO-90, was accessed on 30 October 2022 from `https://registry.opendata.aws/copernicus-dem`.

2 Level 2 Cloud Mask

2.1 Introduction

The PREFIRE L2 algorithm suite requires that every TIRS scene is known to be either clear or cloudy. This determination is made through a cloud masking algorithm designed for TIRS. Not only should this algorithm work globally, but it should perform seamlessly in the high latitudes where geophysical conditions make cloud detection especially challenging. Towards this end, the PREFIRE algorithm team developed two independent cloud masks based on different algorithm heritage and training set approaches. The first approach leverages a principal component (PC) methodology (PC-MSK) developed for ESA's FORUM mission and is described in Kahn et al. (2023). The second approach is based on a neural network (NN) methodology (NN-MSK) and is described in Bertossa et al. (2023). Having two alternative – and potentially complementary cloud mask algorithms – will enhance the chances of successfully meeting or exceeding the PREFIRE mission requirements (see Section 2.2).

2.2 PREFIRE mission requirements

The PREFIRE mission has clearly defined requirements for the L2-MSK product. (1) The cloud mask is required to detect 80-90% of clear-sky occurrences. The primary usage of the cloud mask is to identify clear scenes with high confidence such that other downstream PREFIRE algorithms can operate within clear-sky conditions to meet their own requirements. (2) The aforementioned requirement applies to clear-sky scenes with spatial scales of 15-50 km and larger extents. At these scales, clear-sky is mostly resolved by the nominal TIRS spatial footprint size. Clear-sky scenes with scales smaller than 15 km are smaller than the TIRS spatial footprint size and have no mission requirement for detection.

2.3 PC Mask

2.3.1 Use of GMAO simulations

Algorithm development was carried out with a simulated L2-MSK that leveraged GMAO numerical model output with radiances generated from PCRTM. The simulations are intended to mimic the expected TIRS instrument characteristics and post-launch noise estimates. The L2-MSK will be tailored to the unique characteristics of the two TIRS instruments during the post-launch time period.

The initial version of L2-MSK is based on GMAO simulations coupled to a Level-1 TIRS instrument model (see Section 1). The TIRS radiances simulated with the GMAO model are used with initial TIRS SRF estimates using PCRTM. The simulations are available over the entire globe for a range of days during 2020 with a nominal configuration mimicking expected PREFIRE cubesat orbits. Some relevant GMAO fields of interest include profiles of temperature (T), specific humidity (q), cloud optical depth (COD), and ice/liquid water content

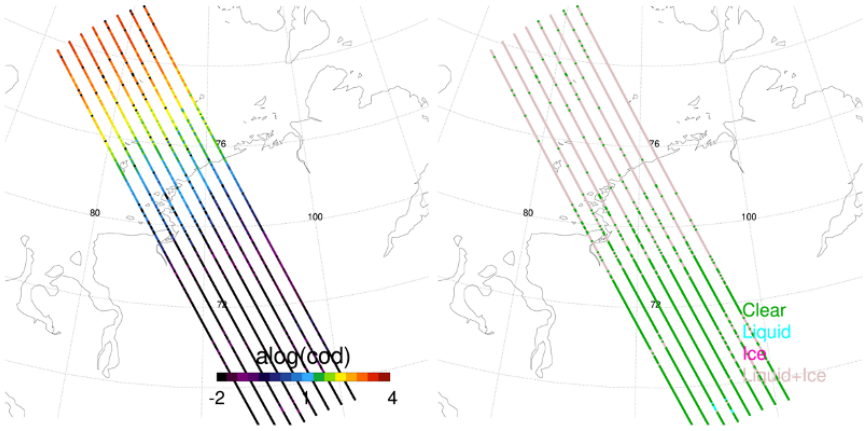

Figure 2.1: GMAO simulations of column optical depth in natural log scale (left) and cloud top thermodynamic phase (right). Shown is an orbital segment of TIRS data along the Siberian coastline for eight cross-track and 250 along-track TIRS scenes.

(IWC/LWC). Log-scale values of COD are shown in Figure 2.1 for an example orbital segment along the Siberian coastline. The cloud-top thermodynamic phase (liquid, ice, mixed) from the simulations is also depicted. This particular scene is fairly typical in that clear-sky is located over land and clouds are found over the ocean. Further examples over Greenland and in the low-latitudes are described in Kahn et al. (2023).

Lower tropospheric stability (LTS) is defined as the difference in potential temperature between 700 hPa (θ_{700}) and 1000 hPa (θ_{1000}). LTS is a useful metric for capturing vertical layers that may contain quasi-isothermal lapse rates or temperature inversions that could be problematic for thermal-based cloud detection (e.g., Garay et al. 2008). The GMAO profiles of water vapor mixing ratio are integrated into a single value of integrated precipitable water vapor (PWV). LTS and PWV are shown in Figure 2.2. This scene exhibits strong variability in thermal structure and moisture and complements the cloud complexity depicted in Figure 2.2. High values of LTS are common within the Arctic region and complicate cloud detection. Furthermore, variable amounts of PWV can also complicate cloud detection as water vapor absorption features strongly depend on the TIRS channel frequency.

2.3.2 Adapting the FORUM cloud detection method to TIRS

We briefly summarize the implementation of the Maestri et al. (2019) methodology developed for the FORUM mission to the TIRS instruments. The training sets of clear-sky and cloudy-sky radiances are drawn from 20 randomly selected spectra from GMAO simulations in orbital segments of eight cross-track and 250 along-track TIRS scenes, where each orbital segment has a new random draw.

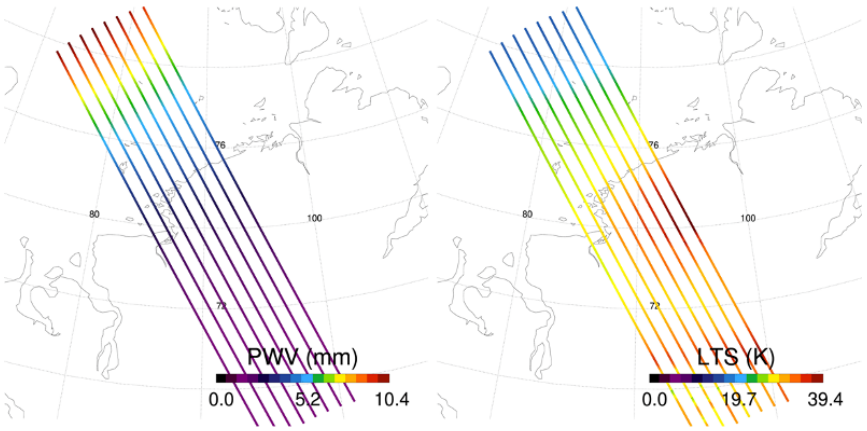

Figure 2.2: GMAO simulations of precipitable water vapor (PWV) (left) and lower tropospheric stability (LTS) (right).

The clear-sky radiances are simulated for every TIRS scene - regardless of the presence of clouds - and will be calculated as part of the post-launch operational algorithm. A set of 20 random draws from the TIRS scenes for clear and cloudy skies are shown in Figure 2.3 for the same orbital segment shown in Figures 2.1 and 2.2. While the radiances for cloudy scenes are slightly lower than clear-sky radiances, there is substantial overlap in their magnitudes making it challenging to visually distinguish differences between clear and cloudy sky. However, there are more subtle differences in the spectra that the PC approach is designed to exploit (see below). This scene is typical of the Arctic region; much cleaner separation in clear and cloudy sky spectra is observed in the midlatitudes and tropics (Kahn et al. 2023).

The Similarity index (SI) developed by Maestri et al. (2019) defines the closeness of a given radiance spectrum to two different training data sets for clear and cloudy skies; here we apply this method to the GMAO simulations. The SI uses empirical orthogonal functions (EOFs) and principal components (PCs) separately derived from the clear and cloudy sky training data sets. The value of SI is normalized and ranges from -1.0 to +1.0. See below discussions for details on the calculation of SI. We employ similar terminology used in Maestri et al. (2019) to describe the method to calculate SI. The SI is defined separately for clear and cloudy skies:

$$SI_{clr}(j), j \in \{1...J\}, \tag{2.1}$$

and

$$SI_{cld}(j), j \in \{1...J\}, \tag{2.2}$$

where J is the number of TIRS footprints considered (i.e., the total number in a segment of an orbital granule, nominally J=2000). The two sets of training

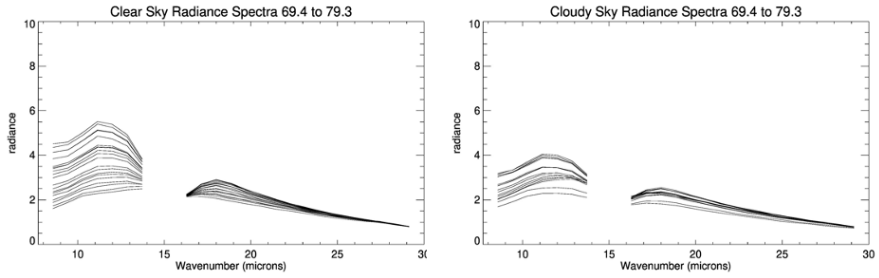

Figure 2.3: Twenty clear-sky (left) and twenty cloudy-sky (right) training radiances from the GMAO simulations for the orbital segment depicted in Figures 1 and 2. The training methodology for this simulated data set, and the plan for the post-launch TIRS radiances, are described in Kahn et al. (2023). The PC-MSK only uses the 23 channels available in filters 2 and 3, following the same approach used in L2-SSE. Note the substantial overlap in the spectral shapes and radiance magnitudes between clear and cloudy sky. This highlights the degree of difficulty in the high latitude regions.

radiances $\mathbf{TR}_{clr}(\nu,\mathrm{t})$ and $\mathbf{TR}_{cld}(\nu,\mathrm{t})$ are a function of the wave number ν associated with the 23 TIRS channels used in the PC decomposition, and the index, i denoting the number of training spectra used. We then define the training eigenvector matrices:

$$\mathbf{TREM}_{clr}(\nu, PC) = eig(cov(\mathbf{TR}_{clr}(\nu, i))) \tag{2.3}$$

and

$$\mathbf{TREM}_{cld}(\nu, PC) = eig(cov(\mathbf{TR}_{cld}(\nu, i))) \tag{2.4}$$

There are two sets of EOFs, one for clear-sky and the other for cloudy-sky. The general idea is that the higher order EOFs will exhibit larger spectral differences between the two matrices than the lower order EOFs. However, some of the high order EOFs will no longer reflect geophysical variability and instead will reflect noise. A maximum number of EOFs are therefore considered for the purpose of cloud detection. This number will fluctuate between orbital segments and is discussed in Kahn et al. (2023). A total of 20 PCs are retained through empirical experimentation. The first six EOFs associated with PC 0 to 5, with additional PC values, are shown in Figure 2.4.

The first few PCs explain the vast majority of the variance. Even though the higher order PCs explain a very small portion of the variance, they are not weighted in the Maestri et al. (2019) methodology. The PCs with very little explained variance have equal weight in the methodology such that more subtle spectral differences are used to discriminate clear and cloudy TIRS footprints.

The SI is depicted in Figure 2.5 and the histogram is observed to have two distinct peaks. By definition, the peak on the left is associated with clear sky while the peak on the right is associated with cloudy sky. Initial algorithm testing by the developers showed that an automated method would be required for

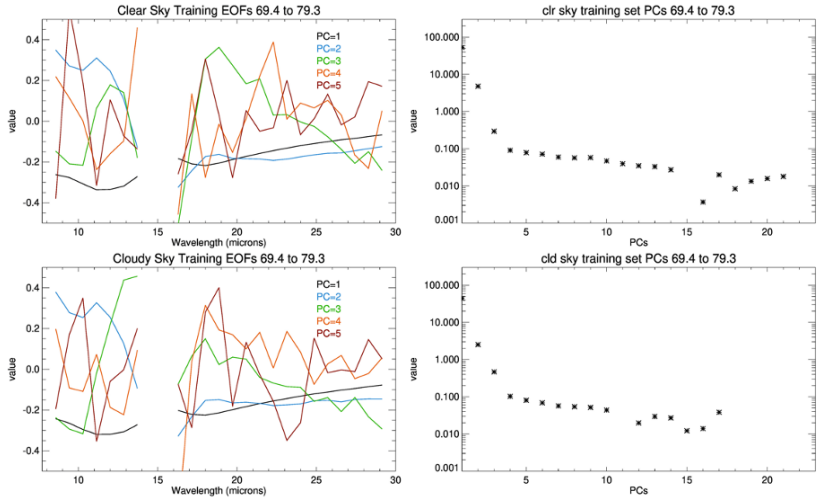

Figure 2.4: Left column: the first five EOFs for clear (top) and cloudy (bottom) sky radiance training sets. The first few EOFs are very similar between clear and cloudy sky, but larger differences appear for successive EOFs. Right column: the PC values for all EOFs. The PC-MSK uses a local training approach and thus the EOFs and PCs will change with successive orbital segments (Kahn et al. 2023).

choosing a threshold to separate clear from cloudy scenes. As described in Kahn et al. (2023), Otsu's binary classification approach was selected, as it is numerically stable, computationally efficient, and consistently ranks as one of the best algorithms for binary classification of one-dimensional histograms. The two approaches described in Maestri et al. (2019) (elementary and distributional) were deemed not appropriate for an operational algorithm and would require constant re-tuning of clear/cloudy thresholds. As the TIRS footprint is much larger than MODIS or VIIRS 1-km imagery, a simple clear/cloudy granulation in the categorization is justified as the skill in detecting clear versus cloud in difficult scenes is undoubtedly a challenge (e.g., partial cloud cover, thin clouds, topographical variability, isothermal layers, inversions). An unknown category straddling the boundary between clear and cloud was considered in the algorithm development stage but was not included as this categorization was difficult to justify, quantify, and validate.

Maps of PC-MSK, NN-MSK (to be discussed below), SI, and COD-MSK are shown in Figure 2.6. COD-MSK is a binary cloud mask considered as truth using a threshold of COD=0.25 to distinguish clear from cloud. The choice of 0.25 follows the same choice made for the NN-MSK development. The performance of PC-MSK and NN-MSK using hit and miss rates are shown as percentages in the figure panels. A fuller set of statistics is described in Kahn et al. (2023). The map of SI helps to visualize the spatial structure of the SI histogram in Figure

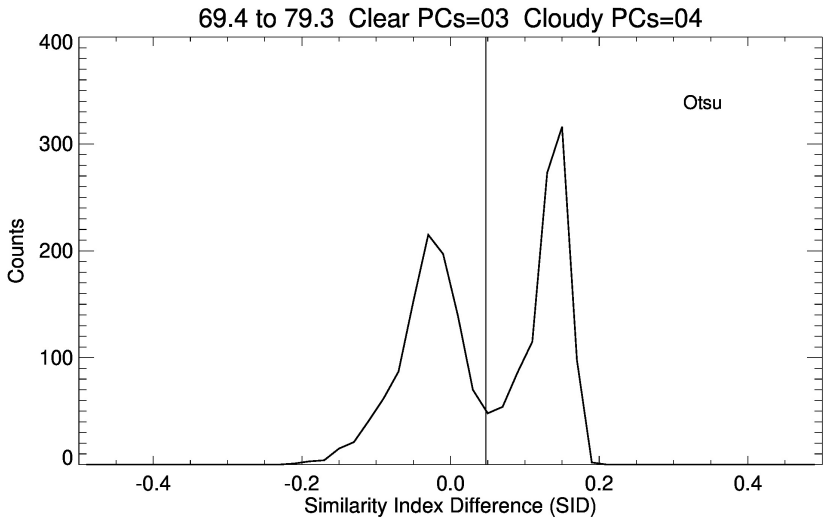

Figure 2.5: Similarity index (SI) for the same scene depicted in earlier figures. Otsu's binary classification that separates clear from cloud is shown by the vertical line. This is a fully automated classification and will vary between orbital segments. See Kahn et al. (2023) for further discussion.

2.5 and how Otsu's thresholding is capable of separating clear from cloud.

2.4 NN Mask

Here we describe the design and training procedure of the neural network (NN)-based cloud mask. A similar approach as that taken in Bertossa et al. (2023) is used. Training and evaluation are based upon simulated orbit files from GMAO simulations. A threshold of 0.25 vertically integrated cloud optical depth (COD) demarcates clear and cloudy scenes, where a value greater than or equal to 0.25 is defined as 'cloudy' and a value less than 0.25 is defined as 'clear'. This value is chosen based on maximizing the NN's ability to exploit the sensitivity of the TIRS measurements, while also preferentially detecting optically thin clouds (Fig. 2.7. In addition to the valid TIRS channels, the model uses an estimate of the 2-m temperature and total column water vapor based on the AUX-MET product. During training, noise is added to both the simulated spectra and the AUX-MET products. To simulate error in the TIRS spectra, for each channel, noise is drawn from a Gaussian distribution centered on zero with a standard deviation equal to that channel's expected error. To simulate model error in predicting 2-m temperature, noise is sampled from a Gaussian distribution with mean 0 and standard deviation of 1 K. To simulate model error in predicting total column water vapor, a relative error is used where noise is sampled from a Gaussian distribution with mean 0 and standard deviation of 10% error.

48 simulated granules are used for model training, 4 randomly sampled from

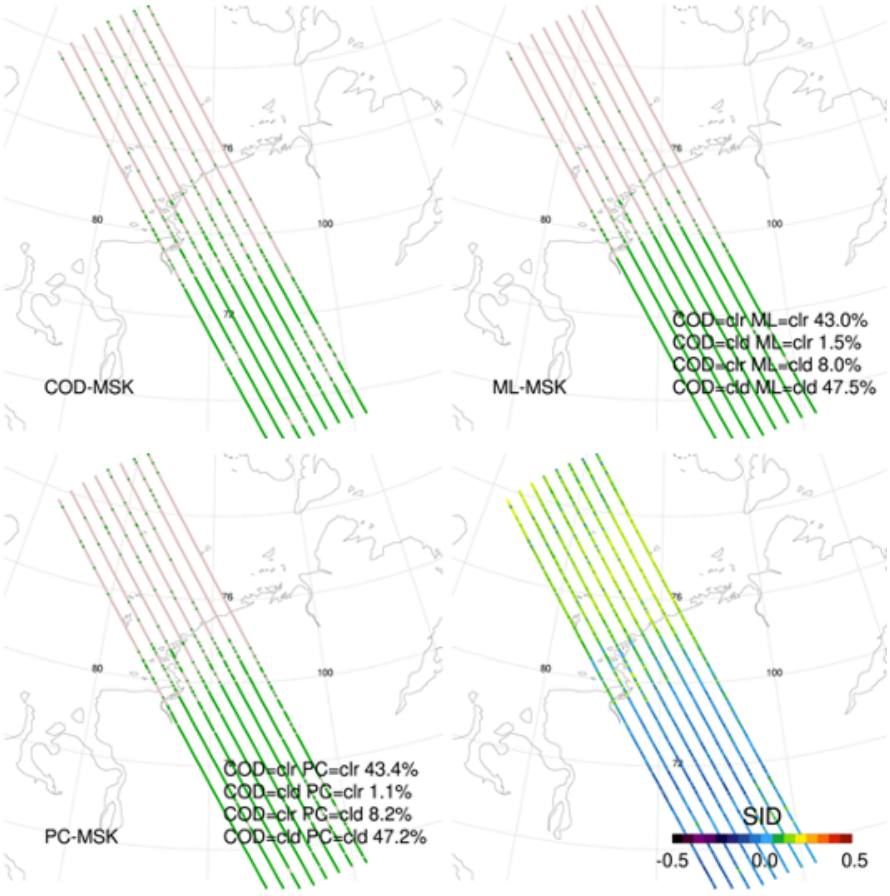

Figure 2.6: Similarity index (SI) for the same regions depicted in Figures 2.1 and 2.2

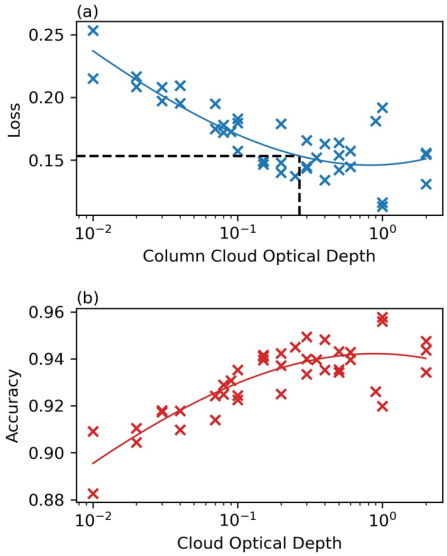

Figure 2.7: (a) The binary cross-entropy loss of neural networks with various COD thresholds demarcating "clear" vs "cloud" scenes. Solid lines are cubic functions fit to the evaluated points. Vertical dashed lines represent the TWP threshold corresponding to an evaluated loss that is 105% of the fit function's minimum loss (COD=0.25; horizontal dashed), this helps detect optically thin clouds. (b) The accuracy of the neural networks corresponding to the various COD thresholds depicted in (a). Horizontal dashed lines correspond to the accuracy for the same COD threshold depicted in (a).

each month. The loss used for training is binary cross entropy, defined as:

$$\text{Loss} = -\frac{1}{|\mathbf{Y}^*|}\sum\left[(1-\beta)\mathbf{Y}^*\log_{10}(\hat{\mathbf{Y}}) + \beta(1-\mathbf{Y}^*)(\log_{10}(1-\hat{\mathbf{Y}}))\right] \quad (2.5)$$

where $\mathbf{Y}^*$ is a binary set representing 'truth'. Clear is defined to be the null condition (0) and cloudy the alternate condition (1). $\hat{\mathbf{Y}}$ is the corresponding set of predicted probabilities by the NN for the cloudy class. Finally, $\beta = \frac{\sum \mathbf{Y}^*}{|\mathbf{Y}^*|}$, adjusts for imbalances between the number of cloudy versus clear scenes in the training set. For each individual prediction, the first term in Eq. 2.5 is equal to 0 if the scene is clear and the second term is equal to 0 if the scene is cloudy. This loss function designates that, statistically, the detection of clear and cloudy scenes should have equal effect on the overall model skill.

The skill of the model is not found to be particularly sensitive to the model architecture, however, for completeness the structure used for the NN is listed in Tab. 2.1. The use of batch normalization and dropout layers helps deter overfitting.

Table 2.1: The neural network structure for the cloud mask NN. Layer levels may be used as a reference for how inputs progress through the NN. Layer types and output shape are listed for each layer. The input shape takes the form of nchannels, referring to the number of 'clean' channels for that particular x-track scene, with two additional inputs for the ingested AUX-MET products.

Baseline NN Structure		
Layer Level	Type	Output Shape
1	Input	(None, nchannel+2)
	BatchNormalization	(None, 52)
2	Dense	(None, 256)
	Dropout(0.2)	(None, 256)
3	Dense	(None, 256)
	Dropout(0.3)	(None, 256)
4	Dense (softmax activation)	(None, 2)

To account for differences between sensors, 16 unique NNs are trained (2 TIRS instruments, each with 8 sensors). Each NN is trained with the same 48 granules, and architectures are identical except for the input layer, which only ingests the 'clean' channels for each sensor. Each NN evaluates only on its respective sensor and the output is combined to produce the final NN mask. Since NN training is inherently stochastic, each unique NN is retrained five times and only the best of the five training sessions (based on loss values for an independent set of granules not seen during training) is saved for operational

use. Additional training will take place after real data is collected and an independent means of validation is available.

Figure 2.8 depicts one of the sixteen NN's ability to detect clouds as a function of the estimated cloud top height (eCTH) and the COD. The model is particularly skillful at detecting high thick clouds. However, as would be expected, thinner lower clouds are more difficult to detect. Low confidences in predictions occur near the NN's COD threshold (0.25) since slight perturbations in COD may induce spectral signatures that shift the scene from one class to the other; conversely, high confidences occur well away from this threshold.

2.5 Using PC-MSK and NN-MSK

The ability to detect clouds is highly dependent on cloud type and the atmospheric and surface variability within a given scene. The primary purpose of L2-MSK is to confidently identify 80-90% of clear-sky scenes for scales of 15-50 km in the Arctic; thus the cloud detection will be optimized for this need. To ensure clear-sky detection with a high level of confidence, it is recommend that one uses PC-MSK and ML-MSK together. An uncertainty estimate is available with ML-MSK, while the SI value and Otsu's threshold value are reported with PC-MSK. These additional quantities should provide key additional information regarding the likelihood of clear-sky or cloudy-sky detected within a given TIRS scene. Possible approaches that leverage the synergistic use of PC-MSK and ML-MSK will be tested by the PREFIRE Science Team during the post-launch checkout phase.

2.6 Validation Plan

Initial validation of PC-MSK and ML-MSK will be performed against the VIIRS cloud mask and CrIMSS ECF for orbital segments that are not used in the formation of the training data sets. As with the identification of ideal training set radiances, the most optimal comparisons will be limited to small time differences ($\sim$minutes) between PREFIRE and JPSS. Inevitably, the time restriction is a function of variable atmospheric conditions, implying a more (less) restrictive time difference, for instance, when wind speed is higher (lower). The meteorological context will leverage the Aux-Met files to examine temporal differences between PREFIRE and JPSS coincidences as a function of both wind speed and direction shear. This initial validation effort will play a crucial role in optimizing the training data for the operational version of PC-MSK. We expect that the CrIMSS cloud products to be most similar to those derived from PREFIRE rather than the VIIRS cloud mask. CrIMSS will be available during daytime and nighttime observations, while the VIIRS cloud mask will be more limited at night. The advantage of VIIRS will be the order km-scale cloud cover and will be essential to quantify complicated scenes.

Surface classification using microwave (MW) channels from the ATMS instruments is used to distinguish ocean, ice-free land, ice-covered land, sea ice, glacier ice, and coastlines apart from each other. MW surface classification

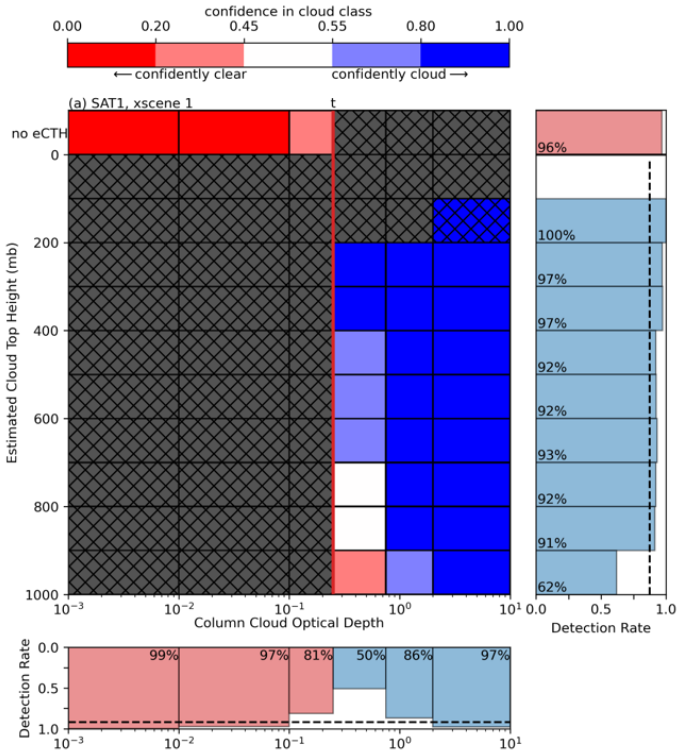

Figure 2.8: An example evaluation of the NN cloud mask (a) A 2D histogram of the assigned probability to the "cloud" class by the NN for scenes binned by estimated cloud-top height (eCTH, determined by the pressure in which the top-down integrated COD exceeds 0.1.) and the column cloud optical depth (COD) of the scene. Bins that contain less than 0.1% of the dataset are crossed and empty bins are gray. True clear scenes lie to the left of the designated COD threshold, whereas true cloud scenes lie to the right. All true clear scenes are binned together as having no eCTH (top) and thus are broken down only by a function of COD. Darker shades of blue indicate that the neural network is on average very confident that scene bin is cloud. Darker shades of red indicate that the neural network is on average very confident that scene bin is clear. White indicates little confidence one way or the other. (b) The detection rate (number of times correctly predicted "cloud" divided by the number of clouds within that bin) for cloud scenes as a function of eCTH. The mean cloud detection rate, over all eCTH levels, is plotted with a vertical dashed line. The clear detection accuracy is also listed at the top. (c) As (b), but as a function of the COD of the scene. The mean accuracy of the NN is plotted with a horizontal dashed line. In (b) and (c), blue bars indicate statistics relating to cloudy scenes, and red bars indicate statistics relating to clear scenes.

was previously used for quantifying PREFIRE sampling scenarios (Kahn et al. 2020). For the pre-launch algorithm development, the TIRS radiances simulated from GMAO data do not reflect real surface type variations. As the development of PC-MSK proceeds on actual TIRS data post-launch, the MW surface classification is anticipated to play a more important role to capture TIRS radiance dependence on surface type. The PC-MSK algorithm may use clear and cloudy sky training matrices derived for each surface type.

2.7 References

Bertossa, C., L'Ecuyer, T., Merrelli, A., Huang, X. and Chen, X., 2023. A neural network–based cloud mask for PREFIRE and evaluation with simulated observations. Journal of Atmospheric and Oceanic Technology, 40(4), pp.377-396.

Garay, M. J., S. P. de Szoeke, and C. M. Moroney (2008), Comparison of marine stratocumulus cloud top heights in the southeastern Pacific retrieved from satellites with coincident ship-based observations, J. Geophys. Res., 113, D18204, doi:10.1029/2008JD009975.

Kahn, B. H., B. J. Drouin, and T. S. L'Ecuyer (2020), Assessment of sampling sufficiency for low-cost satellite missions: Application to PREFIRE, J. Atmos. Ocean. Tech., 37, 2283–2298, doi: 10.1175/JTECH-D-20-0023.1.

Kahn, B. H., C. Bertossa, X. Chen, B. J. Drouin, E. W. Hokanson, X. Huang, T. S. L'Ecuyer, K. Mattingly, A. Merrelli, T. Michaels, N. B. Miller, F. Donat, T. Maestri, and M. Martinazzo (2023), The Polar Radiant Energy in the Far Infrared Experiment (PREFIRE) principal-component-based cloud mask: A simulation experiment, Atmos. Meas. Tech. Discuss., https://doi.org/10.5194/egusphere-2023-2463.

Maestri, T., W. Cossich, and I. Sbrolli (2019), Cloud identification and classification from high spectral resolution data in the far infrared and mid-infrared, Atmos. Meas. Tech., 12, 3521–3540, https://doi.org/10.5194/amt-12-3521-2019.

3 Level 2 Atmospheric Retrieval

PREFIRE Atmospheric Retrieval Algorithm Aronne Merrelli (ATM algorithm lead), Nathaniel Miller, PREFIRE Science Team August 2022

PREFIRE L2 ATM Algorithm Theoretical Basis Document

3.1 Introduction

This Algorithm Theoretical Basis Document (ATBD) describes the algorithms used to produce the 2B-ATM (clear sky atmosphere) product for the Polar Radiant Energy in the Far Infrared Experiment (PREFIRE). The 2B-ATM algorithm uses data from the Aux-Met (Auxiliary Meteorological analysis), 2B-MSK (Cloud mask), and the 2B-SFC (surface properties) products as prior information.

3.2 Instrument Overview

The spectrometer for PREFIRE, the Thermal Infrared Spectrometer (TIRS), collects spectral radiance measurements across a wavelength range of approximately 5 to 54 μm with a spectral sampling of 0.84 μm. The light is dispersed by a grating onto a 64x8 element detector array that measures 8 simultaneous spectra along the spectrometer slit. The first four channels respond to shortwave radiance ($< 3\mu$m) and are not planned to be part of the calibrated L1B dataset as there will be no calibration system for these wavelengths and no expectation of instrument performance. Due to the instrument design, there are two-channel gaps at approximately 7, 15, and 30 μm, at the boundaries of the order-sorting filters used to select for specific grating diffraction orders. The layout of the filters results in 54 usable channels covering most of the thermal infrared range. The actual flight detectors have individual bad detector elements which will imply a different number of valid channels between the 8 cross track spectra. While the spectral resolution is much lower than modern infrared sounders, the spectral information available, particularly in the Far Infrared Red (FIR) water vapor rotational absorption band, does allow for coarse vertical resolution temperature and water vapor profiles.

For the currently planned orbit, the ground footprint shapes of the 8 TIRS scenes are approximately 10x30 km (cross-track by along-track) rectangles, with the 8 scenes separated cross-track by 20 km gaps between them. The temporal sampling rate of TIRS with the currently planned orbit altitude results in along-track overlap of approximately 7/8 between consecutive measurements. For the baseline ATM algorithm, no attempt is made to combine these observations in anyway. In other words, each spectrum is treated as an entirely independent measurement. Future research will investigate whether the overlapping measurements can be combined in some way to reduce sensor noise.

Figure 3.1 shows a summary of the spectral response functions (SRFs) compared to a clear sky, standard atmosphere emission spectrum. The SRFs

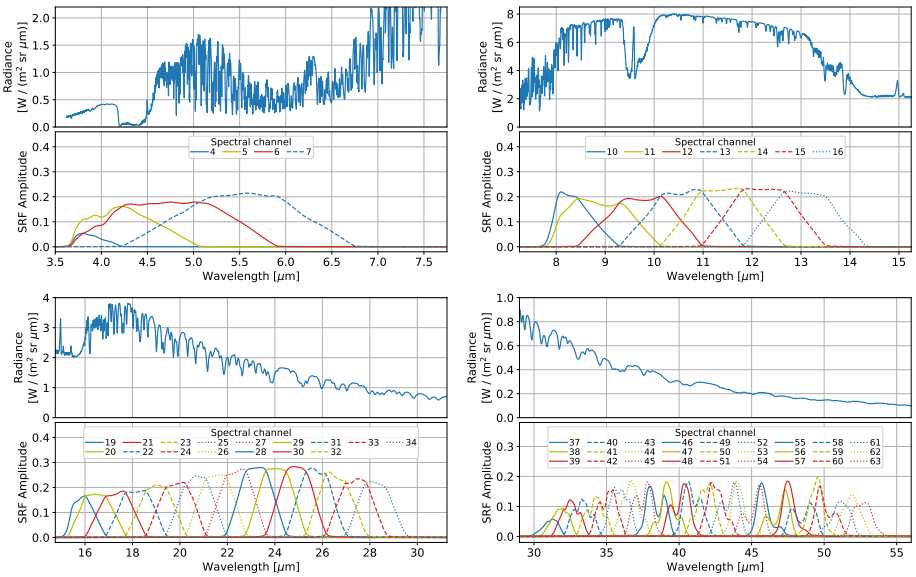

Figure 3.1: The TIRS SRFs grouped by the order sorting filter. In each panel, the upper plot is an emission spectrum from a standard atmosphere for comparison.

grouped according to the order sorting filter. Note the two channels (n) in the gaps between each grouping (n = 8, 9, 17, 18, 35, 36). Figure **??** shows sample weighting functions, for a standard atmosphere, across the primary wavelengths used for the ATM retrieval.

3.3 Overview

The ATM algorithm is a physical retrieval implemented with a standard optimal estimation approach (Rodgers, 2000) with a Levenberg-Marquardt parameter to adjust the weighting of the *a priori* and measurement information during iteration. The state vector consists of the temperature and water vapor vertical profiles and the surface temperature. The remaining relevant geophysical properties are taken as fixed from the values in the *a priori* datasets. The ATM algorithm is intended to run in clear sky only, so the processing is run only on the measurements identified as clear by the 2B-MSK product.

A priori information is derived from several sources in the PREFIRE SPDS processing chain and input into the 2B ATM algorithm, in order to create a final output data file. The output data file contains the final retrieval state at the coarse vertical resolution used in the 2B-ATM output product. Figure 3.3 shows the overall data flow.

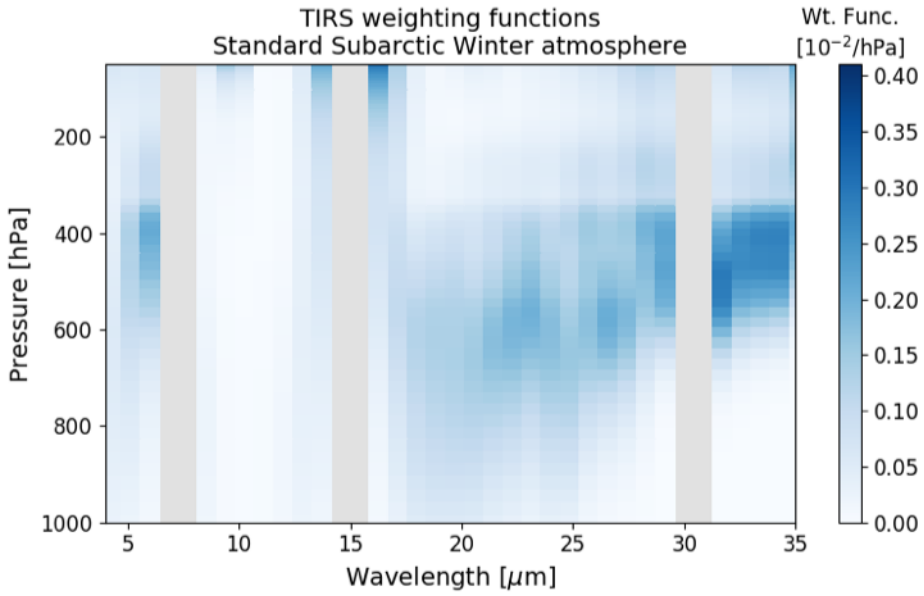

Figure 3.2: Sample TIRS weighting functions for the standard subarctic winter atmosphere, for $n = 4 - 40$.

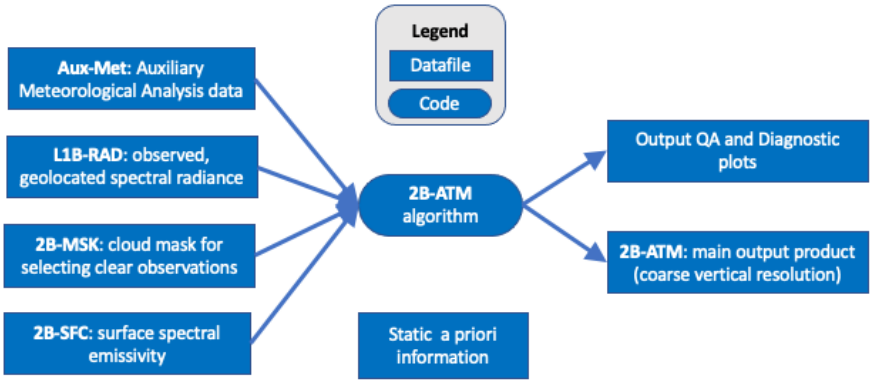

Figure 3.3: Algorithm Flowchart

3.4 Spectral Radiance Forward Model

The forward model used within the retrieval algorithm is the Principal-Components based Radiative Transfer Model (PCRTM) V3.4 (Liu et al., 2006). The PCRTM is an efficient and accurate plane parallel RT model, and uses a set of pre-computed Principal Components (PCs) describing a specific spectrometer sampling grid. The V3.4 implementation supports user defined profiles for the six primary infrared active molecules: water vapor, CO_2, O_3, CH_4, CO and N_2O. A number of other trace gases (such as CFCs) are included with fixed concentration profiles. The PCRTM can compute both the forward modeled radiance, as well as Jacobians for surface temperature, temperature profile, and concentration profiles for the six variable absorbers. A standard set of 101 fixed pressure levels defines the internal leveling grid for the forward model. To cover the FIR wavelengths measured by TIRS, we use a set of pre-computed coefficients constructed for a theoretical interferometer covering the wavenumber range 50 – 2760 cm^{-1} at a 0.5 cm^{-1} sampling grid. The high spectral resolution forward modeled spectra are converted to a wavelength grid and the TIRS channel Spectral Response Functions (SRF) are applied to generate TIRS channel radiances.

For the ATM algorithm, the PCRTM is operated in a clear sky only mode, though the PCRTM does contain ice and water cloud spectral emissivity models. This version of the PCRTM does not include capability to model the spectral reflectance, so the output will include only the thermal emission.

3.5 State and Measurement Vectors

The retrieved state vector for the ATM algorithm includes the temperature profile, $\mathbf{T}$, the logarithm of the water vapor mass mixing ratio profile, $\ln(\mathbf{Q})$, and the surface temperature T_s, combined into a single joint as follows:

$$\mathbf{x} = [\mathbf{T}; \ln(\mathbf{Q}); T_s] \tag{3.1}$$

The profile variables are defined in the full PCRTM vertical level resolution, but for only the levels, j, with pressures less than the surface pressure as defined by the Aux-Met product (in other words, only the levels above the surface topography are retrieved). This implies that the typical number of retrieved levels will be slightly less than 101, or as few as 80 for very high-altitude surface topography. The below surface levels are set to copies of the lowest altitude air temperature and water vapor mixing ratio. The below-surface values are input to PCRTM for the forward radiance calculation, but they are not included in the state vector meaning the values do not change during optimization. (Note that the first below surface level helps define the temperature and gas concentration of the partial layer containing the surface, so the below surface values do impact the modeled radiance).

The measurement vector is the measured spectral radiance, as described in the Instrument Overview, TIRS spectra will contain 54 valid spectral channels, less any identified bad detector elements. The shortest wavelength channels are not planned to be used in the ATM algorithm, in order to limit the impact of

scattered solar radiation on the algorithm and limit any day/night biases that would arise. Our forward model (PCRTM v3.4) does not model the spectral reflectance, so these channels at the short wavelength end would require significant extra modeling efforts to be utilized in the algorithm. In addition, the information content for water vapor and temperature profiling of these channels is a small fraction of the total, so removing these channels from the retrieval does not cause a significant performance degradation. If the detector at $n = 6$ is not flagged as poor quality, then we will we pay close attention its behavior in the flight data as this channel would be sensitive to both scattered solar radiation and non-Local Thermodynamic Equilibrium (LTE) emission in the 4.3 μm CO_2 absorption band (DeSouza-Machado et al. 2007). In addition, the longest wavelength channels (wavelengths larger than 40 μm) have relatively low signal to noise, and it may be necessary to remove several of these channels depending on their behavior in flight.

3.6 *A Priori* data

The OE algorithm requires *a priori* covariance matrices and mean values describing the expected probability distribution of the state vector before the measurement is examined. Since our *a priori* is derived from Auxiliary meteorological analysis data, the *a priori* mean will be direct copies of analysis fields interpolated to the TIRS observation location and time. The covariance should then represent our expectation of the probability distribution errors in the meteorological analysis fields relative to the true values. This error distribution should include error in the analysis field itself, as well as error incurred from the interpolation of the analysis grid and time to the actual observation location and time. In practice, this covariance is very difficult to accurately estimate. As an empirical approximation, we can compute distributions of analysis errors from comparing an analysis time step to the average of the bracketing time steps. For example, we can compare the field at 12UTC to the average of the fields at 09UTC and 15UTC (a $\pm$ 3 hour interpolation), or 06 and 18 UTC (a $\pm$ 6 hour interpolation). The averaged field is a proxy for the interpolation that will be done between a set of two analysis time steps and the arbitrary TIRS measurement time. This procedure should capture that part of the interpolation error, although it will not include any spatial interpolation. The covariance of these differences should capture realistic vertical error correlations, assuming the atmospheric transport within the analysis data is realistic. However, since this is not comparing the analysis data to an actual independent "truth" dataset, this method is likely to be an underestimate of the true error.

The SDPS will initially produce Aux-Met products from the GEOS-IT analysis data stream from NASA GMAO (Lucchesi, 2015) which will be available during the PREFIRE mission. To compute our initial covariance matrices, we used the above procedure on GEOS5 FP-IT data, which was available during algorithm development, before GEOS-IT was available. This data source has a time step of 3 hours for the three-dimensional variables (the temperature and water vapor fields), so in practice the interpolation time window would be a

Parameter	Upper atmosphere	Lower atmosphere
Surface T variance		$(2.0\ \mathrm{K})^2$
T variance	$(0.5\ \mathrm{K})^2$	$(2.0\ \mathrm{K})^2$
$\ln(Q)$ variance	$(0.3)^2$	$(0.6)^2$
T correlation scale	50 hPa	100 hPa
$\ln(Q)$ correlation scale	50 hPa	100 hPa

Table 3.1: Parameters defining the *a priori* covariance matrices for temperature and water vapor.

maximum of ± 1.5 hours to the arbitrary TIRS measurement times. We chose to use the interpolation from the ± 6 hour interpolation window as a way to compute a conservative estimate of the *a priori* covariance. In other words, this procedure will generate larger covariances in order to capture some of the known additional error sources that are not captured by the method. Finally, we approximate the computed covariances with an autoregressive correlation model (Lerner et al. 2003). This covariance model uses an exponential correlation model, so the covariance between two levels i and j, with variances σ_i^2 and σ_j^2, pressures p_i and p_j and a correlation scale p_L is given by (following Lerner et al. 2003, equation 7):

$$S_a(i,j) = \sigma_i \sigma_j \exp[-|p_i - p_j|/p_L] \tag{3.2}$$

Because the information content of TIRS observations is very low for the upper atmosphere ($p < 100$ hPa), we use a correlation scale length in pressure coordinates that enforces a high degree of correlation among these upper atmosphere levels. Different values are used for the correlation scales and variance in the lower and upper atmosphere, and a logistic function smooths the transition between the two regimes. Table 3.1 gives the values of variances and correlation scales in the upper and lower atmosphere used in the analytic covariance model. Figure 3.4 shows the shape of the correlation structure and variance for the temperature *a priori* matrix. The correlation matrix for $ln(Q)$, is the same, and no correlation is assumed between temperature and water vapor.

In addition to the temperature and water vapor profiles that are present in the retrieval state vector, there are many additional geophysical variables that can impact the modeled radiance. These other variables have low information content in the TIRS measurements, so cannot be retrieved, but should be specified accurately to minimize modeling errors. All of these additional variables are not included in the state vector, so their values will be fixed during optimization. These include the surface spectral emissivity and profiles of other infrared active molecules (CO_2, O_3, CH_4, CO and N_2O). The surface spectral emissivity will be taken the initial retrieval from the 2B-SFC product. For CO and N_2O, the fixed profile from the standard atmosphere is assumed for all observations. Since the O_3 profile has strong vertical and temporal variation, it will be taken from the Aux-Met product, after passing through the same temporal and spatial interpolation as the temperature and water vapor profiles. For CO_2 and CH_4, a

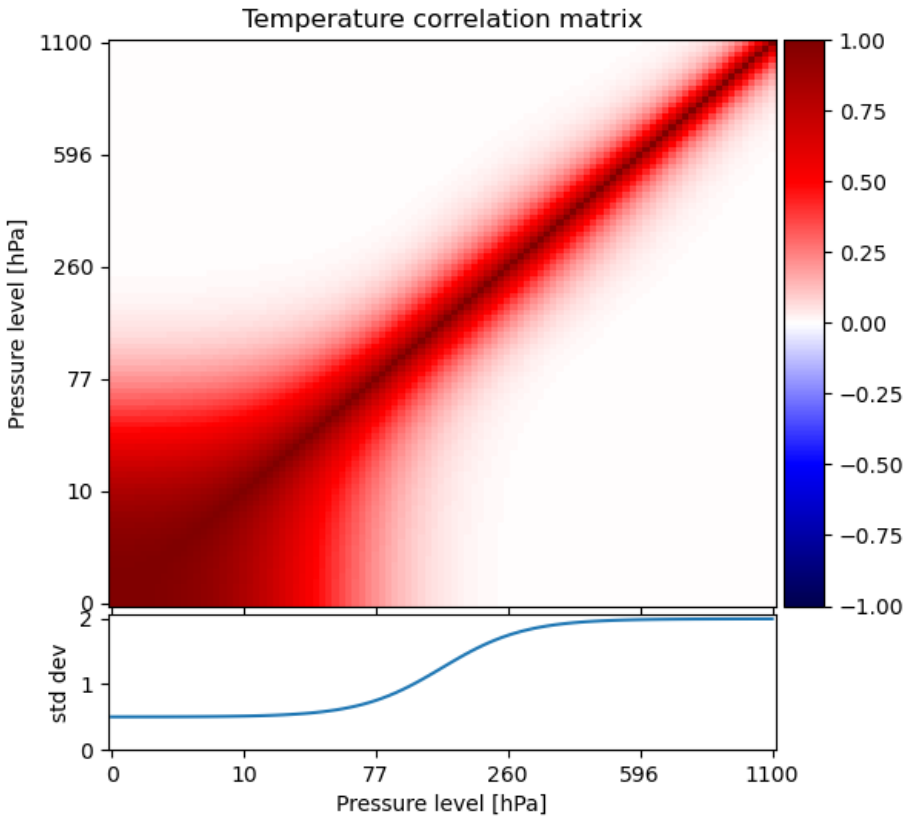

Figure 3.4: *A priori* temperature correlation and variance used in the retrieval.

fixed volume mixing ratio profile is used, based on a climatology developed from the Copernicus Atmospheric Modeling System (CAMS) EGG4 greenhouse gas reanalysis product (Agustí-Pareneda et al., 2022). The climatology models the EGG4 XCO_2 and XCH_4 (the total column-averaged dry air mole fractions) as a function of latitude and time. To compute the climatology, the daily EGG4 data from 2003 - 2020 was first averaged across longitudes to produce the zonal averages with time. The zonal averaged time series were then fit with harmonic series ($\sin + \cos$) and polynomial functions of time. These coefficients were then smoothed across latitudes with splines in order to reduce the overall dimensionality of climatology fits and to reduce noise across the individual latitude bands. Both CO_2 and CH_4 use linear polynomials. The CO_2 harmonic fit uses three terms, to fit annual and sub-annual cycles, while the CH_4 harmonic fit only uses one term. For each TIRS observation, the spline fits are evaluated at the observation latitude in order to determine the harmonic and polynomial coefficients, which are then evaluated to determine the CO_2 and CH_4 prior values. For an example with CO_2, assuming the spline fits yield the linear polynomial coefficients c_0, c_1 and the harmonic coefficients a_n, b_n, then the *a priori* CO_2 will be:

$$\mathrm{CO_2} = c_0 + c_1 t + \sum_{n=1}^{3} (a_n \sin(nt) + b_n \cos(nt)) \tag{3.3}$$

The evaluation for the CH_4 *a priori* value proceeds in a similar fashion, using fewer harmonic terms.

3.7 Inversion Method

The inversion method used in the ATM algorithm is a standard Bayesian nonlinear optimal estimation (OE) approach. Starting from an initial guess, the algorithm iterates the state vector, $\mathbf{x}$ value, recomputing the forward modeled spectral radiance and Jacobians at each step. The state vector updates at each iteration are the standard linear cost-function minimization steps. The method is similar to the standard Newton's method, with an additional Levenberg-Marquardt parameter to adjust the weighting of the *a priori* and measurement information during iteration (Rodgers 2000). This implementation closely follows the OE solver method used in the NASA OCO-2 L2 algorithm (Crisp et al., 2021).

The cost function is from the standard OE formalism, following from an assumed *a priori* state vector mean ($\mathbf{x_a}$) and covariance (S_a), a measurement vector ($\mathbf{y}$) and measurement error covariance ($\mathbf{S}_\epsilon$), and a forward model function ($\mathcal{F}$). For a particular iteration where the state vector value is $\mathbf{x_i}$, the cost function (c) is given by:

$$c = (\mathbf{y} - \mathcal{F}(\mathbf{x_i}))^T {\mathbf{S}_\epsilon}^{-1} (\mathbf{y} - \mathcal{F}(\mathbf{x_i})) + (\mathbf{x_i} - \mathbf{x_a})^T {\mathbf{S_a}}^{-1} (\mathbf{x_i} - \mathbf{x_a}) \tag{3.4}$$

At each iteration, the forward model returns the modeled measurement ($\mathcal{F}(\mathbf{x_i})$) as well as the Jacobian at the state vector value (K_i). These are used to compute

the state update, $\mathbf{dx_{i+1}}$. The actual state update is computed using a linear matrix solver (the `linalg.solve` function in NumPy, which utilizes LAPACK). The state update equation is given by:

$$[(1+\gamma)\mathbf{S_a}^{-1}+\mathbf{K_i}^T\mathbf{S_\epsilon}^{-1}\mathbf{K_i}]\mathbf{dx_{i+1}} = [\mathbf{K_i}^T\mathbf{S_\epsilon}^{-1}(\mathbf{y}-\mathcal{F}(\mathbf{x_i}))+\mathbf{S_a}^{-1}(\mathbf{x_i}-\mathbf{x_a})] \quad (3.5)$$

These quantities are computed for a scaled state vector, using the matrix $\mathcal{M}$ which contains the inverse square root of the diagonal of $\mathbf{S_a}$ along the diagonal. Multiplying by $\mathcal{M}$ scales the vector by dividing by the per-state variable standard deviation contained in the $\mathbf{S_a}$ matrix. This yields a slightly different form of equation 3.5, operating in the scaled state vector space:

$$\mathcal{M} = \begin{bmatrix} S_{a,(1,1)} & 0 & 0 \\ 0 & \dots & 0 \\ 0 & 0 & S_{a,(k,k)} \end{bmatrix}^{1/2} \quad (3.6)$$

$$\tilde{\mathbf{S}}_\mathbf{a} = \mathcal{M}^{-1}\mathbf{S_a}\mathcal{M}^{-1} \quad (3.7)$$

$$\tilde{\mathbf{x}} = \mathcal{M}^{-1}\mathbf{x} \quad (3.8)$$

$$[(1+\gamma)\tilde{\mathbf{S}}_\mathbf{a}^{-1}+\mathcal{M}\mathbf{K_i}^T\mathbf{S_\epsilon}^{-1}\mathbf{K_i}\mathcal{M}]d\tilde{\mathbf{x}}_\mathbf{i+1} = [\mathcal{M}\mathbf{K_i}^T\mathbf{S_\epsilon}^{-1}(\mathbf{y}-\mathcal{F}(\mathbf{x_i}))+\tilde{\mathbf{S}}_\mathbf{a}^{-1}(\tilde{\mathbf{x}}_\mathbf{a}-\tilde{\mathbf{x}}_\mathbf{i})] \quad (3.9)$$

After each iteration, the linearity of the forward model and cost function are assessed by comparing the value of the cost function after the state update (c_i+1) with a forecasted value of the cost function, assuming linearity, from the previous state value. The forecast value of the cost function relies on linear prediction of $\mathbf{y}$ at the current state:

$$\mathcal{F}(\mathbf{x_{i+1}}) \approx \mathcal{F}(\mathbf{x_i}) + \mathbf{K_i}\mathbf{dx_{i+1}} \quad (3.10)$$

The cost function forecast, c_{FC} is computed from equation 3.4, using equation 3.10 for $\mathcal{F}(\mathbf{x_{i+1}})$ and $\mathbf{x_{i+1}} \approx \mathbf{x_i} + \mathbf{dx_{i+1}}$. The ratio between the actual cost function change and the forecast cost function change, R, is calculated as:

$$R = \frac{(c_i - c_{i+1})}{(c_i - c_{FC,i+1})} \quad (3.11)$$

For a well-behaved update, the cost function at iteration i+1 should be smaller than i, and if it is linear then it should be close to the value of the forecast. In this case the ratio R should be close to 1. On the other extreme, for poorly-behaved updates, the cost function value may not change ($R = 0$) or even increase after the update ($R < 0$). Given these limiting values for R, we assign one of four labels for the state update: divergent updates ($R <$ 0.0001), moderately nonlinear updates ($0.0001 < R < 0.25$), weakly nonlinear ($0.25 < R < 0.75$), or linear updates ($R > 0.75$). During iteration, a divergent update triggers a change to the Levenberg-Marquardt parameter (λ_0 see below),

and the state update is discarded and recomputed with a new value of the λ_0 parameter. All other update types ($R > 0.0001$) will update the state vector using $\mathbf{dx_{i+1}}$.

The Levenberg-Marquardt λ_0 parameter controls a relative weighting between the *a priori* state estimate and the measurement. We start with a value of 10, and then update it during iteration with the following criteria, based on the classification of the state update by the cost function prediction method described above: For divergent updates or moderately nonlinear updates, λ_0 is increased by a factor of 10; for weakly nonlinear updates, λ_0 is unchanged, and finally, for linear updates, λ_0 is reduced by a factor of 2. The iteration is stopped when one of three exit criteria is reached: 1) the maximum number of iterations was reached, 2) the maximum number of divergent updates was reached, or 3) the state update was smaller than a threshold value. Retrievals that stop iteration by the third criteria are considered converged. The third criterion is evaluated by computing the size of the squared scaled state vector update relative to the current posterior error covariance, divided by the number state vector elements. This quantity (z) is compared against a threshold value of 0.1 to determine convergence:

$$z = \frac{1}{k}\mathbf{d\tilde{x}_{i+1}^{T}}\tilde{\mathbf{S}}^{-1}\mathbf{d\tilde{x}_{i+1}} \tag{3.12}$$

Each one of the criteria is set by an adjustable parameter that will be continually re-evaluated. Each of the thresholds can represent tradeoffs between algorithm throughput, yield, and accuracy, that will not be fully characterizable with pre-flight simulation testing. For example, more retrievals will converge if the iteration limit is increased, or higher accuracy might be obtained with smaller state update thresholds.

Finally, when the iterative algorithm stops, we perform a final forward model calculation to get the value of $\mathcal{F}(\mathbf{x}')$ at the retrieved state for the purposes of a χ^2 calculation to evaluate the goodness of fit and to compute the spectral residuals. The χ^2 is computed in the conventional way, given by equation 3.13. The number of degrees of freedom are taken from the trace of the averaging kernel matrix, $\mathbf{A}$, at the final state vector value. This allows for the calculation of the reduced χ^2, which is expected to be near a value of 1 for a successful retrieval. In the following equation, k is the number of variables in the state vector, and d is the number of degrees of freedom in the retrieval.

$$\chi^2_\nu = \frac{(\mathbf{y} - \mathcal{F}(\tilde{\mathbf{x}}))\mathbf{S}_\epsilon{}^{-1}(\mathbf{y} - \mathcal{F}(\tilde{\mathbf{x}}))}{k - d} \tag{3.13}$$

While the actual measurement vector used in the retrieval will be a subset of the total TIRS channels, the final forward model calculation will produce modeled radiances for all 54 valid channels. The full spectral model will be used for quality assessment as described in the section below.

3.8 Output processing

3.8.1 Layer specification of output profiles

Because the information content of the TIRS measurement is relatively low, the full vertical resolution profiles (the PCRTM standard 101 levels) are far more densely spaced than what is needed to capture the actual information content. This is particularly true in the upper atmosphere levels, where the full resolution includes 44 levels below 100 hPa. Before creating the final output product, the full resolution levels are grouped and combined into a smaller number of layers. A general heuristic is used to determine an appropriate grouping of the high vertical resolution levels based on the information content profile at the high vertical resolution. Starting from the TOA level, the information content profile is integrated downwards (with a cumulative sum), stopping when the total information reaches some threshold level. The threshold level should be less than one, otherwise the information content total would suggest the retrieval would have enough degrees of freedom for signal to retrieve partially independent sub-layers within the layer. Once the threshold level is surpassed, the level defines the bottom level that will be used in the combined layer. The process is repeated with the current level as the top level of the next combined layer.

The level combination process produces different level groupings for each individual profile. In particular, the process would produce a smaller number of combined layers for low information content profiles (high surface altitude, dry conditions). We desired a single layer specification that is applicable globally. Therefore, we determined the layer specification from an ensemble of tropical ocean profiles from ERA-5 reanalysis, as these will tend to have the highest total information content, and we determined a single set that is approximately the number returned from the average temperature profile. For simplicity, the same layer specification is applied to both the temperature and water vapor profile.

When the high-resolution profiles are combined, each low vertical resolution layer value is the mean of the associated high-resolution grouping. The posterior covariance matrix is computed by block averaging according to the same layer specification. The layer specification is shown in Table 3.2. The pressure boundaries of the coarse output levels are specified as the half-levels between the lower and upper pressure levels of the neighboring combined layers. Note that nearly the entire upper atmosphere ($p < 150$ hPa) is combined into one coarse output layer. The troposphere is then divided into six layers with pressure thickness ranging from approximately 120 – 170 hPa.

3.8.2 Quality assessment variables

The optimal estimation algorithm outputs several status variables that are used for quality assessment. These are combined into two quality variables. First, a summary integer flag (`atm_quality_flag`) with categorical values is provided. A second bit-flag (`atm_qc_bitflags`) that includes more detailed status information is included in the product. The summary integer flag should be sufficient for most uses, with the additional detail in the bit flags is available for more

Combined layer number	PCRTM level number range	Pressure range (hPa)	Pressure thickness (hPa)
1	1 – 51	0.005 – 156	156
2	52 – 64	156 – 307	151
3	65 – 72	307 – 433	126
4	73 – 79	433 – 565	132
5	80 – 86	565 – 718	153
6	87 – 93	718 – 892	174
7	94 – 101	892 – 1100	208

Table 3.2: Specification of the combined layers for the output product.

status value	Description
0	Best quality, converged retrieval
1	Poor quality, converged retrieval (reduced χ^2 exceeds threshold)
2	Retrieval did not converge
10	Retrieval not attempted due to presence of clouds as specified by Cloud flag in MSK product

Table 3.3: Description of ATM integer quality flag

advanced analysis of the product. The details of the flags will likely change with on-orbit data, but the intention is for the summary integer flag to retain the same definition, while the bit flags will likely include additional status conditions as needed.

The summary integer flag records the four main status conditions for the ATM algorithm within each TIRS observation. In brief, these are that no retrieval was attempted, or that a retrieval was attempted resulting in one of three outcomes: a good quality converged retrieval, a poorer quality converged retrieval, or an unconverged retrieval. These are listed in table 3.3 with the corresponding integer values. The bit flags give more detail about the convergence status, which can fail because either the diverging step or iteration count limits were reached, or an unphysical state vector value was reached during iteration. Additional status bits may be added once on-orbit data is analyzed. Table 3.4 describes the current set of bit flags within the pre-launch algorithm.

Threshold values for these QA variables are still under assessment using simulated data, and they will be re-evaluated as further refinements of the preflight noise models from TIRS become available. Ultimately, the thresholds will be reassessed again when flight data becomes available.

As described in the earlier section, when the retrieval is performed, the forward model is used to create a full spectral model even if a subset of the channels was used in the retrieval. If there are detector elements that have unexpected behavior on orbit, the modeled radiance may allow for assessment of the radiometric response relative to the "good" detector elements. For example, a

bit number	Status description
0	reduced χ^2 threshold exceeded
1	retrieval exceeded iteration count limit
2	retrieval exceeded diverging step count limit
3	retrieval went outside allowable state vector range
15	retrieval not attempted, due to cloud mask

Table 3.4: Descriptions of ATM quality flag bits

problematic channel could be evaluated by excluding it from the retrieval and analyzing the residuals (modeled minus observed radiance) in the retrieval output. These spectral residuals will be continually monitored during the mission. Furthermore, bulk statistics based on the fraction of converged retrievals and the averaged reduced χ^2 will be used to assess overall retrieval product quality. These values will be visualized separately for the eight TIRS spectra. Differences between the average performance among the eight spectra (for example, the distribution of χ^2 values) can indicate problems at the L1B calibration level.

3.9 Retrieval analysis: Information content and Uncertainty Characterization

Tests were performed with simulated measurements in order to assess the performance and uncertainties computed by the retrieval algorithm. The simulated measurements were generated from radiance simulations using the same forward model used in the retrieval (PCRTM, as described earlier), based on atmospheric profiles from ERA-5 reanalysis data (Hersbach et al. 2020) produced by the European Centre for Medium-range Weather Forecasts. The region locations reflect that PREFIRE is a polar-focused mission but will also produce global products. Three of the regions are polar (Arctic Ocean, Greenland Ice Sheet, Antarctica) and the fourth region is near the warm pool in the tropical Pacific Ocean. The full set of profiles thus spans a wide range of polar climate conditions, and also spans the range of cold/dry and warm/moist extremes we expect to observe globally. Figure 3.5 shows the locations of the four regions. For each region, we drew 8000 random samples from 2016 to yield a testing ensemble. Each profile produces a simulated radiance and Jacobian from PCRTM, which is then processed through the standard "Degrees of Freedom for Signal" (DFS) analysis (Rodgers, 2000) to assess the information content of the temperature and water vapor profiles. The TIRS information content is very strongly modified by the total water vapor amount, since the temperature information is relatively low because of the masked channels at 15 μm. Figure 3.6 shows a joint histogram of the DFS and total column water vapor (CWV) across the entire 32,000 profile ensemble.

The profiles are used to directly generate simulated observations with representative sensor noise, but then the retrieval is run with a perturbed profile as the first guess in conjunction with these simulated observations. The perturba-

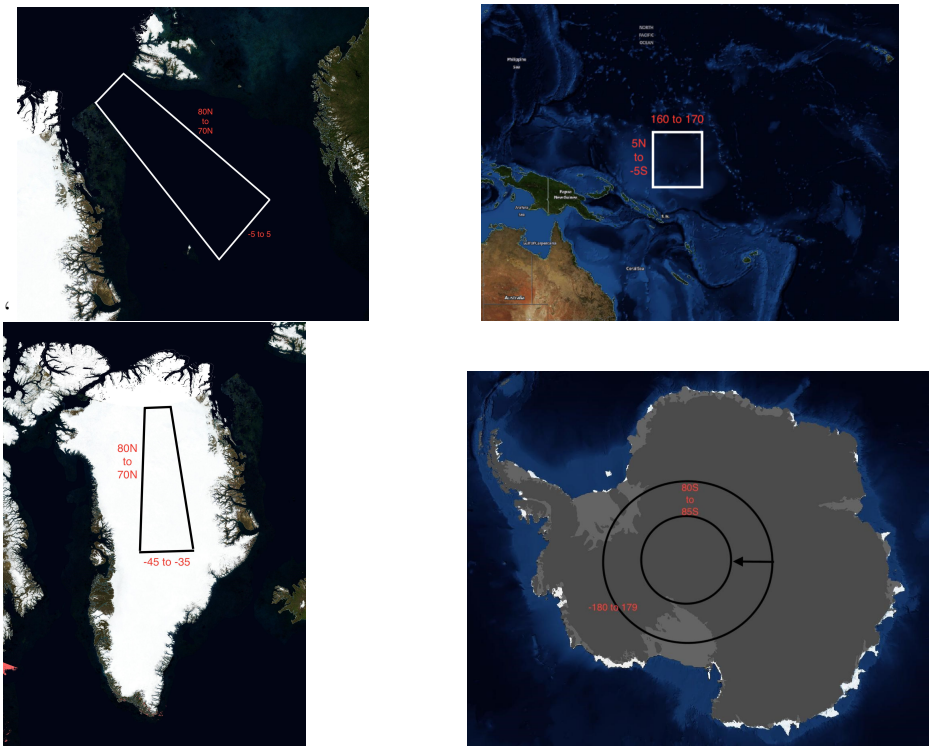

Figure 3.5: Regions where profile ensembles were extracted from ERA-5 reanalysis data: Upper left, Arctic Ocean (70^oN – 80^oN, 5^oW – 5^oE); upper right, tropical ocean (5^oS – 5^oN, 160^oW – 170^oE); lower left, Greenland (70^oN – 80^oN, 45^oW – 35^oE); Antarctica (80^oS – 85^oS). Images are from NASA Worldview.

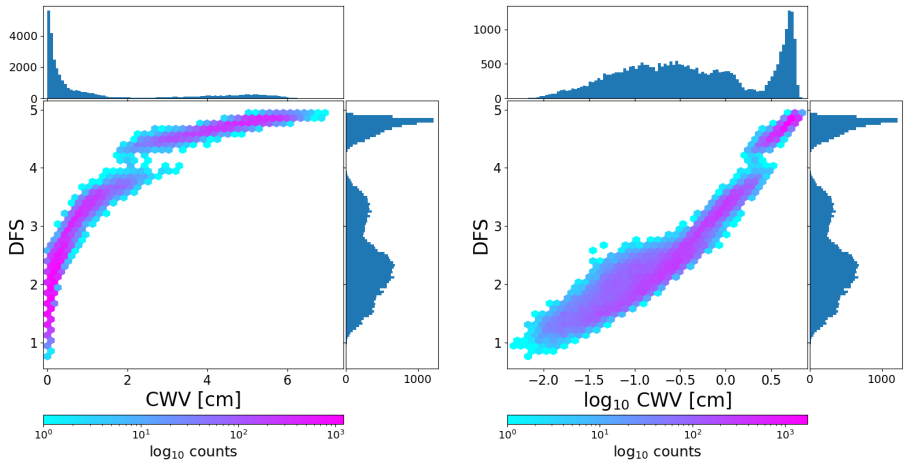

(a) Linear x-scale for CWV.

(b) Logarithmic x-scale for CWV.

Figure 3.6: Joint and marginal histograms of retrieval DFS (for temperature and water vapor profiles) versus a linear or logarithmic scaled total column water vapor (CWV). The data from the three polar regions populates a similar region in these two parameters, with the tropical data separated to larger values in both DFS and PWV.

tion is created as a correlated random variable, drawn from a covariance nearly equal to the prior. The same correlation structure is used, but the variance is constant with height rather than decreasing to a lower value in the upper atmosphere.

The retrieval is run on all selected profiles, and the statistics are pooled within each regional ensemble. The difference between retrieved and true profiles is characterized in terms of the precision (standard deviation of the differences) and accuracy or bias (mean of the differences). Furthermore, we examine the accuracy of the retrieval algorithm's reported uncertainty by computing the standard deviation of the scaled differences (z):

$$z = (\hat{\mathbf{x}} - \mathbf{x_{true}})/\epsilon_x \tag{3.14}$$

where the uncertainty (ϵ_x) is the posterior value computed by the retrieval algorithm. With accurate uncertainties, this quantity should be a normally distributed value with unit variance, meaning the standard deviation should converge to 1.

Figure 3.7 shows the results for the temperature profiles from the Arctic Ocean ensemble. The results from the other three regional ensembles are similar and omitted for brevity. The results are generally within expectations. In general, within the troposphere the reduction in uncertainty relative to the prior in the full set of retrieval levels ranges from 0.1 to 0.4 K. The level combining does increase the precision slightly. For example, the standard deviation in Fig-

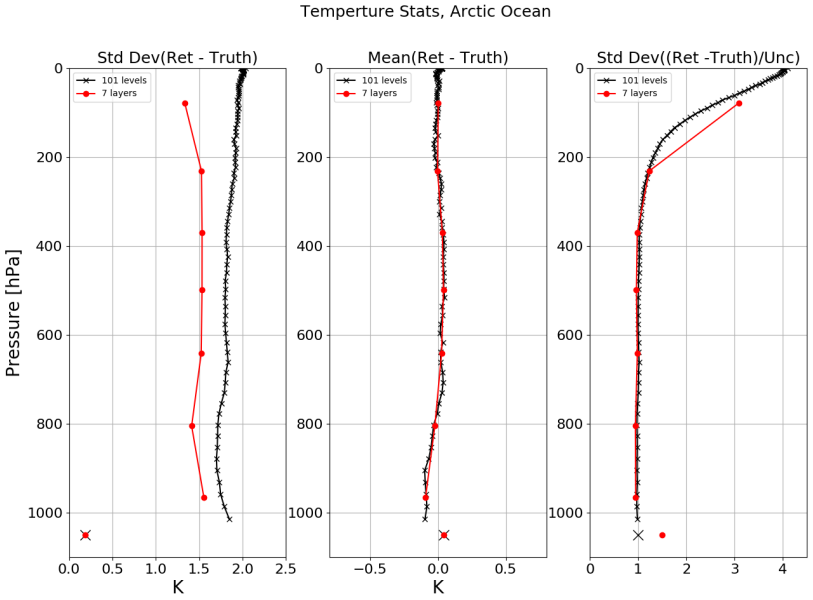

Figure 3.7: Evaluation statistics for temperature for the Arctic Ocean ensemble: (a) retrieval precision estimate, from the standard deviation of retrieval – truth differences; (b) retrieval accuracy estimate, from the mean of the differences; (c) accuracy of uncertainties, from the standard deviation of the scaled uncertainties. The original 101-level and combined 7-layer profiles are shown, with the surface temperature display as the separated single point at p=1050 hPa.

ure 3.7(a) drops from about 1.8 to 1.5 K, due to averaging out of uncorrelated error among the combined levels. The biases (middle column) are small, generally 0.1 K or less, with the larger biases generally occurring near the surface. Note that the scaled uncertainty is very close to 1 for the original and combined levels throughout the troposphere, demonstrating that the post processing calculations are handling the uncertainty propagation accurately through the level combining process. The scaled uncertainty increases to larger values in the upper atmosphere, here due to the perturbations being larger than the *a priori* assumptions. The measurements also have very little information about the upper atmosphere levels (note in **??**(a) that the standard deviation does not drop from the perturbation amplitude of 2K), so the retrieved state is very close to the prior.

Figure 3.8 shows the results for the water vapor profiles, displayed in a similar way as the temperature results in Figure 3.7. Since the water vapor profile retrieval is done in $\ln(Q)$ space, the accuracy and precision estimates are also shown in the $\ln(Q)$ space. The transformation back to linear space will introduce a bias itself, so it is important to isolate any possible bias from

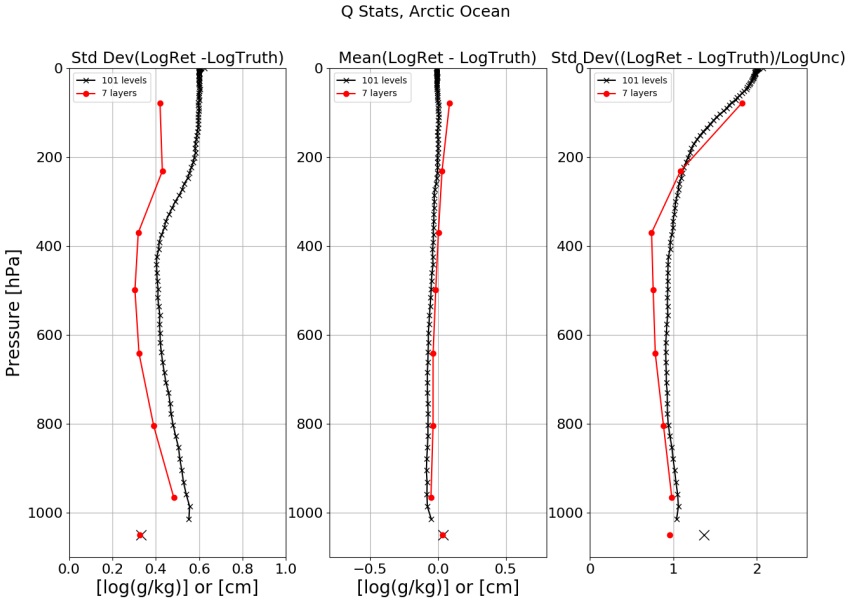

Figure 3.8: Water vapor evaluation statistics. Similar to Figure **??** (for temperature) but using the retrieval statistics in $\ln(Q)$ space. The separated point at p=1050 is the results for the CWV.

the retrieval itself. Displaying the results in $\ln(Q)$ space also makes it easy to relate to the variance of the *a priori*. The results for water vapor are largely the same as temperature, and there is again good consistency between the regional ensembles.

The primary output variable for the retrieval is the column water vapor (CWV). The CWV is simply the vertical integral of the water vapor profile, but it is important to ensure the uncertainty propagation through the integration is accurate. In Figure 3.8(c), the scaled uncertainties for the CWV computed from the original 101-level profile are slightly high, but after level combination the CWV integral uncertainty is very accurate. Table 3.5 lists the final CWV uncertainties observed across the four regional ensembles and gives a rough estimate of the overall uncertainty of global CWV estimates from the ATM retrieval.

3.10 Validation Plan

Comparisons of ground-based and air-borne measurements to PREFIRE water vapor level 2 products provide an independent gauge of the accuracy of the retrievals. Validation sources are critical to verifying the retrieved values are within the reported uncertainty. Ground-based stations, situated in

	Antarctica	Greenland	Arctic Ocean	Tropical Ocean
Mean CWV [cm]	0.111	0.201	0.880	4.92
Standard dev. [cm]	0.056	0.082	0.327	0.89
Fractional uncertainty (Std. dev./mean)	51%	41%	37%	18%

Table 3.5: Uncertainty estimates of column water vapor from the ATM retrieval.

the Arctic and Antarctica, have a lot of variation of data availability and measurement types. Direct measurements of the temperature and humidity profiles throughout the troposphere via radiosondes are extremely valuable, usually occur only once or twice a day at a given station. Sub-setting PREFIRE overpasses with station locations and known launch times throughout the mission provides a repository of data useful for statistical analysis. We will utilize the Integrated Global Radiosonde Archive (IGRA) v2 (Durre et al. 2006) which includes a consolidated distribution of radiosonde observations (ftp://ftp.ncdc.noaa.gov/pub/data/igra). Stations in Antarctica and the Arctic are most pertinent for the validation of PREFIRE products. In Antarctica, a majority of active stations in the IGRA are located along the coast as seen in Figure 3.9. The 14 stations labeled in Figure 3.9 will be used during clear-sky scenes to compare retrieved specific humidity profiles to direct measurements from radiosondes. In addition, column water vapor (CWV) estimates will be compared to the integrated water vapor from the radiosondes. The station located at the South Pole is not included as that latitude falls outside of the orbital range of PREFIRE. Specific station data usage is subject to data quality-control tests and availability over the mission period.

In the Arctic, there are 63 currently active stations in the IGRA that average one or more radiosonde launches per day and are north of 60^oN (Figure 3.10). Similar analysis to the Antarctic sites will be performed by comparing the Northern hemisphere sites to the subsampled PREFIRE data. In addition, the three sites labeled in Figure **??** have instruments designed to measure additional atmosphere state information, including high temporal resolution PWV estimates from microwave radiometers and various cloud properties. Specific station data usage is subject to data quality control tests and availability over the mission period.

The Simultaneous Nadir Overpass (SNO) method allows for comparison between PREFIRE and other polar-orbiting satellites (e.g., Cao et al. 2005) when the two similar nadir overpasses occur within small time difference. The Cross-track Infrared Sounder (CrIS) and Infrared Atmospheric Sounding Interferometer (IASI) derived products provide the ability to directly compare water vapor retrievals via SNOs. These comparisons of similar Earth scenes bring to light potential calibration issues, possible biases in water vapor retrievals, or scene dependent discrepancies.

Figure 3.9: IGRA station locations around Antarctica.

Figure 3.10: IGRA station locations around the Arctic Ocean.

3.11 References

Agustí-Panareda, A., Barré, J., Massart, S., Inness, A., Aben, I., et al.: Technical note: The CAMS greenhouse gas reanalysis from 2003 to 2020, Atmos. Chem. Phys., 23, 3829–3859, https://doi.org/10.5194/acp-23-3829-2023, 2023.

Cao, C., C., H. Xu, J. Sullivan, L. Mcmillin, P. Ciren, and Y. Hou, 2005: Intersatellite radiance biases for the High Resolution Infrared Radiation Sounders (HIRS) on-board NOAA-15, -16, and -17 from simultaneous nadir observations. J. Atmos. and Ocn. Tech., 22, 381-395.

Crisp, D., O'Dell, C., Eldering, A., Fisher, B., Oyafuso, F., et al., 2021. OCO (Orbiting Carbon Observatory)-2 Level 2 Full Physics Retrieval Algorithm Theoretical Basis, Tech. Rep. OCO D-55207, NASA Jet Propulsion Laboratory, California Institute of Technology, Pasadena, CA, Version 3.0 - Rev 1, available at: https://docserver.gesdisc.eosdis.nasa.gov/public/project/OCO/OCO_L2_ATBD.pdf (last access: Jun 4 2021),

Copernicus Atmosphere Monitoring Service: CAMS global greenhouse gas reanalysis (EGG4), CAMS Atmosphere Data Store (ADS) [data set], https://doi.org/10.24380/8fck-9w87, 2021.

DeSouza-Machado, S.G., Strow, L.L., Hannon, S.E., Motteler, H.E., Lopez-Puertas, M., Funke, B., Edwards, D.P., 2007. Fast forward radiative transfer modeling of 4.3 um nonlocal thermodynamic equilibrium effects for infrared temperature sounders. Geophys. Res. Lett. 34.

Durre, I., R. S. Vose, and D. B. Wuertz, 2006: Overview of the Integrated Global Radiosonde Archive. Journal of Climate, 19, 53-68.

GMAO website, last accessed 2022-06-24.https://gmao.gsfc.nasa.gov/GMAO_products/GEOS-IT/

Hersbach, H, Bell, B, Berrisford, P, et al. The ERA5 global reanalysis. Q J R Meteorol Soc. 2020; 146: 1999– 2049. https://doi.org/10.1002/qj.3803

Liu, X., Smith, W.L., Zhou, D.K., Larar, A., 2006. Principal component-based radiative transfer model for hyperspectral sensors: theoretical concept. Appl. Opt. 45, 201–209.

Lerner, J.A., Weisz, E., Kirchengast, G., 2002. Temperature and humidity retrieval from simulated Infrared Atmospheric Sounding Interferometer (IASI) measurements. J. Geophys. Res. 107, 4189. https://doi.org/10.1029/2001JD900254

Lucchesi, R., 2015: File Specification for GEOS-5 FP-IT. GMAO Office Note No. 2 (Version 1.4), 60 pp, available from `http://gmao.gsfc.nasa.gov/pubs/office_notes` .

Rodgers, C. (2000) Inverse Methods for Atmospheric Sounding: Theory and Practice. World Scientific Publishing Co Pte. Ltd.

4 Level 2 Spectral Emissivity

Optimal estimation retrieval of surface spectral emissivity Algorithm Theoretical Basis Document Yan Xie, Xianglei Huang and Xiuhong Chen April 9, 2021

Optimal estimation retrieval of surface spectral emissivity Theoretical Basis Document

4.1 Introduction

4.1.1 Purpose of preparing this document

This algorithm theoretical basis document (ATBD) describes the algorithm based on optimal estimation for the retrieval of surface spectral emissivity from radiance spectrum at the top-of-atmosphere (TOA). Specifically, this document describes the data, forward modeling, algorithm details and validation results of the retrieval study.

4.2 Data and Forward Modeling

4.2.1 ERA5 reanalysis data

The latest European Centre for Medium-Range Weather Forecasts (ECMWF) ERA5 reanalysis 6-hourly data (Hersbach et al. 2020) are used to simulate clear-sky PREFIRE radiances at nadir view. Surface temperatures, atmospheric temperature and humidity profiles of four months (January, April, July and October 2005) in the Arctic from ERA5 dataset will be used for the validation of surface spectral emissivity retrieval algorithm.

4.2.2 Band-by-Band surface emissivity dataset

A band-by-band surface emissivity dataset developed by Huang et al. (2016) is used in the study. This monthly-dependent global surface emissivity database is derived from first principles and observations, covering both mid-IR and far-IR at a $0.5^o \times 0.5^o$ spatial resolution.

4.2.3 PCRTM

Forward simulations of radiance spectrum at TOA are performed using the Principal Component Radiative Transfer Model (PCRTM) (Liu et al. 2006) because it is both computationally affordable and accurate. In this study, the PCRTM is employed to generate the synthetic radiances and Jacobians on the PREFIRE spectrum from 5 to 45μm at 0.86μm resolution. Detailed descriptions of the PCRTM are identical to Chapter 5 in the PREFIRE Spectral Flux ATBD by Xianglei Huang and Xiuhong Chen.

n	λ_n (μm)	ν_n (cm^{-1})	Transmittance in January	Transmittance in July
10	8.44	[1246.88, 1128.67]	0.85	0.73
12	10.13	[1030.93, 947.87]	0.80	0.73
13	10.97	[947.87, 877.96]	0.96	0.87
14	11.82	[877.96, 816.99]	0.96	0.83
15	12.66	[816.99, 764.53]	0.83	0.66
16	13.50	[764.53, 718.39]	0.48	0.35
20	16.88	[607.90, 578.03]	0.23	0.06
21	17.72	[578.03, 551.27]	0.45	0.10
22	18.57	[551.27, 526.59]	0.47	0.09
23	19.6	[526.59, 504.29]	0.39	0.05
24	20.25	[504.29, 483.79]	0.34	0.03
25	21.10	[483.79, 464.68]	0.28	0.02
26	21.94	[464.68, 447.23]	0.20	0.01
27	22.78	[447.23, 431.03]	0.16	0.00

Table 4.1: PREFIRE channels selected for the surface spectral emissivity retrieval. The atmospheric transmittances are calculated using MODTRAN5 with monthly and area mean profiles from ERA5 in January and July 2005 over the Arctic Ocean (73-77^{o}N, 0-360^{o}E).

4.3 Algorithm

?? demonstrates the flowchart of the surface emissivity algorithm.

4.3.1 PREFIRE channels selection

In this study, 14 PREFIRE channels in mid-IR and far-IR are selected out for the retrieval of surface spectral emissivity (Table 4.1). For monthly mean of ERA5 6-hourly profiles in Arctic Ocean, the transmittances in July are smaller than those in January, mostly due to the increase of water vapor abundance.

4.3.2 Optimal estimation retrieval

Optimal estimation method is a physical retrieval algorithm based on the Bayes' theorem.

$$(P(\mathbf{x} \mid \mathbf{y}) = \frac{(P(\mathbf{y} \mid \mathbf{x})P(\mathbf{x}))}{P(\mathbf{y})} \tag{4.1}$$

$P(\mathbf{x}|\mathbf{y})$ denotes the probability of a specific state $\mathbf{x}$ given the observation $\mathbf{y}$ and is known as the *a posteriori* probability density function (pdf). The state being optimized includes the geophysical variables:

$$\{T_s, \epsilon_n\} \in \mathbf{x}, \mathbf{y} \tag{4.2}$$

The optimal estimation retrieval method seeks the $\mathbf{x}$ which maximizes this *a posteriori* pdf. $P(\mathbf{x}|\mathbf{y})$ can be calculated using the likelihood of observations

given a specific state $P(\mathbf{y}|\mathbf{x})$ and the *a priori* probability distribution of the state $P(\mathbf{x})$. $P(\mathbf{y})$ functions as a normalization term and is not required in practice.

Observations $\mathbf{y}$ at TOA contain both radiances and the measurement noises. The PREFIRE observations are simulated by adding synthetic measurement noise ϵ to the clear-sky spectral radiances calculated by the PCRTM.

$$\mathbf{y} = \mathcal{F}(\mathbf{x}) + \epsilon \tag{4.3}$$

Gaussian distribution is widely used to model the pdfs due to its generality and convenience (Rodgers 2000). In this study, the likelihood $P(\mathbf{y}|\mathbf{x})$ and the *a priori* pdf $P(\mathbf{x})$ are assumed to be Gaussian. As a consequence, the *a posteriori* pdf $P(\mathbf{x}|\mathbf{y})$ also follows a Gaussian distribution.

$$\begin{gathered} \textit{A priori}\text{: } \mathbf{x} \approx \mathcal{N}(\mathbf{x_a}, \mathbf{S_a}) \\ \text{Likelihood: } \mathbf{y}|\mathbf{x} \approx \mathcal{N}(\mathcal{F}(\mathbf{x}), S_\epsilon) \\ \textit{A posteriori}\text{: } \mathbf{x}|\mathbf{y} \approx \mathcal{N}(\hat{\mathbf{x}}, \hat{\mathbf{S}}) \end{gathered}$$

$\mathbf{x_a}$ and $\mathbf{S_a}$ are the *a priori* mean and covariance matrix of the state $\mathbf{x}$, which represents the knowledge of state variables before observations. The observation $\mathbf{y}$ is composed of signals from the PCRTM forward model $\mathcal{F}$ given a specific state $\mathbf{x}$ and the noise quantified by the measurement error covariance matrix $\mathbf{S}_\epsilon$.

A priori knowledge of the state $\mathbf{x}$ can be obtained from climatological data, laboratory measurements or empirical analysis. In this study, the *a priori* mean $\mathbf{x_a}$ of surface spectral emissivity are set to 0.95 out of simplicity. The initial guess used in the iteration $\mathbf{x_0}$ is set equal to the *a priori* mean $\mathbf{x_a}$. The *a priori* covariance matrix $\mathbf{S_a}$ is derived from a recently developed surface emissivity database covering the far-IR spectrum (Huang et al. 2016). This global surface emissivity dataset is computed based on observations and first principles for each month at a $0.5^o \times 0.5^o$ spatial resolution. Monthly surface spectral emissivity at nadir view (0^o) is first converted to the PREFIRE spectrum. For each PREFIRE channel, find the dataset spectral grids which fall within the channel range. Surface emissivity on the PREFIRE channel is computed as the mean of observationally based surface emissivity at corresponding spectral grids.

Surface spectral emissivity dataset in the Arctic (60-90^{o}N, 0-360^{o}E) for all months are used to calculate the surface emissivity covariance matrix. The a priori covariance matrix S_a is generated by first multiplying the surface emissivity covariance matrix by 4, and then decreasing the correlation coefficient between different channels by half. This *a priori* constraint is not too strict so that signals from observations can be captured, neither too loose so that surface emissivity estimates still fall within a reasonable range. The measurement error covariance $\mathbf{S}_\epsilon$ is a diagonal matrix of which the main diagonal is composed of the square of the PREFIRE noise equivalent spectral radiance.

$\hat{\mathbf{x}}$ is the optimal estimate of the state, of which the uncertainty can be characterized by the *a posteriori* covariance matrix $\hat{\mathbf{S}}$. Theoretical formulas of

$\hat{\mathbf{x}}$ and $\hat{\mathbf{S}}$ can be conveniently derived based on Gaussian-distributed pdfs.

$$\hat{\mathbf{x}} = (\mathbf{K}^T {\mathbf{S}_\epsilon}^{-1}\mathbf{K} + {\mathbf{S}_\mathbf{a}}^{-1})^{-1}(\mathbf{K}^T {\mathbf{S}_\epsilon}^{-1}\mathbf{y} + {\mathbf{S}_\mathbf{a}}^{-1}\mathbf{x_a}) \tag{4.4}$$

$$\hat{\mathbf{S}} = (\mathbf{K}^T {\mathbf{S}_\epsilon}^{-1}\mathbf{K} + {\mathbf{S}_\mathbf{a}}^{-1})^{-1} \tag{4.5}$$

The optimal estimate $\hat{\mathbf{x}}$ can be viewed as a sum of *a priori* mean and observed signal weighted by the inverse of covariance matrices. The Jacobian matrix $\mathbf{K} = \delta F(\mathbf{x})/\delta\mathbf{x}$ describes the first derivative of the forward model with respect to a state variable.

For moderately linear cases, the Jacobian $\mathbf{K}$ can be used to invert observations in the measurement space back to the state space. Due to the dependence of Jacobian K on the state $\mathbf{x}$, it is necessary to iteratively solve the inverse problem and update the Jacobian at each iteration step. Therefore, optimal estimation algorithm uses the iterative Gauss-Newton method to find the root of $\nabla_\mathbf{x} = -ln(P(\mathbf{x}|\mathbf{y})$. The retrieval process is governed by the following iteration steps.

$$\mathbf{x_{i+1}} = \mathbf{x_a} + (\gamma_a^{-1} + {\mathbf{K_i}}^T {\mathbf{S}_\epsilon}^{-1}\mathbf{K_i})^{-1}{\mathbf{K_i}}^T {\mathbf{S}_\epsilon}^{-1}[\mathbf{y} - \mathcal{F}(\mathbf{x_i}) + \mathbf{K_i}(\mathbf{x_i} - \mathbf{x_a})] \tag{4.6}$$

$$\mathbf{S_i} = (\gamma_a^{-1} + [\mathbf{K_i}]^T {\mathbf{S}_\epsilon}^{-1}\mathbf{K_i})^{-1}(\gamma^2 {\mathbf{S}_\mathbf{a}}^{-1} + {\mathbf{K_i}}^T {\mathbf{S}_\epsilon}^{-1}\mathbf{K_i})(\gamma_a^{-1} + {\mathbf{K_i}}^T {\mathbf{S}_\epsilon}^{-1}\mathbf{K_i})^{-1} \tag{4.7}$$

Different from the classic formulations in Rodgers (2000), a tuning parameter γ is introduced to manually adjust the relative weight of *a priori* constraints and observed information (Carissimo et al. 2005, Zhou et al. 2007, Masiello et al. 2012, Turner et al. 2014). γ >1 means more information from the *a priori* than the observation. Following the work of Turner et al. (2014), a sequence of γ values [1000, 300, 100, 30, 10, 3, 1, 1, 1 ...] has been used in this study. This modification is meant to stabilize the retrieval process by gradually adding information from the observation step by step. The iteration will stop when γ=1 and the convergence criterion

$$((\mathbf{x_i} - \mathbf{x_{i+1}})^T [\mathbf{S_i}]^{-1}(\mathbf{x_i} - \mathbf{x_{i+1}}) < \frac{length(\mathbf{x})}{10} \tag{4.8}$$

is met. This convergence criterion makes sure that the change of $\mathbf{x}$ between two steps is smaller than the retrieval uncertainty by at least an order of magnitude.

4.3.3 Surface emissivity mapping

The mapping process transforms surface spectral emissivity on the PREFIRE channels to the PCRTM (sensor ID: 2) input spectrum covering 740 grids from 50.38 to 2759.89 cm^{-1}. For each PCRTM spectral grid, If its wavenumber falls in any PREFIRE channel, the surface emissivity at this PCRTM spectral grid will

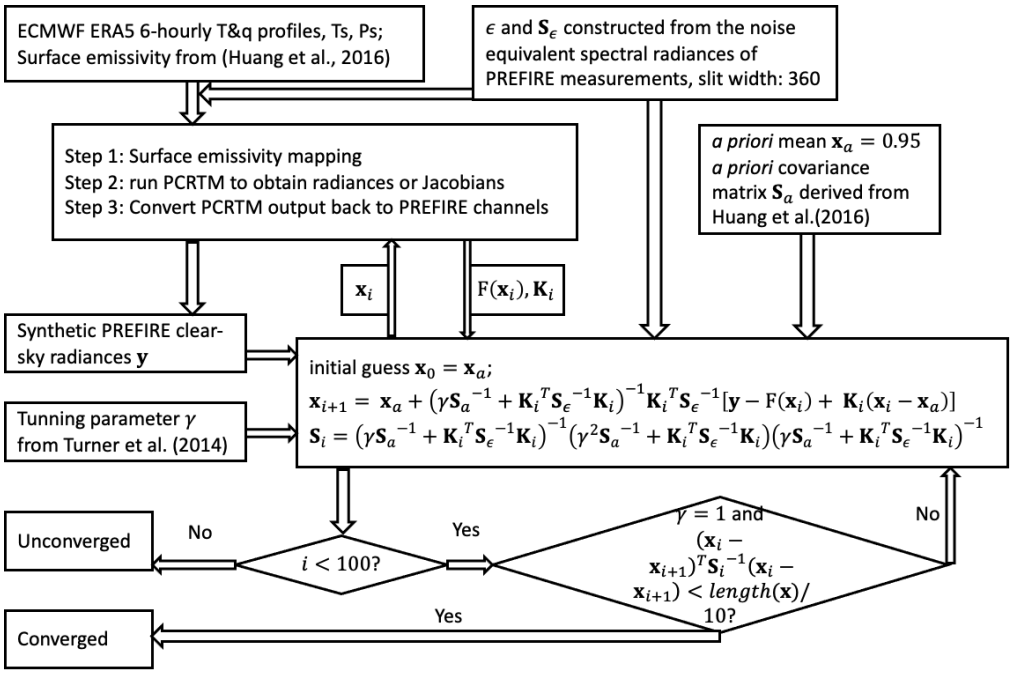

Figure 4.1: Flowchart of the optimal estimation algorithm for surface spectral emissivity retrieval on the PREFIRE channels.

be set equal to the value on that PREFIRE channel. If its wavenumber falls beyond the PREFIRE spectral range, the surface emissivity at this PCRTM spectral grid will be set equal to the value on the nearest PREFIRE channel, in other words, at $n = 10$ when wavenumber is smaller than 424.24 cm^{-1} or at $n = 27$ when wavenumber larger than 1228.07 cm^{-1}. If its wavenumber does not fall in any selected PREFIRE channel but still within the PREFIRE spectral range, the surface emissivity at this PCRTM spectral grid will be set equal to the value on the nearest PREFIRE channel, or the average of two adjacent channels if the PCRTM wavenumber happens to fall at the middle between two PREFIRE channels.

4.3.4 Conversion of PCRTM output back to the PREFIRE channels

The radiances and Jacobians generated by the PCRTM are on the 5421 spectral grids from 50 to 2760 cm^{-1} at 0.5 cm^{-1} spectral resolution. This output spectrum differs from that of PREFIRE, which means the radiances and Jacobians need to be converted back to PREFIRE channels. To solve this problem, spectral response function (SRF) and relevant spectrum information in the file "PREFIRE_SRF_v0.10.4_360_2021-03-28.nc" are used. The SRF (size: 6951 × 63) is on the spectrum of 6951 grids (0.43 - 60.00μm at 0.0086μm resolution) for all the PREFIRE channels. The PCRTM output $\mathbf{Y_0}$ (size: 5421 × 1) is first interpolated onto the SRF spectrum to get $\mathbf{Y_1}$ (size: 6951 × 1). For each selected PREFIRE channel, find the corresponding SRF column (size: 6951 × 1) and select out SRF spectral grids which fall within the channel spectral range. If (1) the sum of SRF column is positive and (2) the sum of $\mathbf{Y_{1on}}$ the selected spectrum is a real value, $\mathbf{Y_1}$ will then be convolved using the SRF column to derive $\mathbf{Y_2}$ on this PREFIRE channel.

$$\mathbf{Y_2} = \frac{\sum \mathbf{Y_1} \cdot SRFcolumn \cdot \Delta\lambda}{\sum SRFcolumn \cdot \Delta\lambda}, \Delta\lambda = 0.0086\mu m \tag{4.9}$$

Otherwise, the final output on this PREFIRE channel will be set as "Not a Number" (NaN).

4.4 Information content analysis

The information content analysis aims to evaluate the information contributed by the true state given noisy observations. In order to gain an insight before the actual conduction of retrievals, monthly mean profiles in three typical polar regions: Arctic Ocean (73-77^{o}N, 0-360^{o}E), Greenland (70-80^{o}N, 310-340^{o}E), Antarctic Plateau (75-85^{o}S, 60-90^{o}E) from ERA5 6-hourly reanalysis data in January and July 2005 are used for the information content analysis.

4.4.1 Averaging Kernel

The averaging kernel matrix, $\mathbf{A}$, (Backus et al. 1970) A quantitatively evaluates the sensitivity of retrieval results to the true state.

$$\mathbf{A} = \frac{\delta \hat{\mathbf{x}}}{\delta \mathbf{x}} = \mathbf{S_a K}^T (\mathbf{K S_a K}^T + \mathbf{S}_\epsilon)^{-1} \mathbf{K} \tag{4.10}$$

The columns of $\mathbf{A}$ describe the response of retrieval estimates to the change of a specific true state variable. The rows of this averaging kernel matrix represent the sensitivity of a specific retrieval estimate to all state variables. And the diagonal elements denote the sensitivity of a specific retrieval estimate to its own true value. This self-sensitivity is expected to be 1 in the ideal scenario.

Averaging kernels of surface emissivity in three typical polar regions: Arctic Ocean, Greenland and Antarctic Plateau are shown in Figure 4.2 for January and July in 2005. Each curve represents a row in the averaging kernel matrix. The *a priori* covariance matrix $\mathbf{S_a}$ is generated by first multiplying the emissivity covariance matrix by 4, and then decreasing the correlation coefficient between different channels by half. For Arctic Ocean and Greenland, the peak values of MIR channels are larger than 0.5 in January and July. In contrast, the peak averaging kernel values of FIR channels decrease in July mostly due to increased water vapor absorption.

4.4.2 Degree of Freedom for signal

Degree of freedom for signal d refers to the number of independent pieces of information concerning the true state that can be determined from a measurement. This value denotes how informative the observation can be given the measurement noise and the dependence among state variables. Degree of freedom for signal equals to the trace of averaging kernel matrix, in other words, the sum of self-sensitivity.

$$d = tr(\mathbf{S_a K}^T (\mathbf{K S_a K}^T + \mathbf{S}_\epsilon)^{-1} \mathbf{K}) = tr(\mathbf{A}) \tag{4.11}$$

The d values for signals shown in Table 4.2 are based on the 52 valid PREFIRE longwave channels. The *a priori* covariance matrix $\mathbf{S_a}$ is generated by first multiplying the emissivity covariance matrix by 4, and then decreasing the correlation coefficient between different channels by half. The DOF for surface emissivity in the MIR varies around 3 to 4, despite the change of total column water vapor. While the d for signal surface emissivity in FIR decreases when the total column water vapor increases. This implies that surface emissivity retrieval in the FIR can be significantly influenced by the water vapor abundance.

4.5 Validation

Synthetic clear-sky PREFIRE radiances are used to validate the surface emissivity retrieval algorithm. There are 960 profiles including ECWMF ERA5 6-hourly

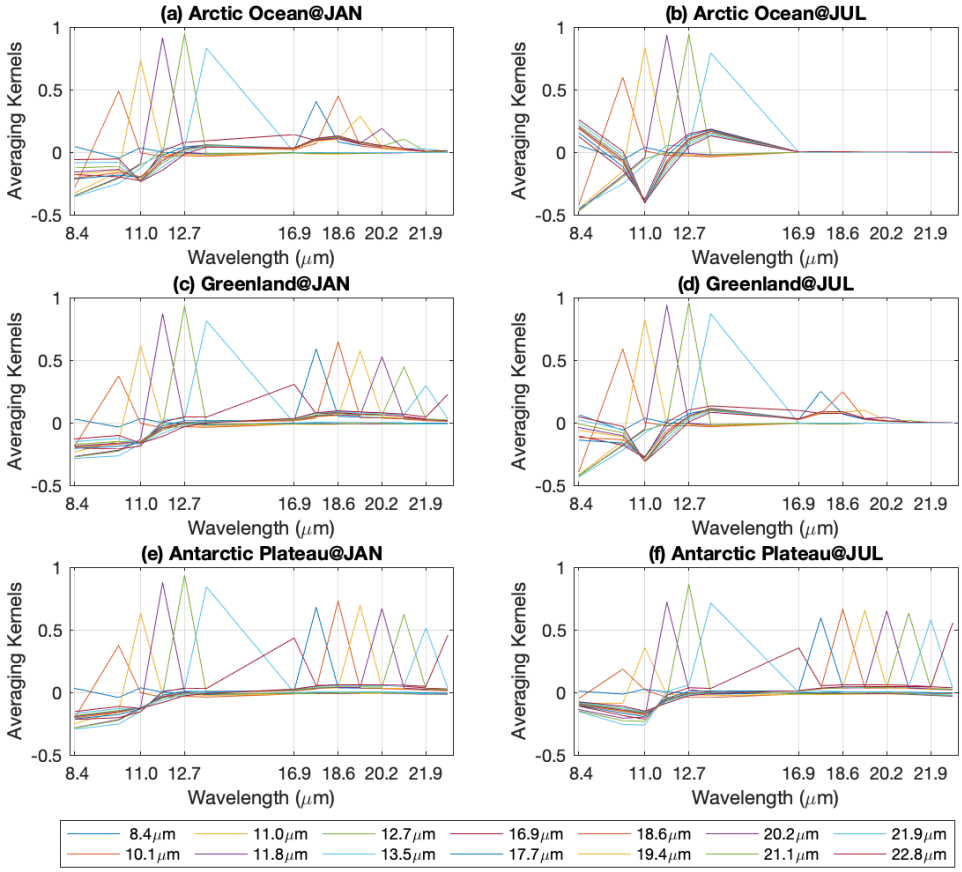

Figure 4.2: Averaging kernels of surface spectral emissivity in three typical polar regions: Arctic Ocean (73-77^{o}N, 0-360^{o}E), Greenland (70-80^{o}N, 310-340^{o}E), Antarctic Plateau (75-85^{o}S, 60-90^{o}E) calculated using ERA5 6-hourly reanalysis data in January and July 2005.

	Arctic Ocean		Greenland		Antarctic Plateau	
	JAN	JUL	JAN	JUL	JAN	JUL
d(T, q, T_s, ϵ_n)	9.6	8.4	10.9	8.6	11.8	11.8
$d(\epsilon_n)$	5.1	4.0	7.0	4.8	9.5	9.2
$d(\epsilon_{n_{MIR}})$	3.0	3.6	3.0	3.9	3.7	2.7
$d(\epsilon_{n_{FIR}})$	2.1	0.4	4.0	1.0	5.8	6.5
d(TCWV (cm))	0.30	1.27	0.12	0.59	0.07	0.02

Table 4.2: Degree of freedom, d, for signal and total column water vapor in three typical polar regions: Arctic Ocean (73-77^{o}N, 0-360^{o}E), Greenland (70-80^{o}N, 310-340^{o}E), Antarctic Plateau (75-85^{o}S, 60-90^{o}E) calculated using ERA5 6-hourly reanalysis data in January and July 2005.

temperature and humidity, surface temperatures and pressures randomly chosen in January, April, July, October 2005, 240 profiles for each month. Surface emissivity spectrums from the surface spectral emissivity database (Huang et al., 2016) are randomized by ± 0.05, and adjusted to 0.98 if the emissivity values exceed 1. The atmospheric profiles and surface properties are then fed into the PCRTM V3.4 to generate the synthetic clear-sky PREFIRE radiances without noise. The synthetic measurement noises are randomly derived from the normal distribution with zero mean and one standard deviation characterized by the PREFIRE noise equivalent spectral radiances. These random noises are then added to the radiances to generate the synthetic clear-sky PREFIRE radiances with noise. Both synthetic radiances without and with noise are used to retrieve surface spectral emissivity. Differences between the retrieved surface emissivity and the true surface emissivity values, namely the input to PCRTM, are investigated. Retrieval results using synthetic radiances without noise can validate the performance of the optimal estimation retrieval algorithm. On the other hand, results using synthetic radiances with noise can examine the accuracy level of surface emissivity retrievals in practice given the PREFIRE instrument noise.

Figure 4.3 shows the mean and root mean square error (RMSE) of absolute differences between the surface emissivity retrievals and the true values, using clear-sky synthetic PREFIRE radiances without noise. All of the 960 cases in four months converged within 10 iterations. The optimal estimation retrieval algorithm performs steadily on the MIR channels, with the bias mean plus RMSE falling within the range [-0.02, 0.01]. For channels in the FIR, mean of the absolute differences vary within ± 0.01. While the corresponding RMSEs are between 0.02 and 0.03, larger than those in the MIR. This increase of RMSEs is mostly attributable to cases in July and October.

Figure 4.4 shows the mean and root mean square error (RMSE) of absolute differences between the surface emissivity retrievals and the true values, using clear-sky synthetic PREFIRE radiances added with the instrument noise. Again, all of the 960 cases in four months converged within 10 iterations. The mean and RMSE of absolute differences show no significant difference compared to those in Figure 5.1. With the currently expected PREFIRE instrument noise,

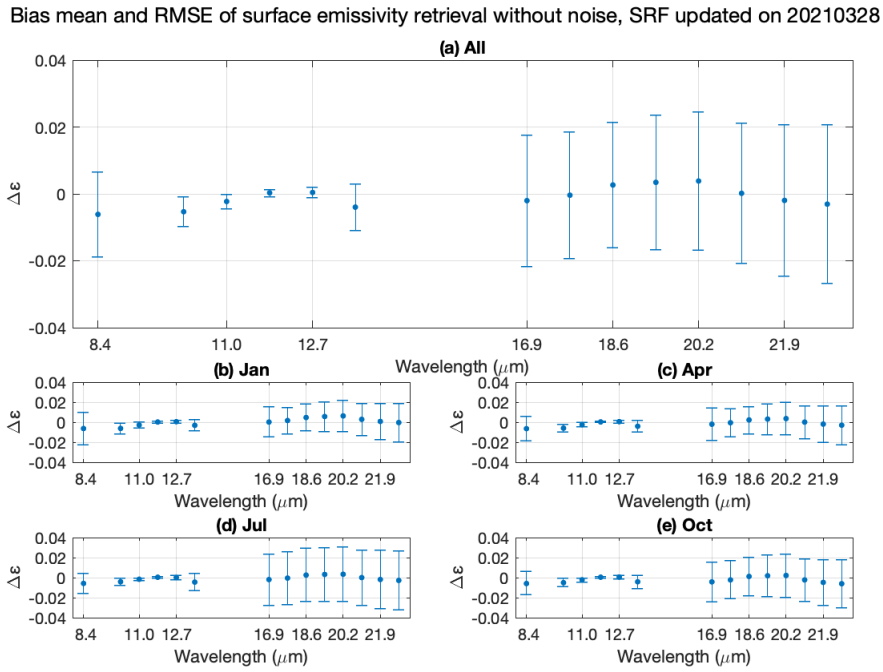

Figure 4.3: Mean (denoted by solid point markers) and Root Mean Square Error (denoted by bars) of absolute differences between the surface emissivity retrievals and the truth. The surface emissivity retrievals are derived from clear-sky synthetic PREFIRE radiances without noise. The panel (a) is based on retrieval results of all the converged cases. Subpanels (b), (c), (d), (e) characterize retrieval results in January, April, July and October respectively.

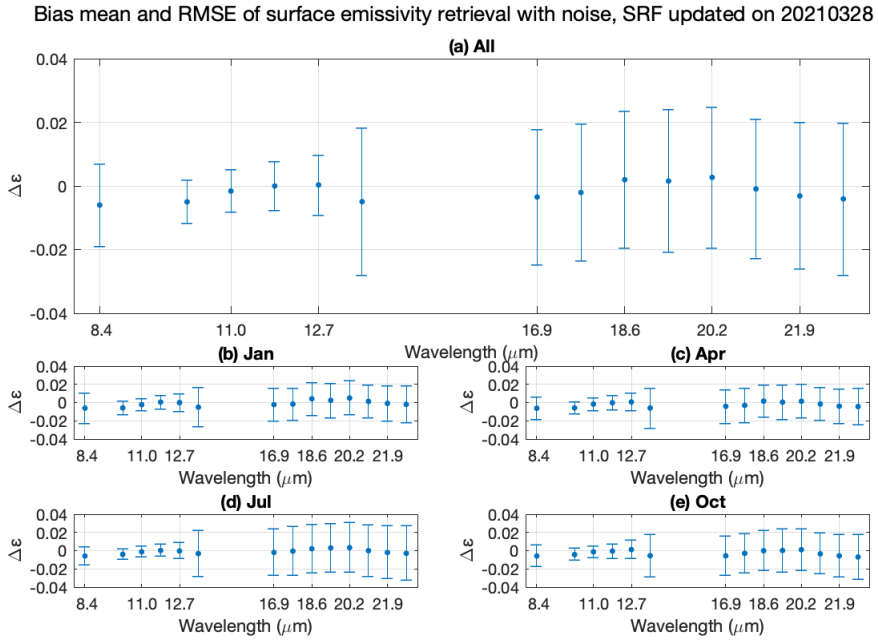

Figure 4.4: Similar to Figure 4.3 but surface emissivity retrievals derived from clear-sky synthetic PREFIRE radiances added with instrument noise.

the averaged surface emissivity retrieval will not be noticeably affected compared to the idealized retrieval without any noise.

4.6 An update

The algorithm can be applied to other PREFIRE SRF. We modified the PREFIRE SRF from version 10 ("PREFIRE_SRF_v0.10.4_360_2021-03-28.nc") to version 12 ("PREFIRE_TIRS1_SRF_v12_2023-08-09.nc" and "PREFIRE_TIRS2_SRF_v12_2023-08-09.nc"). Version 12 has different SRFs for two instruments: TIRS1 and TIRS2. Each instrument has 8 sensors. For the same instrument, all 8 sensors have the same SRF, but have different Noise-Equivalent Delta Radiance (NEDR), see Figure 5.3. We only do surface emissivity retrieval for channels with low NEDR (bitflag¡=1). Table 4.3 lists the channels used for surface emissivity retrievals for each sensor of TIRS1 and TIRS2. Then, they will be expanded to all 58 PREFIRE longwave channels using interpolation.

As validation, the surface emissivity retrieval algorithm is applied to synthetic PREFIRE radiance. Then the retrieved surface emissivity is compared with true emissivity used for simulating synthetic PREFIRE radiance. The synthetic PREFIRE radiance is simulated from GEOS-5 FP-IT analysis in four months of 2021 (three days in each month). Figures 4.5 and 4.6 show the mean and standard deviation of the difference between retrieved and true emissivity. Generally, the mean difference and standard deviation are larger for detected clear-sky cases than for truly clear-sky cases. Table 4.4 summarizes the difference between retrieved and true surface emissivities for channels used for retrieval. Overall, the median differences are all negative about -0.01 and the RMSEs are about 0.015-0.020. There are very small differences between TIRS1 and TIRS2.

4.7 References

Backus, G., and F. Gilbert. (1970), "Uniqueness in the Inversion of Inaccurate Gross Earth Data." Philosophical Transactions of the Royal Society of London. Series A, Mathematical and Physical Sciences, vol. 266, no. 1173, pp. 123–192.

Carissimo, A., I. De Feis, and C. Serio. (2005), "The physical retrieval methodology for IASI: The δ-IASI code". Environ. Model. Software, 20, 1111-1126.

Ebell, K., Löhnert, U., Päschke, E., Orlandi, E., Schween, J. H., and Crewell, S. (2017), "A 1-D variational retrieval of temperature, humidity, and liquid cloud properties: Performance under idealized and real conditions". J. Geophys. Res. Atmos., 122, 1746– 1766, doi:10.1002/2016JD025945.

Hanel, R. A., Schlachman, B., Rogers, D., and Vanous, D. (1971), "Nimbus 4 Michelson Interferometer", Appl. Opt. 10, 1376-1382

		Number of Channels used	Channels used for retrieving surface emissivity
TIRS1	Sensor 1	14	10 12 13 14 15 16 20 21 22 23 24 25 26 27
	Sensor 2	13	10 13 14 15 16 20 21 22 23 24 25 26 27
	Sensor 3	9	10 14 15 16 23 24 25 26 27
	Sensor 4	14	10 12 13 14 15 16 20 21 22 23 24 25 26 27
	Sensor 5	14	10 12 13 14 15 16 20 21 22 23 24 25 26 27
	Sensor 6	14	10 12 13 14 15 16 20 21 22 23 24 25 26 27
	Sensor 7	10	10 12 13 14 15 16 20 22 26 27
	Sensor 8	12	10 12 13 14 15 16 20 21 23 24 25 26
TIRS2	Sensor 1	13	11 12 13 14 15 19 20 21 22 23 24 25 26
	Sensor 2	13	11 12 13 14 15 19 20 21 22 23 24 25 26
	Sensor 3	13	11 12 13 14 15 19 20 21 22 23 24 25 26
	Sensor 4	12	11 12 14 15 19 20 21 22 23 24 25 26
	Sensor 5	13	11 12 13 14 15 19 20 21 22 23 24 25 26
	Sensor 6	13	11 12 13 14 15 19 20 21 22 23 24 25 26
	Sensor 7	11	13 14 15 19 20 21 22 23 24 25 26
	Sensor 8	13	11 12 13 14 15 19 20 21 22 23 24 25 26

Table 4.3: Number of channels and channels used for deriving surface emissivity for each sensor of TIRS1 and TIRS2.

Sensor	TIRS 1 Sim Performance			TIRS 1 Error Delta	TIRS 2 Sim Performance			TIRS 2 Error Delta
	5^{th}	95^{th}	median		5^{th}	95^{th}	median	
1	-0.027	0.015	-0.011	0.016	-0.030	0.016	-0.011	0.017
2	-0.023	0.014	-0.013	0.016	-0.025	0.016	-0.010	0.016
3	-0.035	0.011	-0.017	0.020	-0.019	0.018	-0.011	0.017
4	-0.019	0.016	-0.011	0.015	-0.024	0.014	-0.012	0.016
5	-0.037	0.016	-0.012	0.019	-0.028	0.015	-0.011	0.017
6	-0.022	0.016	-0.012	0.015	-0.024	0.015	-0.011	0.015
7	-0.021	0.018	-0.011	0.015	-0.026	0.010	-0.014	0.017
8	-0.024	0.015	-0.012	0.016	-0.024	0.014	-0.011	0.015
Aggregate	-0.025	0.016	-0.012	0.017	-0.025	0.015	-0.012	0.016

Table 4.4: 5^{th}, 95^{th} percentile, median value, and error Delta (root mean square error) of the absolute difference between retrieved and true surface spectral emissivity for TIRS1 and TIRS2. Aggregate value is from the combination of all 8 Sensors.

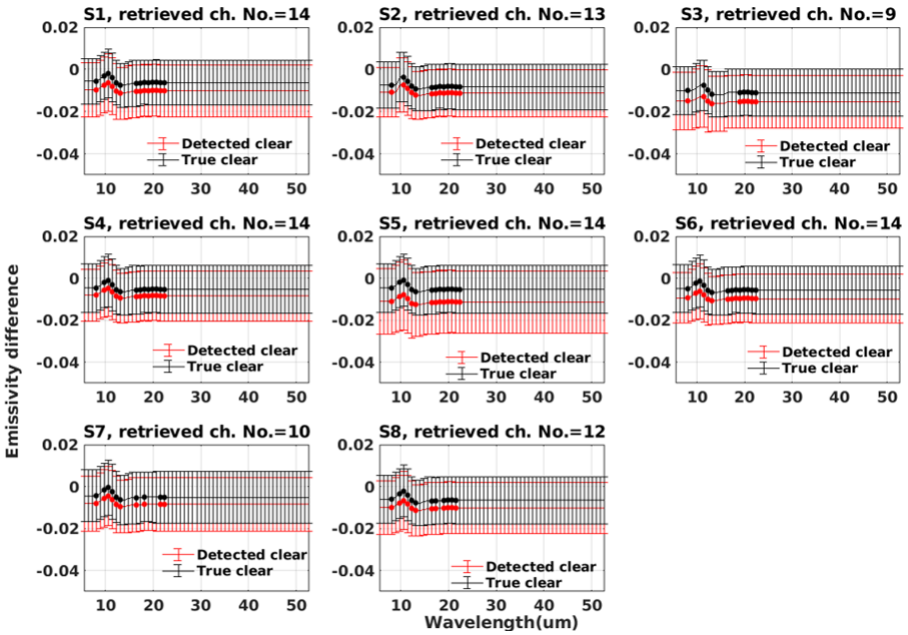

Figure 4.5: Mean and standard deviation of the difference between retrieved and true emissivity at PREFIRE channels for each sensor of TIRS1 over the polar regions. The black line is for cases that are purely clear sky. The red line is for cases that are detected as clear sky using the cloud mask algorithm. Dots are for the channels used for retrieval. Ticked vertical lines show the standard deviation of the difference.

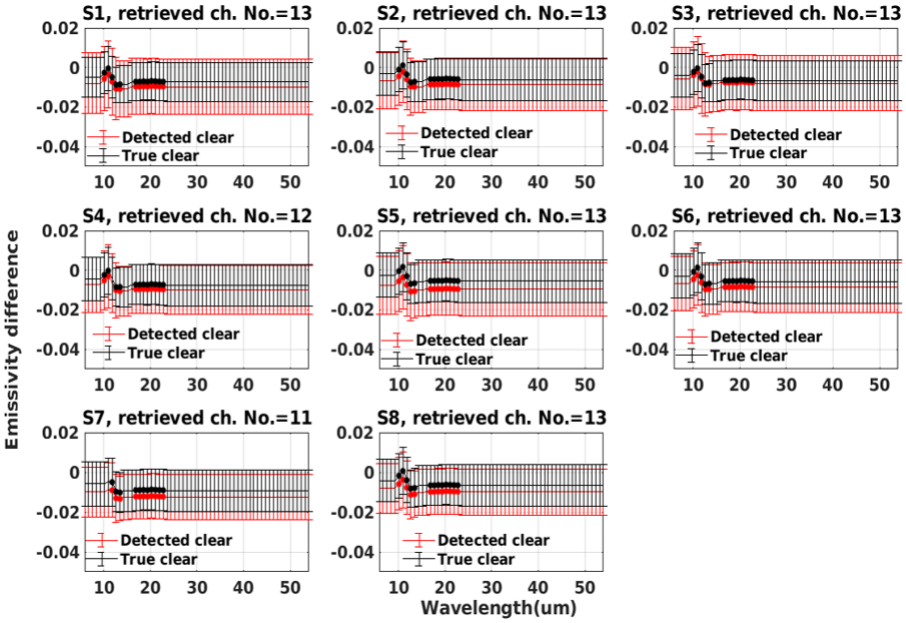

Figure 4.6: Same as Figure 4.5, but for TIRS2.

Hersbach, H, Bell, B, Berrisford, P, et al. (2020), "The ERA5 global reanalysis". QJR Meteorol Soc., 146: 1999– 2049.

Huang, X., Chen, X., Zhou, D. K., & Liu, X. (2016), "An Observationally Based Global Band-by-Band Surface Emissivity Dataset for Climate and Weather Simulations", Journal of the Atmospheric Sciences, 73(9), 3541-3555.

Liu, X., Smith, W. L., Zhou, D. K, and Larar, A. (2006), "Principal component-based radiative transfer model for hyperspectral sensors: theoretical concept", Appl. Opt. 45, 201-209

Masiello, G., Serio, C. and Antonelli, P. (2012), "Inversion for atmospheric thermodynamical parameters of IASI data in the principal components space", Q.J.R. Meteorol. Soc., 138: 103-117.

Rodgers, C. D. (2000). "Inverse Methods for Atmospheric Sounding: Theory and Practice", World Scientific.

Turner, D. D., & L ohnert, U. (2014). "Information Content and Uncertainties in Thermodynamic Profiles and Liquid Cloud Properties Retrieved from the Ground-Based Atmospheric Emitted Radiance Interferometer (AERI)", Journal of Applied Meteorology and Climatology, 53(3), 752-771.

Zhou, D. K., Smith, W. L., Sr., Liu, X., Larar, A. M., Mango, S. A., & Huang, H. (2007). "Physically Retrieving Cloud and Thermodynamic Parameters from Ultraspectral IR Measurements", Journal of the Atmospheric Sciences, 64(3), 969-982.

5 Level 2 Spectral FLux

PREFIRE Spectral Flux Algorithm Theoretical Basis Document Xianglei Huang and Xiuhong Chen April 9, 2021

PREFIRE Spectral Flux Algorithm Theoretical Basis Document

5.1 Introduction

5.1.1 Purpose

This algorithm theoretical basis document (ATBD) describes the algorithm used to derive the PREFIRE (Polar Radiant Energy in the Far-InfraRed Experiment) spectral flux product from observed PREFIRE spectral radiance. The product is included in the PREFIRE Level 2 (L2) product. Specifically, this document describes the data, forward modeling tool and algorithm details, and validation results. We derive both clear-sky and overcast-sky spectral flux at PREFIRE longwave channels ranging from 5 to 54 μm (PREFIRE channels 6 - 63) over polar regions.

5.2 Data Sets and Forward Modeling Tool

The PREFIRE Spectral fluxes are derived from PREFIRE radiances based on spectral ADMs for different sub-scene types and different surface types. Spectral ADMs were built offline using a forward radiative transfer model (PCRTM version 3.4) and using 6-hourly profiles from ECMWF ERA5 reanalysis. The sub-scene type is also sometimes referred to as "discrete interval" in the CERES SSF algorithms (Loeb et al. 2005).

5.2.1 PREFIRE

There are two 6U CubeSats in PREFIRE (SAT1 and SAT2), which are in distinct 470–650 km altitude, near-polar (82^o-98^o inclination) orbits each carrying a miniaturized IR spectrometer (TIRS1 and TIRS2; each instrument has 8 sensors), covering 0- 54 μm at $\sim$0.84 μm spectral resolution, operating for one seasonal cycle (a year) (https://prefire.ssec.wisc.edu/). PREFIRE measurements are at nadir view and over the polar regions. Channels 8, 9, 17, 18, 35 and 36 have zeros spectral response function. So these six channels have invalid measurements. Also, some channels having large noise are also not used. Table 5.1 shows the number of channels and specific PREFIRE channels used to derive spectral flux. Spectral fluxes at all 58 longwave channels are derived based on these filtered radiances at valid channels and corresponding ADMs following Loeb et al., 2005, Huang et al.(2008; 2010; 2014), and Chen et al. (2013).

Figures 5.1, 5.2 and 5.3 show the SRF for each channel and Noise-Equivalent Delta Radiance/Temperature for channels used for deriving spectral flux, respectively, based on PREFIRE SRF files

	Sensor	Number of Channels used	Channels used for deriving spectral flux
TIRS1	1	51	6-7 10 -16 19-34 37-50 52-63
	2	47	6-7 10 13-16 19-34 37 39-52 54- 62
	3	45	6-7 10 11 14-16 19 23-34 37-42 44 -60 62-63
	4	52	6-7 10 -16 19-34 37-63
	5	45	6-7 10-16 19-29 31-34 37-49 52 55-57 60- 63
	6	49	6-7 10 -16 19-27 29-34 37-51 53 55-63
	7	45	6-7 10 -16 19-20 22 26-34 37 39-56 58-59 61-63
	8	46	10 12 -16 19-21 23-26 28-34 37-56 58-63
TIRS2	1	46	6-7 10-15 19-34 37 40-47 50-62
	2	51	6-7 10-15 19-34 37-63
	3	21	6-7 10 -16 19 -27 29-31
	4	48	6-7 10-12 14 15 19-28 30-34 37-51 53-63
	5	32	6 -7 10-16 19-34 37-38 40-42 44 53
	6	42	6-7 10-15 19-31 41-43 45-51 53-63
	7	24	6-7 10 13-16 19-29 31-34 38-39
	8	36	6-7 10-16 19-31 38 41-43 46-49 51 53-54 58 61-62

Table 5.1: Number of channels and channels used for deriving PREFIRE spectral flux for each sensor of TIRS1 and TIRS2.

`PREFIRE_TIRS1_SRF_v12_2023-08-09.nc` and
`PREFIRE_TIRS2_SRF_v12_2023-08-09.nc`.

5.2.2 ECMWF Reanalysis

The latest European Center for Medium Range Weather Forecasting (ECMWF) ERA-5 reanalysis (Hersbach et al. 2020) are used to simulate clear-sky PREFIRE radiance and flux at nadir view. ERA-5 is based on the Integrated Forecasting System (IFS) Cy41r2, which was operational in 2016. ERA-5 has replaced the popularly used ERA-Interim reanalysis (Dee et al., 2011) by using 12-hourly ten-member ensemble 4D-Var scheme. ERA-5 has assimilated lots of historical satellite and *in-situ* observations and forcing from the improved radiation system and sea-surface boundary conditions. The temperature, wind, and humidity in the troposphere are improved compared to ERA-Interim. ERA-5 has archived hourly and high spatial resolution data. The vertical pressure levels are still the same as in ERA-Interim (37 levels from the surface to 1hPa). We only used the 6-hourly profiles of temperature, humidity, as well as surface skin temperature and surface pressure at 1.5^o by 1.5^o grids for simulations. We use four months (January, April, July and October) of data in 2005 for ADM construction.

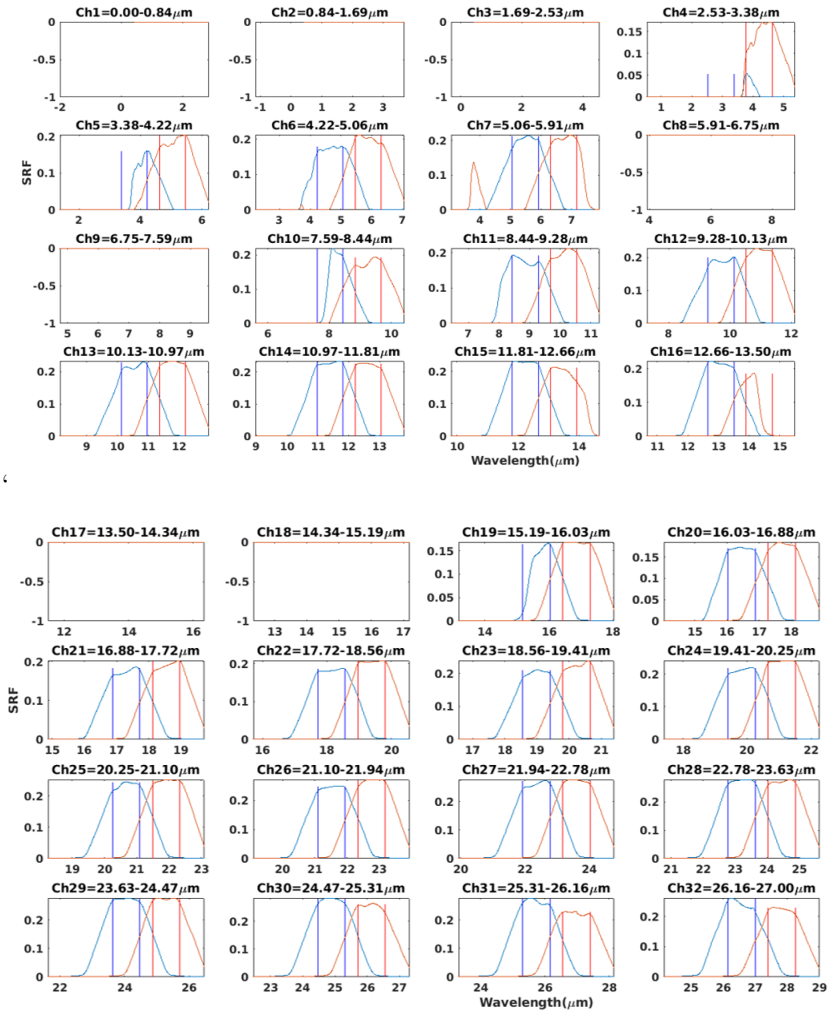

Figure 5.1: Spectral response function for PREFIRE channels 1-32, slit width = 360 μm. Vertical lines show the lower and upper bounds of each channel. Blue lines are for TIRS1 and red lines are for TIRS2.

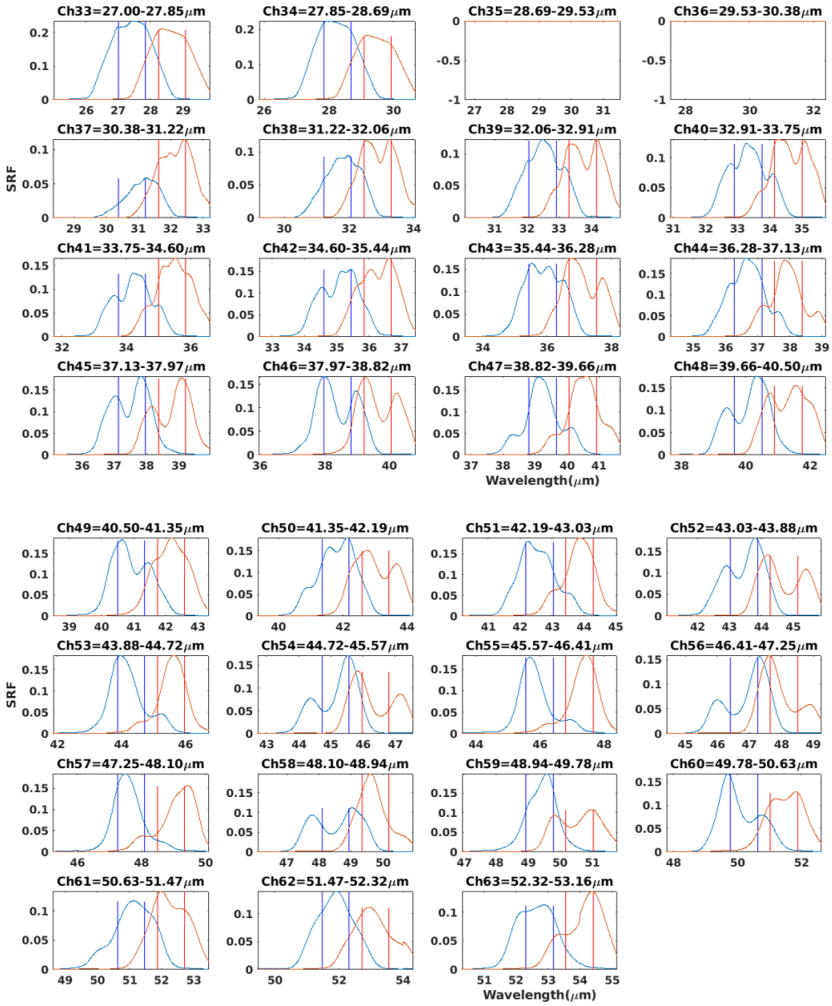

Figure 5.2: Same as Figure **??**, but for PREFIRE channels 33-63.

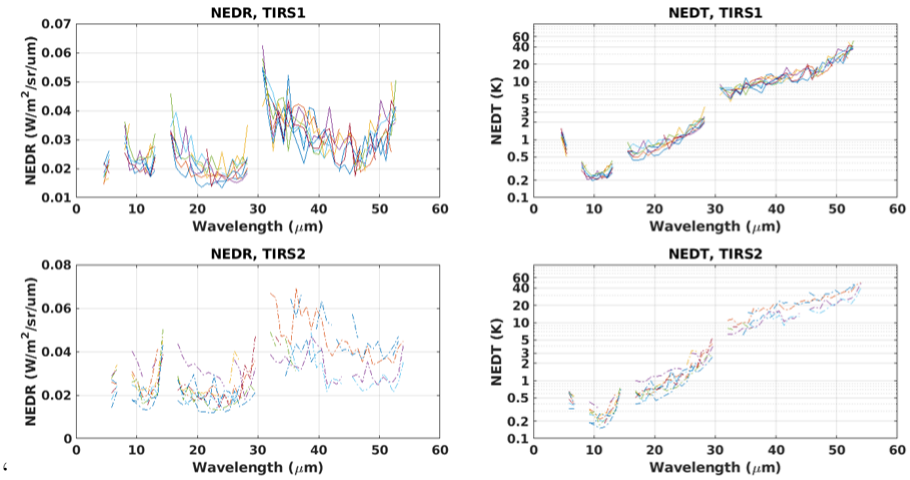

Figure 5.3: Left: Noise-Equivalent Delta Radiance (NEDR,1-sigma radiance noise level) of PREFIRE measurements. Right: same as left but for Noise-Equivalent Delta Temperature at a temperature of 255 K. Top panels are for TIRS1 and lower panels are for TIRS2. Different colors are for different sensors.

5.2.3 Forward Radiative Transfer Model

In order to construct ADMs suitable for the PREFIRE, a forward radiative transfer model is needed. We use PCRTM (principal component-based radiative transfer model) V3.4 for this purpose. PCRTM was developed by Liu et al. (2006). It utilizes the correlations between radiances over different frequencies and thus, compared to the line-by-line calculation, greatly reduces the number of monochromatic calculations without significant degradation of the accuracy. Compared with the line-by-line radiative transfer model benchmark calculations, the root-mean-square errors for the PCRTM to calculate AIRS spectrum is less than 0.4 K (Liu et al., 2006). A recent intercomparison study of fast hyperspectral radiative transfer models for cloudy scenes (Aumann et al., 2018) also confirms the robust performance of the PCRTM compared to other fast radiative transfer models. The PCRTM-based simulator by Chen, Huang, and Liu (2013) is designated to interface the PCRTM with meteorological fields from both climate models and reanalyses in a flexible way and has been used in other published studies (e.g., Bantges et al., 2016; Huang et al., 2014; Pan et al., 2017; Chen et al., 2018).

5.2.4 Synthetic PREFIRE Radiance and Flux

For clear-sky condition: The profiles of temperature, humidity and ozone, and surface skin temperature from ECMWF ERA-5 are fed into the PCRTM-based radiance simulator to calculate clear-sky spectral radiance at nadir view. Profiles of CH_4, CO, and N_2O are from standard profiles (McClatchey et al.,1972. The

CO_2 vertical profile from McClatchey et al. (1972) is scaled by the CO_2 mixing ratio of the actual month as compiled by National Oceanic and Atmospheric Administration Earth System Research Laboratory. Surface emissivity is from Huang et al. (2016). For the sea-ice region, emissivity is a weighted average of water and ice emissivity using sea-ice fraction from ERA-5.

For cloudy-sky condition: the PCRTM also needs cloud phase, cloud optical depth, cloud effective size for each level with clouds. The grid is assumed to be overcast. Clouds above 440 hPa is deemed as ice clouds, clouds below 440hPa is deemed as water clouds; the effective size of ice cloud is parameterized based on cloud temperature (Ou and Liou, 1995); effective size of water cloud is fixed as 20 micron; the cloud optical depths are calculated from the liquid (Fouquart 1987) and ice water content (Ebert and Curry 1992).

Synthetic PREFIRE radiance is done by convolving the PCRTM output at 0.5 cm^{-1} resolution with the spectral response functions of individual PREFIRE channels. Synthetic PREFIRE fluxes are computed using a 2-point (32.333^o, 69.203^o) Gaussian quadrature (Clough et al., 1992), and are just the integration of spectral flux at 0.5 cm^{-1} within each PREFIRE channel (*i.e.*, without convolution with PREFIRE SRF). Upper panel of Figure 5.4 shows the flux difference between PCRTM using 2-point Gaussian quadrature method and LBLRTM using 3-point Gaussian quadrature method. Fluxes by PCRTM are 1-3 Wm^{-2} larger than fluxes by LBLRTM. Lower two panels of Figure 5.4 show the difference in clear-sky fluxes between 2-point and 3-point Gaussian quadrature. The differences are within -0.1 - 0.6 Wm^{-2}. This suggests that the differences between PCRTM and LBLRTM are mainly from their radiation algorithms, not from Gaussian quadrature.

5.3 Algorithm

Figure 5.5 demonstrates the overall algorithm. There are three steps in the algorithm: (1) constructing ADMs, $R_v(\theta)$, for all valid PREFIRE channels, and mean synthetic spectral flux(F_n) for each scene type for all 58 channels which includes $F_{PREFIRE}$ for valid PREFIRE channels and $F_{non-PREFIRE}$ for six invalid PREFIRE channels), (2) estimating the spectral flux at each PREFIRE valid channel ($F_{PREFIRE}$), and (3) estimating the spectral fluxes at channels with zero SRF or large noise ($F_{non-PREFIRE}$).

5.3.1 Scene Type Information

(1) Definition of Scene or Sub-scene Type Over the polar region (60^o-90^oN and 60^o-90^oS): The surface types can be categorized into six kinds as listed in Table 5.2. They are defined using sea ice fraction, snow depth, and land-ocean mask. The sub-scene type (also called the discrete interval) of a footprint for clear-sky is defined based on surface skin temperature, total column water vapor (precipitable water), and lapse rate (surface skin temperature minus air temperature at 300 hPa above surface). The definition of sub-scene types for the clear sky is shown in Table 5.3. The sub-scene type for the overcast sky is defined based

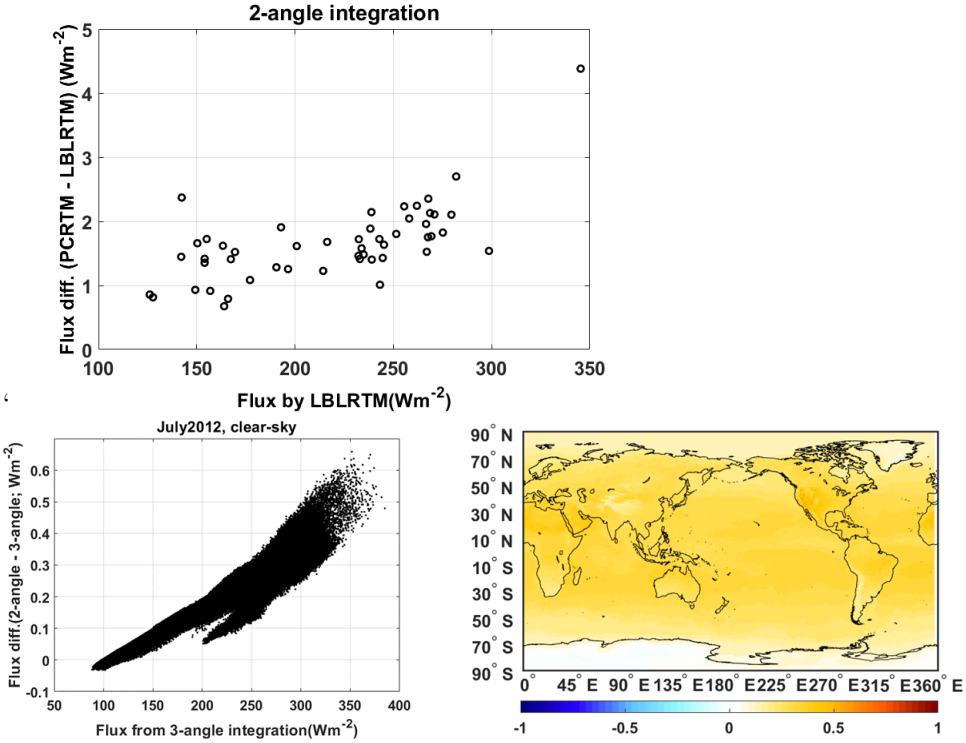

Figure 5.4: Upper: flux difference between PCRTM using 2-point Gaussian quadrature method and LBLRTM using 3-point Gaussian quadrature method. 52 profiles from ECMWF, which were used in Liu et al. (2005) for PCRTM validation, are used here for the calculation. Lower left: Scatter plot of the difference in clear-sky broadband longwave flux at TOA between 2-point (2-angle) and 3-point (3-angle) Gaussian quadrature method by PCRTM V3.4. Lower right: spatial map of the monthly-mean difference in clear-sky broadband longwave flux at TOA between 2-point and 3-point Gaussian quadrature by PCRTM V3.4. Global mean and RMSE are 0.28 and 0.26 Wm^{-2}, respectively. ECMWF ERA-5 in 2012July (only 00UTC for each day) are used for the calculation.

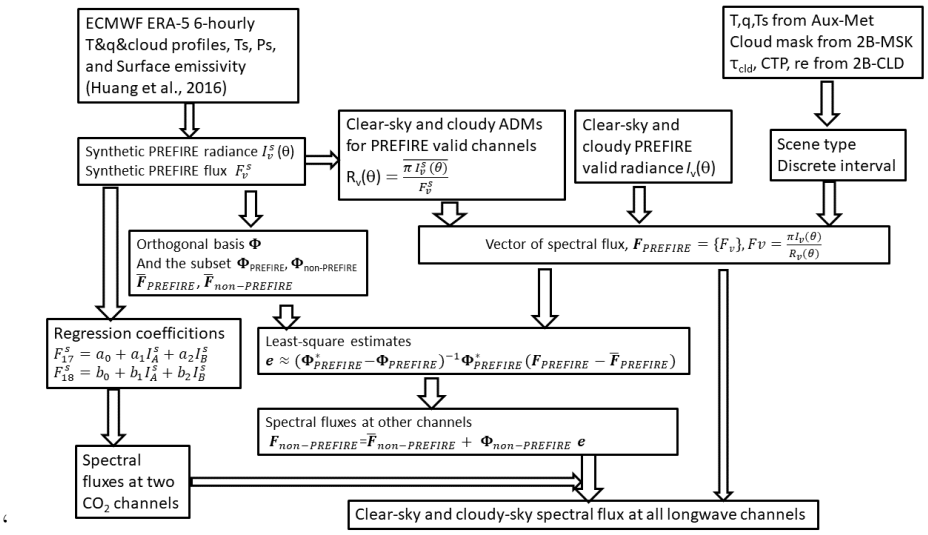

Figure 5.5: Flowchart illustration of the algorithm for deriving spectral fluxes from the PREFIRE radiances.

on surface skin temperature, precipitable water, the temperature difference between surface and cloud top, pseudoradiance (Loeb et al. [2005].), which is calculated based on cloud optical depth and cloud top temperature (pressure). The discrete intervals of precipitable water, the temperature difference between surface and cloud top, and surface skin temperature are shown in Table 5.4.
(2) Scene type information for ADM construction and PREFIRE flux derivation
For ADM construction, we need scene-type information to sort the synthetic PREFIRE radiance and flux into a discrete interval. Sea ice fraction, snow depth, surface skin temperature, total column water vapor and lapse rate are all from ECMWF ERA-5. For PREFIRE flux derivation, given a PREFIRE radiance, we need scene-type information to find a proper anisotropic factor in the ADMs. So far, we have not observed PREFIRE radiance, we derive PREFIRE fluxes from synthetic PREFIRE radiances, which are simulated using reanalysis. So, sea ice fraction, snow depth, surface skin temperature, total column water vapor, lapse rate are also from reanalysis. Later if there are observed PREFIRE radiance, sea ice fraction and snow depth can be from observation, and surface skin temperature, total column water vapor and lapse rate can be from ERA-5 reanalysis, or PREFIRE retrievals if there are such products. Cloud optical depth, cloud top pressure, and cloud effective radius are from retrievals by cloud properties algorithm.

5.3.2 Spectrally Dependent ADMs

Following Loeb et al. (2005), Huang et al. (2008; 2010; 2014), and Chen et al. (2013), an angular distribution model is needed to convert directional radiance

Surface type	description
Sea ice	sea ice fraction≥95% over the ocean & snow depth<0.001m
Melted ice	sea ice fraction between 5% and 95% over the ocean & snow depth<0.001m
Ocean	sea ice fraction<5% over the ocean & snow depth<0.001m
Permanent snow	snow depth≥0.5m over then land (mainly over the Antarctic and Greenland)
Fresh snow	0.001m≤snow depth<0.5m over the land
Non-snow land	snow depth<0.001m over the land

Table 5.2: Surface type classification over the polar region.

Precipitable water (pw; cm)	lapse rate (ΔT; K)	surface skin temperature (T_s; K)
0-0.5	<-10	<230
0.5-1	-10 - 0	230-250
1-2	0 - 10	250-270
>2	10-20	270-290
	>20	>290

Table 5.3: Definition of clear-sky scene types. Each scene type is defined with respect to different ranges of pw, ΔT, and T_s, which was referred to as a "discrete interval" in Loeb et al. (2005). ΔT is defined as the lapse rate in the first 300 hPa of the atmosphere above the surface.

Precipitable water (pw; cm)	Surface-cloud temperature difference (ΔT_{sc}; K)	surface skin temperature (T_s; K)
0-0.5	<-15	<230
0.5-1	-15 to 85 every 5K	230 to 270 every 10K
1-2	>85	270 to 290 every 5K
>2		> 290

Table 5.4: Definition of overcast scene types.

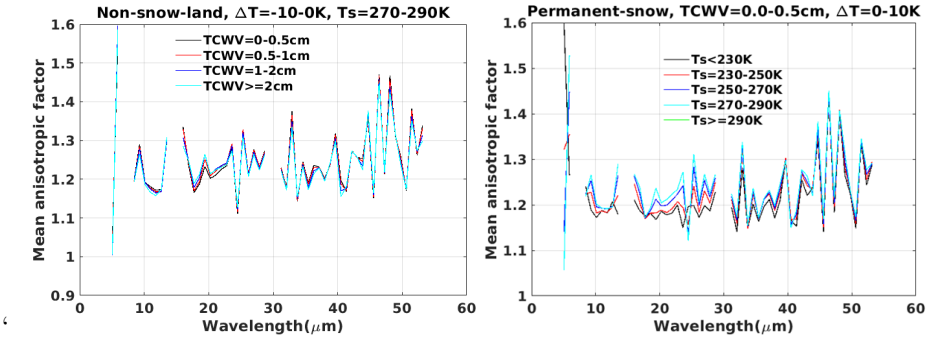

Figure 5.6: Left: Mean anisotropic factor for different precipitable water (total column water vapor; TCWV) over the non-snow land surface; Right: same as the left but for different surface skin temperature Ts over the permanent snow surface.

measurement to flux. The central quantity in such conversion is the anisotropic factor, which is defined as

$$R_n(\theta) = \frac{\overline{\pi I_n^s(\theta)}}{F_n^s} \tag{5.1}$$

where $I_n^s(\theta)$ is the synthetic upwelling radiance intensity at TOA for channel n and viewing zenith angle θ. For nadir view,F_n^s is the corresponding synthetic upwelling flux. Overbar denotes the average of all profiles within the same discrete interval as defined in Tables 5.3 and 5.4.

The spectral ADM consists of a set of pre-determined look-up tables of $R_n(\theta)$ for each sub-scene type and for each channel, so it can be used to derive the flux based on Eq. 5.2 using the PREFIRE-measured $I_n(\theta)$.

To construct the spectral ADMs, in practice we used ERA-5 reanalyses from four months (January, April, July and October) in 2005. For clear sky, we build spectral ADMs for each surface type, more than eight thousand profiles are chosen to construct the spectral ADMs. For an overcast sky, the spectral ADMs are not dependent on surface type.

(1) Anisotropic factor for different precipitable water and T_s

Figure 5.6 shows an example of the anisotropic factor for different precipitable water (or total column water vapor; TCWV) and surface skin temperature T_s. For most PREFIRE channels, $R_n(\theta = 0^o)$ are within 1.1-1.3. The $R_n(\theta = 0^o)$ has a small dependence on TCWV except for wavelengths between 16-25 microns. The $R_n(\theta = 0^o)$ has larger dependence on T_s than on TCWV.

(2) Anisotropic factor for different surface types.

Figure 5.7 shows an example of the anisotropic factor for different surface types. The dependence on surface type is obvious for window channels between 8-14 μm.

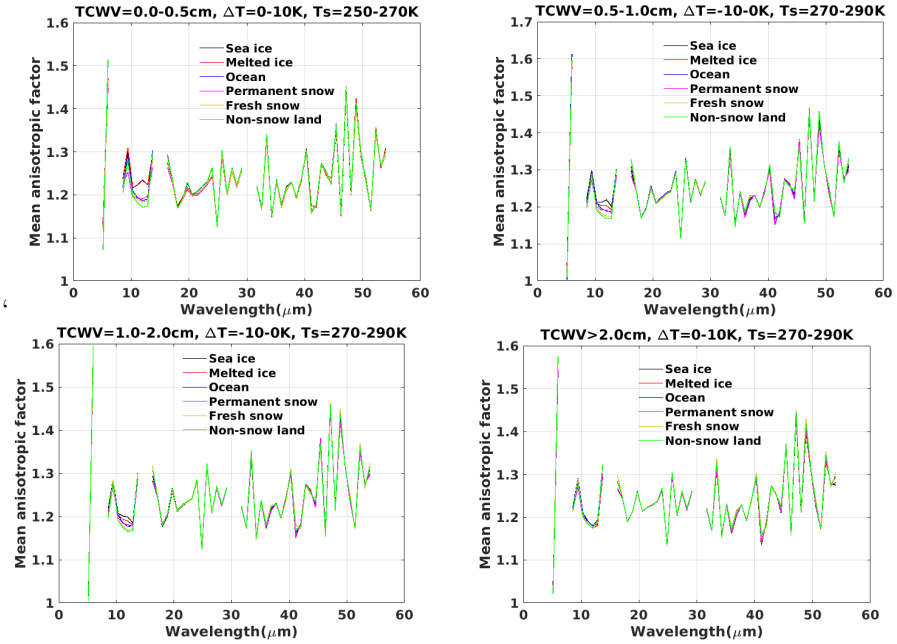

Figure 5.7: Mean anisotropic factor for different surface types. Each panel is for a sub-scene type labeled in the title.

5.3.3 Estimating Spectral LW Fluxes from Spectral Radiance

The algorithm is following Huang et al. (2008; 2010; 2014), and Chen et al. (2013). It is summarized below: For channels with valid PREFIRE radiance, the derivation of spectral flux is straightforward. It merely uses Eq 5.2. With the ADMs, $R_n(\theta)$, built in Section 5.3.2, we also need scene type information defined using TCWV, T_s and ΔT to derive spectral flux from PREFIRE spectra. They are either from atmospheric retrievals or from reanalysis. For an overcast sky, which is determined using the cloud mask product, we also need cloud optical depth, cloud top pressure, and cloud effective radius. They are from cloud property retrievals.

$$F_n = \frac{\pi I_n(\theta)}{R_n(\theta)} \tag{5.2}$$

$F_{PREFIRE}$=F_n. To obtain spectral fluxes over the entire longwave spectral range, a scheme has to be developed to estimate spectral fluxes at invalid PREFIRE channels 8,9, 17,18 35, 36 and other channels with large NEDR. A multi-regression scheme based on the Principal Component Analysis is used to obtain the corresponding spectra fluxes. Parameters in the regression scheme are derived based on the ECMWF ERA-5 profiles and synthetic spectra. For every ECMWF ERA-5 profile falling into a given discrete interval, the synthetic spectral fluxes at all channels are computed. Spectral EOF analysis (principal component analysis in the spectral domain) (Haskins et al., 1999; Huang et al., 2003; Huang and Yung, 2005) is then applied to the collection of synthetic spectral fluxes to derive a set of orthogonal basis functions in the frequency domain,

$$F_n^s = \bar{F}_n \sum_{j=1}^{58} e_j \varphi_n^j \tag{5.3}$$

where F_n^s is the synthetic spectral flux at frequency ν_n from one ECWMF profile and $\bar{F}_n$ is the average of all synthetic spectral fluxes at ν_n. The sum spans the total number of channels, $\varphi_n^j (j = 1 - 58)$ are the principal components (unitary vectors) that consist of a complete set of orthogonal basis in the N-dimensional space, and e_j is the projection of $(F_\nu^s - \bar{F}_\nu)$ onto the j^{th} principal component ϕ_ν^j. In practice, it is found that 99.99% variance can be explained by the first 13 or even fewer principal components. Therefore, we only retain the first M principal components that account for 99.99% variance. In the matrix form, it means

$$F^s - \bar{F} \approx [\varphi^1, \varphi^2, \ldots, \varphi^M] \begin{bmatrix} e^1 \\ e^2 \\ \ldots \\ e^M \end{bmatrix} = \Phi e^s \tag{5.4}$$

where F^s,

$F \cong \{\bar{F}_{PREFIRE}, \bar{F}_{non-PREFIRE}\}$, $\varphi^1, \varphi^2, \ldots, \varphi^M$ are vectors with a dimension of 58 ($M \ll 58$). Correspondingly, $\Phi = \{\Phi_{PREFIRE}, \Phi_{non-PREFIRE}\}$ is an $58 \times M$ matrix and e_s is an $M \times 1$ vector. Note that the total number of channels is 58. The total number of valid PREFIRE channels is smaller than

58 but still much larger than M. Since Eq. 5.4 holds for all channels, if we use PREFIRE in subscript to denote a set of valid PREFIRE channels, we still have

$$F_{PREFIRE} - \bar{F}_{PREFIRE} \approx \Phi_{PREFIRE} e \tag{5.5}$$

Note that $F_{PREFIRE}$ could be derived from valid PREFIRE measurement using Eq. 5.2. $\bar{F}_{PREFIRE}$, on the other hand, are the mean spectral fluxes at all PREFIRE channels from the synthetic spectra for each sub-scene type same as for ADMs. Eq. 5.5 implies a least-square solution

$$e \approx (\Phi_{PREFIRE}* - \Phi_{PREFIRE})^{-1} \Phi_{PREFIRE}* (F_{PREFIRE} - \bar{F}_{PREFIRE}) \tag{5.6}$$

where $\Phi*$ is the transpose of Φ. In practice, because of $M \ll 58$, $\Phi_{PREFIRE}$ is well-conditioned for every discrete interval and inversion of ($\Phi *_{PREFIRE}$ $\Phi_{PREFIRE}$) is numerically stable. Once e is obtained for every qualified PREFIRE observation, Eq. 5.7 can be used to derive the spectral flux at all PREFIRE channels.

$$F \approx \Phi e + \bar{F} \tag{5.7}$$

Where $F = \{F_{PREFIRE}, F_{non-PREFIRE}\}$.

The left panel in Figure 5.8 shows an example of the performance of the algorithm. The derived spectral flux agrees well with true spectral flux except for two channels in the CO_2 band. This is largely because of that the CO_2 channels have a smaller correlation with other channels. To improve the derived flux at CO_2 channels (n= 17, 18), we replace the results with fitted flux using two-channel (n = 19, 20 for TIRS1 and n = 16, 19 for TIRS2) PREFIRE radiances as,

$$F_{17}^s = a_0 + a_1 I_A^s + a_2 I_B^s \tag{5.8}$$

$$F_{18}^s = b_0 + b_1 I_A^s + b_2 I_B^s \tag{5.9}$$

Where A and B are two valid channels, a_0, a_1, a_2 and b_0, b_1, b_2 are regression coefficients.

Figure 5.9 shows an example of the predicted spectral fluxes at two CO_2 channels compared with true fluxes over the sea ice surface. Similar results can be found for other surface types (not shown). Overall, the slope is higher than 0.98 and R^2 is larger than 0.94 for all surface types and for both with noise (data from the left panel of Figure 5.3) excluded and included.

5.4 Validations

5.4.1 Theoretical Validation

For theoretical validation, synthetic PREFIRE radiances are used to derive the spectral fluxes and such spectral fluxes are compared with those directly computed true flux by the PCRTM V3.4. True PREFIRE flux and synthetic PREFIRE radiance are computed using GEOS-5 FP-IT temperature, humidity, and

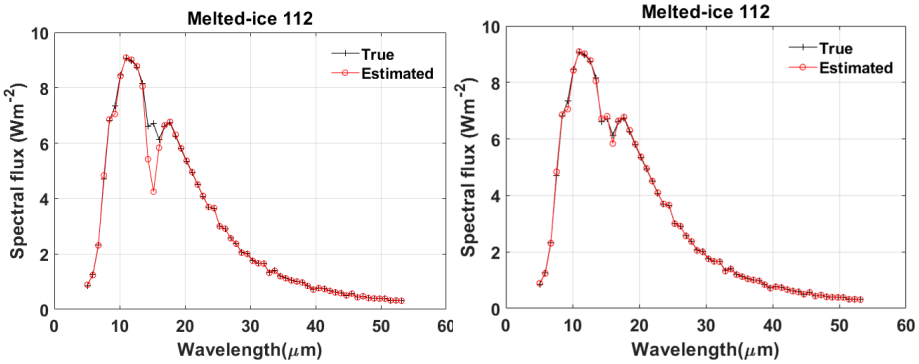

Figure 5.8: Left: Comparison of derived spectral flux with true spectral flux over the sea ice surface and for sub-scene type: 0<TCWV<0.5cm, ΔT <-10K and 230K< T_s <250K. Right: same as left, but estimated flux in two CO_2 channels are replaced with flux fitted using two-channel radiances

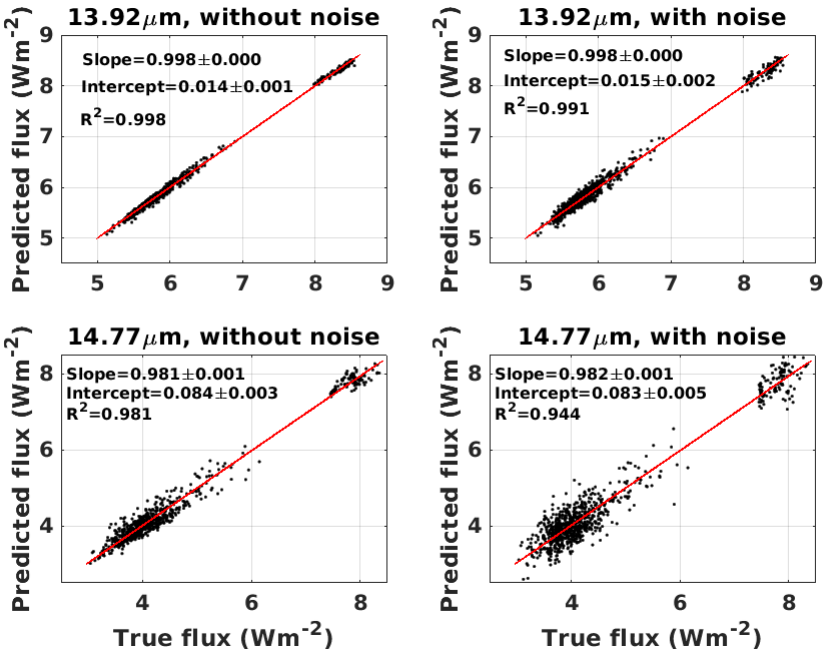

Figure 5.9: Comparison of derived spectral flux with true spectral flux over the sea ice surface for two CO_2 PREFIRE channels. Each dot denotes a sub-scene type in 2005. Synthetic PREFIRE radiances and true fluxes are simulated using ERA-5 profiles. Left column: predicted fluxes are computed using Eqs 5.8 and 5.9 where the noise of PREFIRE measurement is not included in I_{19} and I_{20}. Right column: Same as the left column but the noise of PREFIRE measurement (data from the left panel of Figure 5.3) is included in I_{19} and I_{20}.

Sensor	TIRS 1 Sim Performance			TIRS 1 Error Delta	TIRS 2 Sim Performance			TIRS 2 Error Delta
	5^{th}	95^{th}	median		5^{th}	95^{th}	median	
1	-6.3	4.7	-0.1	13.4	-38.5	4.0	-0.2	22.6
2	-6.9	4.7	0.1	13.6	-37.8	4.2	-0.1	22.6
3	-8.3	4.9	0.1	14.1	-28.9	4.5	-0.3	22.6
4	-6.2	5.0	0.2	13.4	-38.2	4.3	0.0	22.6
5	-6.6	5.1	0.1	13.5	-24.8	4.0	-0.2	22.4
6	-6.4	5.0	0.2	13.4	-41.6	4.3	-0.0	22.7
7	-6.5	5.0	0.1	13.5	-26.4	4.5	-0.2	22.5
8	-7.5	5.3	-0.0	14.0	-25.8	3.9	-0.3	22.4
Aggregate	-6.7	5.0	0.1	13.6	-33.1	4.2	-0.2	22.6

Table 5.5: 5^{th}, 95^{th} percentile, median value, and error Delta (root mean square error) of the relative difference (%) between predicted and true spectral flux for TIRS1 and TIRS2. Aggregate value is from the combination of all 8 Sensors.

cloud profiles in four months of 2021 (3 days in each month). Synthetic PREFIRE radiances, T and q from Aux-met (determining scene type intervals for clear sky), as well as the cloud mask product (determining clear sky or overcast sky), cloud properties product (determining scene type intervals for overcast sky) retrieved from the PREFIRE radiances, are applied to the algorithm to get predicted PREFIRE flux. The differences between the spectral fluxes (or the broadband OLR) predicted from the synthetic PREFIRE radiance and the ones directly computed by the PCRTM are examined. This validation lets us assess the whole algorithm without concerning the accuracy in spectroscopy and forward modeling since the PCRTM is used as a surrogate of radiative transfer in the real world.

Figures 5.10 and 5.11 are the comparison (relative difference) between derived spectral fluxes and true (synthetic) fluxes (including both clear sky and overcast sky) for each sensor type of TIRS1 and TIRS2. The largest errors are still from the two CO_2 channels or channels not covered with valid PREFIRE radiance, and these two channels have less correlation with other valid channels.

Figures 5.12 and 5.13 are the histogram of the difference between predicted OLRs and true (synthetic) OLRs (including both clear sky and overcast sky) for each sensor type of TIRS1 and TIRS2. OLR is the integration of spectral flux over the whole longwave. Overall, the OLR differences are within ± 5 Wm^2.

Table 5.5 summarizes the relative difference between predicted and true spectral flux at all 58 PREFIRE channels. Table 5.6 summarizes the relative difference between predicted and true OLRs. The median errors are very close to 0% for both TIRS1 and TIRS2. The RMSE errors of TIRS2 are generally larger than those of TIRS1, which is primarily due to the spectral shifts of two missing CO_2 channels of TIRS2 compared to TIRS1.

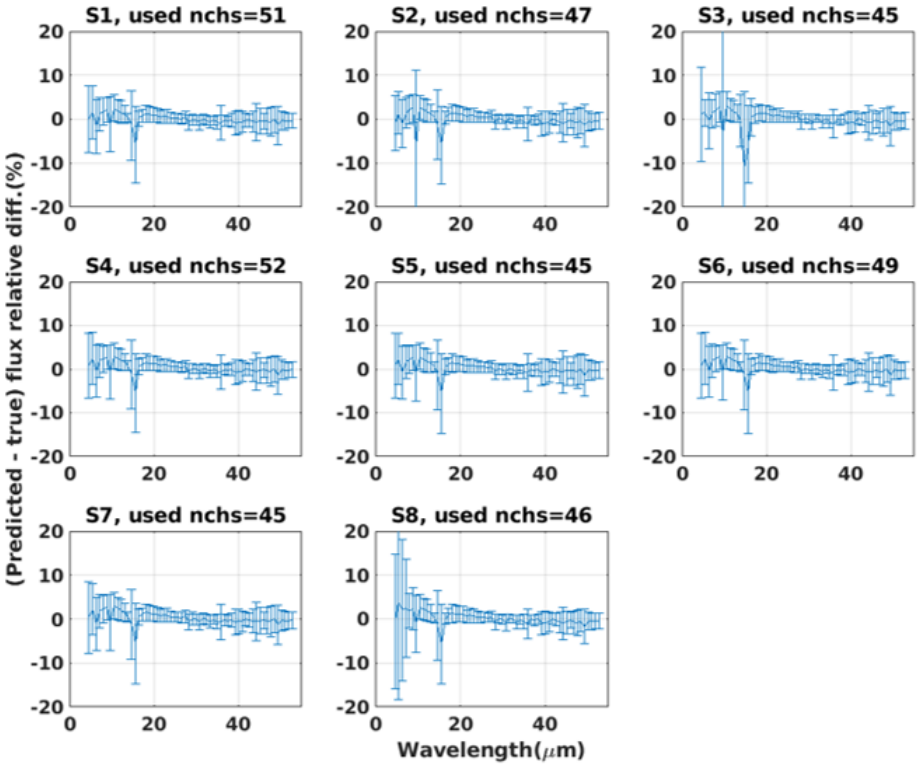

Figure 5.10: Relative difference between predicted and true spectral flux for all PREFIRE longwave channels, and for each sensor type of instrument TIRS1. The sensor number and number of channels used for deriving the whole longwave flux are labeled on the title. All cases are from the polar regions.

Sensor	TIRS 1 Sim Performance			TIRS 1 Error Delta	TIRS 2 Sim Performance			TIRS 2 Error Delta
	5^{th}	95^{th}	median		5^{th}	95^{th}	median	
1	-1.6	2.3	0.2	1.3	-3.5	2.7	-0.5	2.1
2	-1.6	2.5	0.2	1.3	-3.3	3.2	-0.2	2.0
3	-2.2	2.9	-0.2	1.6	-2.7	2.2	-0.7	1.6
4	-1.2	3.1	0.5	1.4	-3.1	3.2	-0.1	2.0
5	-1.6	3.1	0.4	1.5	-2.6	2.2	-0.4	1.5
6	-1.2	3.0	0.5	1.5	-3.4	3.1	-0.1	2.1
7	-1.2	3.0	0.5	1.4	-2.7	2.2	-0.4	1.6
8	-1.7	3.0	0.4	1.6	-2.7	1.9	-0.5	1.5
Aggregate	-1.6	2.9	0.3	1.5	-3.0	2.6	-0.4	1.8

Table 5.6: Same as Table 5.5, but for the relative difference (%) of predicted and true OLR for TIRS1 and TIRS2.

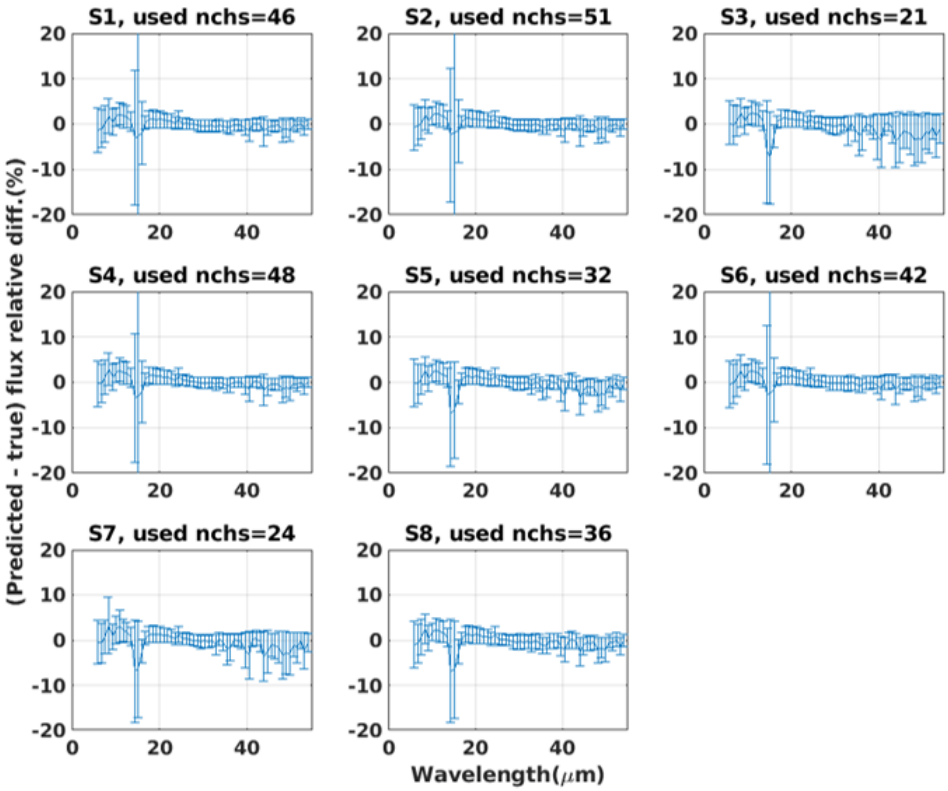

Figure 5.11: Same as Figure 5.10 but for 8 sensors of instrument TIRS2.

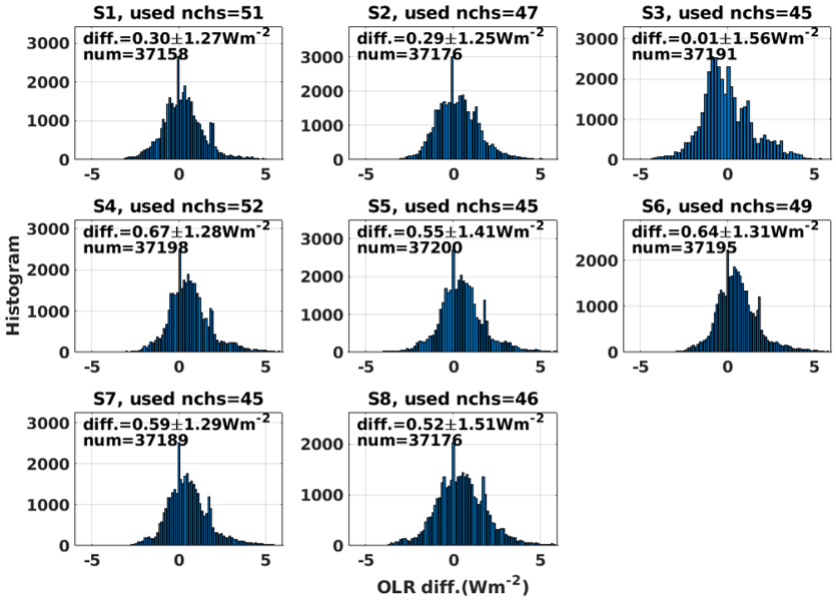

Figure 5.12: Histogram of OLR difference between prediction and truth for 8 sensors of instrument TIRS1. The mean, standard deviation, and number of cases are shown on each panel. All cases are from the polar regions.

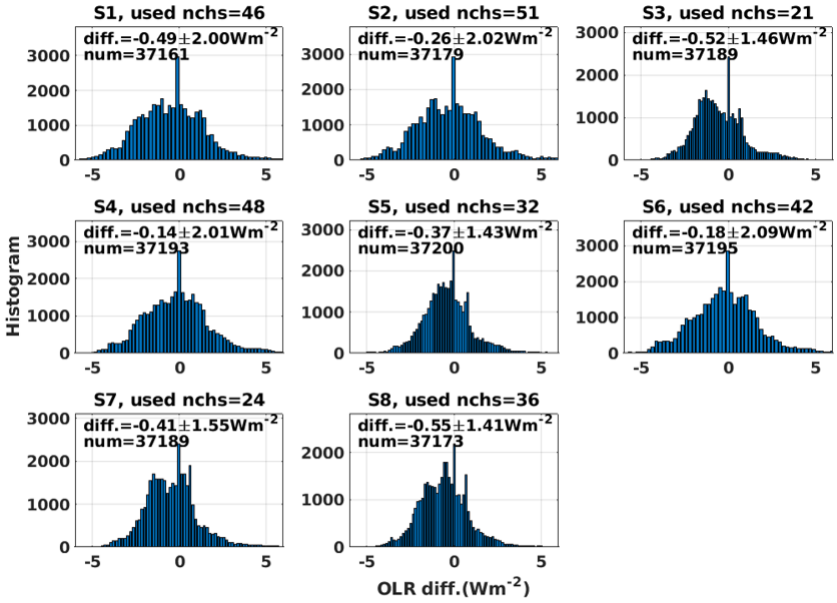

Figure 5.13: Same as Figure 5.12 but 8 sensors of instrument TIRS2.

5.4.2 Validation using Observation

So far, there are no PREFIRE observations that can be used for this validation.

5.5 References

Aumann, H. H., et al., 2018: Evaluation of radiative transfer models with clouds. Journal of Geophysical Research: Atmospheres, 123, 6142–6157. https://doi.org/10.1029/2017JD28073.

Bantges, R., H. Brindley, X. H. Chen, X. L. Huang, J. Harries, & J. Murray, 2016: On the detection of robust multi-decadal changes in the Earth's outgoing longwave radiation spectrum. J. Climate, 29(13), 4939–4947. https://doi.org/10.1175/JCLI-D-15-0713.1.

Chen, X. H., X. L. Huang, and X. Liu, 2013: Non-negligible effects of cloud vertical overlapping assumptions on longwave spectral fingerprinting studies. Journal of Geophysical Research: Atmospheres, 118, 7309-7320. https://doi.org/10.1002/jgrd.50562.

Chen, X. H., X. L. Huang, N. G. Loeb, H. L. Wei, 2013: Comparisons of clear-sky outgoing far-IR flux inferred from satellite observations and computed from three most recent reanalysis products. J. Climate, 26(2), 478-494, doi:10.1175/JCLI-D-12-00212.1.

Chen, X. H., X. L. Huang, X. Q. Dong, B. K. Xi, E. Dolinar, N. Loeb, S. Kato, P, Stackhouse, M. Bosilovich, 2018: Using AIRS and ARM SGP clear-sky observations to evaluate meteorological reanalyses: a hyperspectral radiance closure approach. JGR-Atmospheres, 123 (20), 11720-11734, 10.1029/2018JD028850.

Clough et al., 1992: Line-by-Line Calculations of Atmospheric Fluxes and Cooling Rates' Application to Water Vapor. Journal of Geophysical Research: Atmospheres,15,761-15,785, 1992.

Dee, D. P., et al., 2011: The ERA-Interim reanalysis: Configuration and performance of the data assimilation system. Quarterly Journal of the Royal Meteorological Society, 137(656), 553–597. https://doi.org/10.1002/qj.828. Haskins, R., et al., 1999: Radiance covariance and climate models. J. Climate, 12, 1409–1422.

Ebert, E. E., and Curry, J. A. 1992: A parametrization of ice cloud optical properties for climate models, Journal of Geophysical Research: Atmospheres, 97, 3831–3836.

Fouquart, Y. 1987: Radiative transfer in climate models, in Physically Based Modelling and Simulation of Climate and Climate Changes, edited by M. E.

Schlesinger, pp. 223–284, Kluwer Acad., Norwell, Mass.

Hersbach, H. et al., 2020: The ERA5 global reanalysis. Quarterly Journal of the Royal Meteorological Society, 146,
https://doi.org/10.1002/qj.3803.

Huang, X. L., and Y. L. Yung, 2005: Spatial and spectral variability of the outgoing thermal IR spectra from AIRS: A case study of July 2003. J. Geophys. Res., 110, D12102, doi:10.1029/2004JD005530.

Huang, X. L., J. J. Liu, and Y. L. Yung, 2003: Analysis of thermal emission spectrometer data using spectral EOF and tri-spectral methods. Icarus, 165, 301–314, doi:10.1016/S0019-1035(03)00206-9.

Huang, X. L., N. G. Loeb, and W. Z. Yang, 2010: Spectrally resolved fluxes derived from collocated AIRS and CERES measurements and their application in model evaluation: 2. cloudy sky and band-by-band cloud radiative forcing over the tropical oceans. J. Geophys. Res. Atmos, 115, D21101, doi:10.1029/2010JD013932.

Huang, X. L., W. Z. Yang, N. G. Loeb, and V. Ramaswamy, 2008: Spectrally resolved fluxes derived from collocated AIRS and CERES measurements and their application in model evaluation: 1. clear sky over the tropical oceans. J. Geophys. Res. Atmos, 113, D09110, doi: 10.1029/2007JD009219.

Huang, X. L., X.H. Chen, D. K. Zhou, X. Liu, 2016:An observationally based global band-by-band surface emissivity dataset for climate and weather simulations. Journal of the Atmospheric Sciences, 73, 3541-3555, doi:10.1175/JAS-D-15-0355.1.

Huang, X. L., X. H. Chen, G. L. Potter, L. Oreopoulos, J. N.S. Cole, D.M. Lee, N. G. Loeb, 2014: A global climatology of outgoing longwave spectral cloud radiative effect and associated effective cloud properties. J. Climate, 27, 7475-7492, doi:10.1175/JCLI-D-13-00663.1.

Huang, X. L., X. H. Chen, B. J. Soden, & X. Liu, 2014: The spectral dimension of longwave feedbacks in the CMIP3 and CMIP5 experiments. Geophysical Research Letters, 41, 7830–7837.
https://doi.org/10.1002/2014GL061938.

Liu, X., W. L. Smith, D. K. Zhou, & A., Larar, 2006: Principal component-based radiative transfer model for hyperspectral sensors: Theoretical concept. Applied Optics, 45(1), 201–209.
https://doi.org/10.1364/AO.45.000201.

Loeb, N. G., S. Kato, K. Loukachine, and N. Manalo-Smith, 2005: Angu-

lar distribution models for top-of-atmosphere radiative flux estimation from the Clouds and the Earth's Radiant Energy System instrument on the Terra satellite. Part I: Methodology. J. Atmos. Oceanic Technol., 22, 338–351, doi:10.1175/JTECH1712.1.

Loveland, T. R., and Coauthors, 2000: Development of a global land cover characteristics database and IGBP DISCover from 1 km AVHRR data. Int. J. Remote Sensing, 21, 1303–1330.

McClatchey, R., R. Fenn, J. Selby, F. Volz, and J. Garing, 1972: Optical properties of the atmosphere, Tech. Rep. AFCRL-72-0497, AFGL (OPI), Hanscom AFB, MA 01731.

Ou, S.-C., and K.-N. Liou 1995: Ice microphysics and climatic temperature feedback. Atmos. Res., 35, 127–138.

Pan, F., X. L. Huang, S. S. Leroy, P. Lin, L. L. Strow, Y. Ming, & V. Ramaswamy, (2017). The stratospheric changes inferred from 10 years of AIRS and AMSU-A radiances. J. Climate, 30(15), 6005–6016.
https://doi.org/10.1175/JCLI-D-17-0037.1.

6 Appendix

6.1 Table of variables

$\mathbf{A}$	Averaging Kernel Matrix	NEDT	Noise-Equivalent Difference Temperature
α	angular resolution	o	offset
β	azimuth angle	Ω	Solid angle
B	blackbody radiance	p	pressure
χ	convergene criterion	P	Probability
c	speed of light,	PWV	Precipitable Water Vapor
	cost function	Q	water vapor
CWP	Cloud Water path	ρ	reflection coefficient
d	degree of freedom	R	radius, Resistance, cost-function change
ε	emissivity	$\Re$	Response function
ϵ	noise, error	$\wp$	Responsivity
ϕ	longitude	σ_B	Stefan-Boltzmann constant
E	Irradiance	$\mathbb{S}$	Signal level in digitized counts
F	Flux	S	covariance
f	focal length	SI	segmentation index
$\mathcal{F}$	function	SNR	Signal-to-Noise ratio
γ	*a priori* weight	SRF	Spectral Response Function
	Airy function	θ	latitude, potential temperature
			polar coordinate angle
G	gravitational constant	τ	transmission, optical depth
g	gain	T	Temperature
H	height	$\mathbf{TR}$	Training Radiances
h	Planck's constant	$\mathbf{TREM}$	Training Eigenvector matrices
I	radiance	t	time
IWC	Ice water content	ϕ	polar coordinate angle
IWP	Ice water path	V	voltage
j	counter	v	velocity
k	Boltzmann's constant, unknown in eq 3.11	x, y, z	position coordinates
$\mathbf{K}$	Jacobian	z	convergence (eq. 3.11)
λ	wavelength, Marquardt-Levenberg parameter		standard deviation of scaled differences
l	distance	$\mathbf{x}$	state vector
L	radiance	X	Focal plane position
LTS	Lower tropospheric stability	$\mathbf{y}$	measurement vector
LWC	Liquid water content	$\mathbf{Y}$	eq. 4.9 not clear
LWP	Liquid water path	Y	Focal plane position
M	counter, mass	ζ	incidence angle
$\mathcal{M}$	matrix		
N	counter		
n	channel		
$\mathcal{N}$	Normal distribution		
ν	frequency		

6.2 Abbreviations and Acronyms

ADM	Angular Distribution Model
AIRS	Atmospheric Infrared Sounder
ATBD	Algorithm Theoretical Basis Document
CERES	Clouds and the Earth's Radiant Energy System
DOF	Degree of Freedom
ECMWF	European Centre for Medium-Range Weather Forecasts
EOF	Empirical Orthogonal Function
FIR	Far-InfraRed
IFS	Integrated Forecasting System
LW	Longwave
MIR	Mid-InfraRed
OLR	Outgoing Longwave Radiation
PCRTM	Principal Component-based Radiative Transfer Model
PREFIRE	Polar Radiant Energy in the Far-InfraRed Experiment
RMSE	Root Mean Square Error
SSF	Single Scanner Footprint
SRF	Spectral Response Function
TCWV	Total Column Water Vapor
TOA	Top of Atmosphere
UTC	Coordinated Universal Time
VZA	Viewing Zenith Angle
WV	Wavelength

Table 6.1: Abbreviations and Acronyms in this chapter.

6.3 Figure listing with links.

#	Brief Description	#	Brief Description
1.1	L1 Flowchart	5.1	SRFs for channels 1-32
1.2	Measured NEDR	5.2	SRFs for channels 33-63
2.1	GMAO simulations of column OD	5.3	TIRS1 and TIRS2 NEDR and NEDT
2.2	GMAO simulations of PWV	5.4	Flux differences for different methods
2.3	Cloud algorithm training	5.5	Spectral flux algorithm flowchart
2.4	Cloud algorithm EOFs	5.6	Mean anisotropic factor by PWV
2.5	Similarity indexes histogram	5.7	Mean anisotropic factor by surface type
2.6	Similarity indexes maps	5.8	Flux comparisons to truth as spectra
2.7	Cross-entropy loss	5.9	FLux comparisons to truth as statistics
2.8	Cloud mask 2D histrogram	5.10	Flux difference by channel for TIRS1
3.1	TIRS SRFs grouped by filter	5.11	Flux difference by channel for TIRS2
3.2	Atmospheric pressure weighting functions	5.12	OLR difference by scene for TIRS1
3.3	Atmospheric algorithm flowchart	5.13	OLR difference by scene for TIRS2
3.4	*A priori* T correlation and variance		
3.5	Reanalysis regions		
3.6	DFS joint histograms		
3.7	Temperature retrieval metrics		
3.8	Water vapor retrieval metrics		
3.9	Antarctic ground stations		
3.10	Arctic ground stations		
4.1	SSE algorithm flowchart		
4.2	SSE averaging kernels		
4.3	SSE error estimates, noise-free		
4.4	SSE error estimates with sensor noise		
4.5	SSE truth different for TIRS1		
4.6	SSE truth different for TIRS2		

Table 6.2: List of Figures in this set of ATBDs.